

THESIS ON CIVIL ENGINEERING F70

**Application of Terrestrial Laser
Scanning Technology for Engineering
Structure Surveys**

TARVO MILL



TALLINN UNIVERSITY OF TECHNOLOGY

School of Engineering

Department of Civil Engineering and Architecture

Road Engineering and Geodesy Research Group

The thesis was accepted for the defence of the degree of Doctor of Philosophy in Engineering on 2 November 2017.

Supervisor: Professor Dr. Artu Ellmann

Road Engineering and Geodesy Research Group, Department of Civil Engineering and Architecture, School of Engineering, Tallinn University of Technology, Estonia.

Opponents: Professor Dr. Thomas A. Wunderlich

Chair of Geodesy, Department of Civil, Geo and Environmental Engineering, Technical University of Munich, Germany.

Associate Professor Dr. Jānis Kaminskis

Department of Geomatics, Faculty of Civil Engineering, Riga Technical University, Latvia.

Defence of the thesis: 11 December 2017 at 14.00 p.m. in room NRG-226 in Tallinn University of Technology.

Declaration:

Hereby I declare that this doctoral thesis, my original investigation and achievement, submitted for the doctoral degree at Tallinn University of Technology has not earlier been submitted for any academic degree.

Deklaratsioon: deklareerin, et see doktoritöö, mis on minu ja minu iseseisva töö tulemus, on esitatud Tallinna Tehnikaülikooli doktorikraadi taotlemiseks ja selle alusel ei ole varem taotletud doktori- või sellega võrdsustatud teaduskraadi.

Tarvo Mill



European Union
European Social Fund



Investing in your future

Copyright: Tarvo Mill, 2017

ISSN 1406-4766

ISBN 978-9949-83-167-8 (publication)

ISBN 978-9949-83-168-5 (PDF)

EHITUS F70

Terrestriline laserskaneerimine ehituskonstruktsioonide mõõdistamisel

TARVO MILL

CONTENTS

LIST OF PUBLICATIONS.....	7
AUTHOR’S CONTRIBUTION TO THE PUBLICATIONS	9
ACRONYMS	10
1. INTRODUCTION.....	11
1.1.Terrestrial laser scanning technology.....	11
1.2.Limitations related to TLS	14
1.3.Objectives of the study.....	16
1.4.Outline of the thesis	17
2. TLS MEASUREMENTS AND UNCERTAINTY	19
2.1.Relevant statistical estimates of measurements and uncertainty.....	19
2.2.TLS related uncertainties	21
2.2.1. Factors affecting TLS accuracy	21
2.2.2. Uncertainties due to scanning geometry	22
3. THE RESULTING METHOD FOR UNCERTAINTY ESTIMATION	24
3.1.Development of the ANU calculation method.....	24
4. APPROBATION OF THE DEVELOPED METHOD	30
4.1.Set-up of the experiment	30
4.2.Geometrical proof of ANU	31
4.3.Verification of numerical results.....	34
5. MODELLING OF ANU DISTRIBUTION FOR ENGINEERING STRUCTURES	36
5.1.Set-up of the experiment	36
5.2.Numerical results	37
5.3.Results of geometric modelling of the noise-contaminated data	39
5.4.Optimization of scanning locations.....	40
6. TESTED TLS APPLICATIONS	41
6.1.TLS for monitoring deformations of engineering structures	41
6.1.1. Results of deformation monitoring	44
6.2.TLS for road surveying purposes.....	47
6.2.1. Comparison of TLS and conventional surveying techniques in road surveys	48

6.2.2. Results of the comparisons and the optimal scanning distance for road surveys	48
6.3. TLS for building surveying purposes.....	50
6.3.1. TLS for BIM purposes.....	51
6.3.2. Results of building surveying	51
7. DISCUSSION	54
7.1. Suggestions for future research.....	54
8. CONCLUSIONS.....	56
8.1. Contribution to estimating TLS along-normal uncertainties.....	56
8.2. Engineering structure surveys using the TLS technology.....	57
LIST OF REFERENCES	59
ACKNOWLEDGEMENTS	66
ABSTRACT	67
KOKKUVÕTE.....	68
PUBLICATIONS	69
CURRICULUM VITAE	135
ELULOOKIRJELDUS.....	138

LIST OF PUBLICATIONS

The listed publications are related to the topic of this thesis. The publications are peer reviewed papers published and presented here to fulfil the requirements for the PhD degree of Tallinn University of Technology.

Publications constituting the thesis (all papers are indexed by the Scopus database):

- I.** Mill, T. and Ellmann, A. (2017, online). Assessment of along-normal uncertainties for application to terrestrial laser scanning surveys of engineering structures. *Survey Review*. DOI: 10.1080/00396265.2017.1361565
- II.** Mill, T., Ellmann, A., Kiisa, M., Idnurm, J., Idnurm, S., Horemuz, M. and Aavik, A. (2015). Geodetic monitoring of bridge deformations occurring during static load testing. *The Baltic Journal of Road and Bridge Engineering*, 10(1), 17–27.
- III.** Mill, T., Ellmann, A., Aavik, A., Horemuz, M. and Sillamäe, S. (2014). Determining ranges and spatial distribution of road frost heave by terrestrial laser scanning. *The Baltic Journal of Road and Bridge Engineering*, 9(3), 227–236.
- IV.** Mill, T., Alt, A. and Liias, R. (2013). Combined 3D building surveying techniques - terrestrial laser scanning (TLS) and total station surveying for BIM data management purposes. *Journal of Civil Engineering and Management*, 19, S23–S32.
- V.** Mill, T., Ellmann, A., Uueküla, K. and Joala, V. (2011). Road surface surveying using terrestrial laser scanner and total station technologies. *Proceedings of the 8th International Conference Environmental Engineering* (pp 1142–1147). Vilnius, Lithuania: Vilnius Gediminas Technical University Press.

Relevant oral presentations in international conferences:

- A.** Mill, T. and Ellmann, A. (2016) Simulation of terrestrial laser scanning errors occurring during deformation monitoring. *The 3rd Joint International Symposium on Deformation Monitoring (JISDM)*. Vienna, Austria.
- B.** Mill, T. and Ellmann, A. (2014) Terrestrial laser scanning technology for deformation monitoring of a large suspension roof structure. *The 6th*

International Conference on Engineering Surveying. Prague, Czech Republic.

- C. Mill, T., Ellmann, A., Uueküla, K. and Joala, V. (2011) Road surface surveying using terrestrial laser scanner and total station technologies. *The 8th International Conference Environmental Engineering*. Vilnius, Lithuania.

Additional relevant publications associated with the subject of the thesis are listed in the Curriculum Vitae.

AUTHOR'S CONTRIBUTION TO THE PUBLICATIONS

The contributions to the publications are listed below:

- **Paper I.** The idea for estimating along-normal uncertainties of surfaces was proposed by the supervisor Prof. Artu Ellmann. The development of the methodology that is specially adapted for engineering structures was elaborated by the author in co-operation with the supervisor. The numerical verifications and investigating the behaviour of along-normal uncertainties for various surveying scenarios were carried out by the author, guided by the supervisor. The publication was written and improved in cooperation with the supervisor Prof. Artu Ellmann.
- **Paper II.** The field procedures for deformation monitoring using terrestrial laser scanning were developed by the author. The deformation monitoring field experiment, data processing and assessment of the results were carried out by the author. Data analysis was done by the author in co-operation with all co-authors. The preliminary calculations of the bridge structure behaviour with testing loads were performed by Prof. Juhan Idnurm. The publication was written by the author in co-operation with all co-authors.
- **Paper III.** The design of the research plan was compiled, and the field experiment, data processing and assessment of the results were carried out by the author and looked over by the supervisor Prof. Artu Ellmann. Data analysis was done by the author in co-operation with all co-authors. The publication was written by the author and improved in cooperation with all co-authors.
- **Paper IV.** The research plan was designed by the author. The data collecting was carried out by the author. The data processing and analysis were carried out in cooperation with Assoc. Prof. Aivars Alt. The publication was written by the author and improved in cooperation with all co-authors.
- **Paper V.** The research plan was designed in co-operation with the supervisor Prof. Artu Ellmann. The field experiment was carried out by the author. The data processing and assessment of the results were carried out by the author in cooperation with Katrin Ueküla and looked over by Dr. Vahur Joala. The publication was written by the author and improved in cooperation with the supervisor Prof. Artu Ellmann.

ACRONYMS

ACI	American Concrete Institute
AEC	Architecture, engineering and construction
ANU	Along-normal uncertainty
BIM	Building information modelling
COBIM	Common building information modelling
CSU	Combined standard uncertainty
DIN	German Institute for Standardization
FM	Facility management
GSA	General Services Administration, USA (gsa.gov)
HUE	Gradation of colours
<i>I</i>	Intensity
ISO	International Organization for Standardization
JCGM	Joint Committee for Guides in Metrology
kHz	Kilohertz (10^3 Hz)
MHz	Megahertz (10^6 Hz)
PS	Phase-shift
<i>RGB</i>	Colour model of three colours: red, green, and blue
TLS	Terrestrial laser scanning
TOF	Time-of-flight
WFD	Waveform digitizing
3D	Three-dimensional

1. INTRODUCTION

1.1. Terrestrial laser scanning technology

Terrestrial laser scanning (TLS) is an innovative geodetic surveying technique that allows remote capturing of high resolution and accurate spatial data. The number and variety of applications of the TLS technology in the architectural, engineering, construction and facility management (AEC/FM) industry are continuously increasing. In addition to the wide range of its applications in the AEC/FM industry, the TLS technology has been adopted by many other fields as well. For example, the technology has been widely used for forensic applications and surveying accident and disaster scenes. The collected TLS data are very versatile making it possible to document and reconstruct the surrounding three-dimensional (3D) environment with a high level of accuracy.

The benefit of the TLS survey compared to the traditional geodetic surveying techniques (e.g. geometric levelling and total station surveying) is its ability to record the surrounding environment by measuring a countless number (millions) of survey points within a matter of seconds. The surveying process is contactless, therefore there is no danger of damaging the object or the scene (e.g. accident documentation). Contactless surveying also reduces health risks to the surveyor (e.g. while surveying hazardous objects). TLS provides an automated data capture of everything within the instrument's field of view and maximum surveying range. The panoramic field of view can be up to 360° (full circle) in the horizontal and 310° in the vertical direction, thus leaving only a small area under the scanner unsurveyed. Since the TLS survey uses laser technology, bright light conditions are not required unlike for surveys with optical instruments. This, for example, is very beneficial for underground mining surveys or surveys that are only feasible at night-time (e.g. surveying of large traffic intersections).

Each TLS survey point in the resulting point cloud can be generally characterized by the coordinate components, i.e. the 3D position of the point (the rectangular x , y and z coordinates) and the intensity (I) value. The intensity value is proportional to the power of the backscattered laser beam represented generally in greyscale or in graduation of colours (i.e. HUE, Pesci and Teza 2008, Kaasalainen *et al.* 2009, cf. Fig. 1). The intensity values can be used for example to detect surface damages (Armesto-González *et al.* 2010) or distinguish different surface materials (González-Jorge *et al.* 2012). In addition to the coordinate components and the intensity, many scanners are capable of recording also *RGB* images with true colours. From these images, *RGB* values for each survey point are derived resulting in a data packet where each (i -th) data-point is characterized by x_i , y_i , z_i , I_i and RGB_i . The photorealistic TLS point cloud images (Fig. 1) are beneficial for visualization purposes and for example conservation and management of historic heritage sites (Wilson *et al.* 2013).

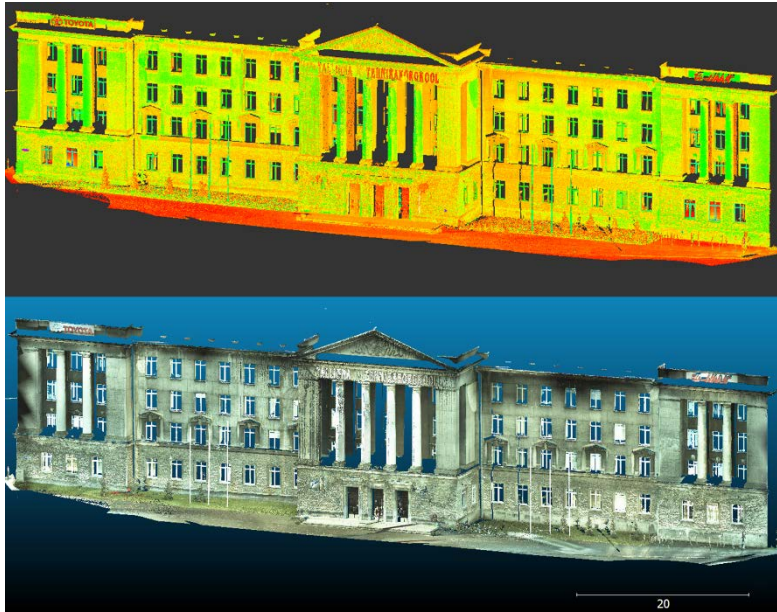


Figure 1. Rendered point clouds with intensity values represented in HUE colours (upper figure) and with true colours (lower figure) of the studied building (cf. **Paper IV**). The scale bar units are in metres.

In general, TLS survey results are referred to the instrument's internal coordinate system or in some external coordinate system (e.g. project coordinate system). In many cases, the object of interest is either too large (cf. Fig. 1) or complex-shaped to be scanned from one position only. Therefore, multiple scanning stations are usually needed. To obtain a complete representation of the scanned object, the data from different scanning stations need to be referred to a common coordinate system. For this, data can be transformed (also known as registering) into a selected coordinate system during the post-processing stage of the surveys. Also, surveys can be conducted directly in a common coordinate system on site by orienting the TLS instrument using survey control network points. Note that modern TLS instruments, similarly to other geodetic instruments (e.g. total stations), can be centred over a known ground control point and be oriented using back-sighting to a known control point. It is also possible to use resectioning (in surveying also known as free stationing) for orientation which is beneficial on construction sites where the occupation of a pre-established control point may not be possible. In addition, some modern scanners are also equipped with traverse functions that enable establishing control networks required for example in building surveying and in road surveying (GSA 2009, Caltrans 2011, BIM Task Group 2013).

Today TLS has become a standard tool in geodetic surveying. The impetus for this has been the quite rapid development of the TLS technology in recent

years. Due to the technological developments, TLS instruments have become more efficient, for example, data acquisition rates have increased within a decade from approximately 2 kHz up to 1 MHz. The user interface of instruments has become easy to handle and is rather similar to that of traditional geodetic instruments that surveyors are accustomed to. In terms of data processing, over the years different commercial and open source software has become available.

TLS technology, in general, is based either on time-of-flight (TOF) principle or continuous-wave principle. The latter is generally known as the phase-shift (PS) principle. From the user's perspective, the main differences between the two technologies are the data acquisition time, working range and the dependence on environmental conditions.

The TOF technology utilizes laser pulse measurement, the succeeding measurement is only carried out after the detection of the backscattered echo of the emitted laser beam. Due to this time delay, the data acquisition rate of TOF scanners is limited (usually <50 kHz). Since the TOF technology generally implements a high concentration of transmitted laser power, the possible measuring distances can exceed a kilometre. In addition, TOF scanners are, in general, more resistant to environmental conditions (e.g. air humidity), thus making these scanners suitable for outdoor applications (Schulz 2007, Lerma García *et al.* 2008, Vosselman and Maas 2010).

The PS scanners, on the other hand, being based on continuous wave laser principle, are able to acquire data at a rate exceeding 1 MHz. Generally, due to the atmospheric attenuation of the laser signal, PS scanners measure shorter distances (~100 m) and are more sensitive to environmental conditions, especially air humidity and precipitation (Schulz 2007, Lerma García *et al.* 2008, Vosselman and Maas 2010).

The most recent scanning technologies implement for example an enhanced TOF principle that uses the waveform digitizing (WFD) technology. This allows faster data acquisition rates up to 1 MHz with scanning distances exceeding 250 m and better distance measuring accuracies compared to the common TOF principle (Bayoud 2006, Maar and Zogg 2014).

In conclusion, due to remote measurements, moderate measuring distances and very fast data acquisition rates TLS has become a very efficient tool. The advantages of TLS can be summarized as follows:

- Fast and accurate reconstruction of 3D spaces;
- Reduction of data acquisition costs and shortening fieldwork (Reshetyuk 2009);
- Reduction of the need for possible re-survey;
- Improving surveyor safety (e.g. hazardous objects);

- Facilitating better information management on AEC/FM projects (BIM Task Group 2013).

1.2. Limitations related to TLS

As TLS provides an excess of data compared with traditional surveying methods, engineers and structural designers have become more aware of the potential of the TLS technology. This includes benefits from better evaluation of the existing spatial (geometry of the object) conditions, performing detailed structural analysis, 3D recording of as-built conditions and improving an overall information management on construction projects. Today the TLS technology has been used in many AEC/FM applications including for example as-built or as-maintained surveys (e.g. Golparvar-Fard *et al.* 2011, Larsen *et al.* 2011, Bosché and Guenet 2014, Wang *et al.* 2015), surveys for building information modelling (BIM) and FM purposes (e.g. Wunderlich 2003, Murphy *et al.* 2013, Xiong *et al.* 2013, **Paper IV**), surveying of different technical infrastructure like roads (**Paper I**, Hiremagalur *et al.* 2009, Akgul *et al.* 2017, Barbarella *et al.* 2017) tunnels (Pejić 2013, Nuttens *et al.* 2014) and bridges (e.g. Tang and Akinci 2012, **Paper II**). The TLS technology has also proven to be beneficial for the monitoring of structural deformations (e.g. Pesci *et al.* 2013, Holst *et al.* 2014, **Papers II and III**, Wunderlich *et al.* 2016, Xuan *et al.* 2016, Yang *et al.* 2017).

Over the years the TLS technology has been used in many different projects; however, two challenging problems exist: (i) gaining sufficient knowledge of the accuracy of the obtained TLS data and (ii) determining the optimal data processing methods.

The present study addresses primarily the first problem: gaining/estimating sufficient knowledge of the accuracy of the TLS data. The accuracy of the TLS survey has been studied by many authors. For example, Barbarella *et al.* (2017) implemented the covariance matrix to estimate the uncertainty of the position of a generic point. Cuartero *et al.* (2010) investigated TLS accuracy by analysing survey point locational errors using coordinate vectors. Chen *et al.* (2016), Xuan *et al.* (2016) and Zhengchun *et al.* (2016) investigated TLS uncertainties by modelling an error ellipsoid. These studies generally focus on survey point uncertainties relative to the TLS coordinate origin rather than with respect to the principal axes of the object itself. In contrast, the present study focuses on estimating along-normal uncertainties (ANU) of TLS surveyed surfaces as these uncertainties have a critical influence on geometric modelling results. The present study makes use of the concept of the combined standard uncertainty (CSU). The CSU originates from the classical theory of geodetic measurement errors (e.g. Bjerhammar 1973) and has been adopted in contemporary guidelines for the measurement industry (JCGM 100:2008). The concept of CSU has been used in many previous studies, for example, Koch (2008) studied CSU for correlated measurements. Alkhatib *et al.* (2009) investigated CSU in the case of

combining both the aleatoric (referred to as irreducible) and epistemic (referred to as reducible) uncertainty quantities. Niemeier and Tengen (2016) used the concept of CSU to model the uncertainty within a geodetic control network adjustment. **Papers II** and **III** investigated CSU, in particular, ANU for the cases of TLS surveying of engineering structures. The present study presents a method to calculate ANU values using the estimates of CSU.

The second challenge concerns the complexity and time consumption of data processing (e.g. Boukamp and Akinci 2007, Golparvar-Fard *et al.* 2011, Bosché and Guenet 2014). Due to the complexity of data processing, it is also possible to obtain different processing results by using different processing methods, for example by using an iterative geometric modelling or a non-iterative modelling. Some issues concerning geometric modelling of TLS data were identified in **Paper IV**. In addition, e.g. Holst *et al.* (2014), Wang *et al.* (2015) and Holst and Kuhlmann (2016) indicated the need for calibrating the obtained TLS measurements. Calibration of measurements is intended to reduce the influence of systematic errors due to the instrumental imperfections of TLS instruments. The calibration parameters can depend on TLS application (Holst *et al.* 2014). These parameters may vary due to the object's reflectance, surveying conditions, instruments used etc. (Holst *et al.* 2014, Wang *et al.* 2015). For geometric modelling of TLS data, in the case of some methods it is also important to provide uncertainty estimates (i.e. ANU values) for each data point after the field surveys have been carried out. The uncertainty estimates are needed for example to properly weight the TLS data to be modelled (e.g. Gruen and Akca 2005, Holst *et al.* 2014, Mao *et al.* 2015). Therefore, to provide reliable laser scanning project results, the data should go through several processing steps: data reduction, data segmentation, data calibration and geometric modelling (Holst *et al.* 2014). These processing steps, in particular data calibration, can make the time lag between the actual surveying and handing over the scanning results to the customer quite long. Such a time lag is a significant limiting factor in the usage of TLS technology in the AEC/FM industry (Boukamp and Akinci 2007, Golparvar-Fard *et al.* 2011, Tang *et al.* 2011, Bosché and Guenet 2014). However, several methods have been proposed to speed up data processing for example for construction quality assessment purposes and for as-built survey purposes using TLS data (Boukamp and Akinci 2007, Bosché *et al.* 2009, Golparvar-Fard *et al.* 2011, Bosché and Guenet 2014).

The insufficient knowledge of the accuracy of the obtained TLS data and the possibility that the results of data processing can differ, make it challenging to assure the reliability and the quality of the obtained results solely relying on TLS data. It is thus quite common that results obtained by TLS are verified using a conventional geodetic surveying method, e.g. precise levelling or total station survey (e.g. Zogg and Ingensand 2008, Rönnholm *et al.* 2009, Nuttens *et al.* 2014, **Papers II** and **III**).

1.3. Objectives of the study

In geodetic surveying, particularly in engineering surveying, it is relevant to be able to assess the expected quality of the surveys both before and after the surveys. Firstly, a prior quality assessment makes it possible to predict the obtainable accuracy of the surveys and plan better the work ahead. By knowing the expected quality of surveys, the surveyor can estimate whether the obtained results are within the acceptable quality limits. Secondly, the quality assessment of the surveying results mitigates risks and improves reliability for the clients. Tang *et al.* (2011) pointed out that quality assurance for TLS surveying results can be done by assessing deviations by (i) computing the minimum Euclidean distance from each survey point to its nearest geometrically modelled surface or (ii) computing point-surface distances along user-specified directions, e.g. the direction of the surface normal.

The objective of the present doctoral thesis is to investigate TLS applications for engineering structure surveys. In particular, a novel method that enables assessing ANU of the surfaces is presented in this thesis (also in **Paper I**). More specific goals are

- (i) elaboration on a method for calculating ANU of surfaces of engineering structures to be surveyed;
- (ii) adapting a classical concept of the error propagation law of random variables in investigating TLS uncertainties for engineering applications.

These complement the wide range of methods proposed in the literature for assessing TLS surveying accuracy. An investigation of ANU occurring in the surveying of engineering structures is also presented. The methodology for calculating ANU values was tested and rigorously proved by the results achieved in two geodetic surveying case studies. The first case study deals with monitoring bridge deformations occurring during a unique bridge load test where the collapse of the bridge was expected due to extreme loading (**Paper II**). The second case study deals with investigating the range and spatial distribution of frost heave (the occurrence of which is common in seasonal frost regions) of roads (**Paper III**). The developed method for calculating ANU values (**Paper I**) proved to be beneficial for surveying projects where deformations are numerically small and repetition of the measurements is impossible (**Papers II and III**).

In addition to the wide range of applications of TLS in the AEC/FM industry (see the aforementioned literature sources), a number of empirical case studies have been conducted by the author of the present thesis. The conducted empirical case studies (**Papers II to V**) investigate the application of the TLS technology for engineering structure surveys considering the following limitations: (i) scanning under a large angle of incidence (**Papers II, III and**

IV), (ii) the influence of atmospheric conditions on TLS surveying (**Papers III** and **V**) and (iii) validation of the obtained TLS results in engineering applications (**Papers II, III** and **IV**).

The results of the empirical case studies have been published in peer-reviewed journal articles and in international conference proceedings.

In summary, the aims of the present study are to

- (i) study and analyse ANU occurring in the TLS surveying of engineering structures (**Paper I**);
- (ii) study and analyse the application of the TLS technology for engineering structure surveys (**Papers II** to **V**).

1.4. Outline of the thesis

The introduction with the literature review provides a brief overview of the current state of the TLS technology, brings out main limitations of using the TLS technology in the AEC/FM industry and defines the problem statement. The rest of the thesis is divided into two parts and is structured as described in the following sections.

The first part of the thesis, which includes Chapters 2 to 5, focuses on the theoretical assessment of TLS uncertainties occurring in the surveying of engineering structures (**Paper I**). The study of the theoretical assessment of TLS uncertainties uses the classical concept of the error propagation law of random variables (e.g. Bjerhammar 1973). Investigations are carried out to determine the influence of the distance and the angle measurement uncertainties (horizontal and vertical angle) to the CSU of a survey point. In particular, the emphasis is on ANU with respect to the surface to be surveyed. A method is derived on the basis of CSU to calculate ANU values for the general cases. In addition, the magnitudes and the distribution of ANU values across the surfaces are investigated based on computer-simulated engineering structures. The study includes suggestions to optimize scanning locations in order to reduce ANU values. The modelling of ANU distribution for engineering structures concludes the first part of the thesis.

The second part of the thesis, from Chapter 6 onwards, focuses on the application of the TLS technology for engineering structure surveys. The developed method for calculating ANU values, as described in Chapter 3, was tested in two empirical case studies. The first case study deals with monitoring deformations occurring during a unique static bridge loading using the TLS technology (**Paper II**). The results obtained by TLS were verified by precise levelling. The second case study deals with the monitoring of road surface deformations occurring due to frost heave at selected road sections using the TLS technology (**Paper III**). The results obtained by TLS were verified by

geometric levelling. Both of the mentioned case studies generally focus on detecting structural deformations in the vertical (either down- or upwards) direction.

Applications of TLS, in particular for road surveying purposes, are investigated with a case study dealing with road surface surveying using TLS and total station technologies (**Paper V**). The optimal scanning distance and the effectivity of using TLS in road surveys are studied. Also, two surveying technologies, the TLS surveying and the traditional total station surveying, are compared (**Paper V**).

Lastly, the application of the TLS technology for building surveying is investigated (**Paper IV**). The study highlights benefits and problematic areas of using TLS data for the purpose of compiling parametric building models for the FM industry. The geometrical accuracy of the created model was verified using pointwise total station survey data.

The conclusions and the discussion on further research needs conclude the thesis.

2. TLS MEASUREMENTS AND UNCERTAINTY

2.1. Relevant statistical estimates of measurements and uncertainty

Every measurement can contain errors. The measurements of the same quantity may yield different values, the difference is called discrepancy. If discrepancies are only of a small magnitude (below a certain threshold), the observations can be referred to as being precise. However, these results may not be accurate, since their definitions are different (Chilani and Wolf 2006, Schofield and Breach 2007):

- (i) precision is described by the compatibility rate between the repeated observations, showing how close the observation results are to each other;
- (ii) accuracy is described by the absolute closeness of the observed value and the true value.

Measurement precision is assessed through measurement uncertainty, which is generally denoted by u (Fig. 2).

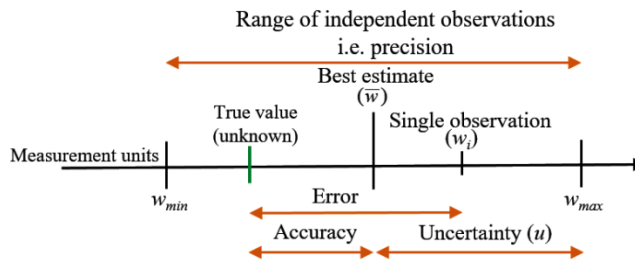


Figure 2. Relations between the true value, the best estimate \bar{w} (i.e. mean value), single observation w_i and measurement uncertainty u (adopted from Ehrlich 2014).

An error is the difference between the measured quantity and the true quantity (i.e. true value, cf. Fig. 2). Since in many occasions the true quantity is unknown, the deviation, i.e. the difference between the measured quantity and the estimated quantity (e.g. the mean value) is used (Eq. 2.1). Uncertainty is a non-negative parameter that describes the dispersion of the obtained quantities within the vicinity of the best estimate value, i.e. the mean value (JCGM 100:2008, Śladek 2016). The larger the measurement uncertainty, the lower is the measurement precision. The parameters for uncertainty can be for example the standard deviation (Eq. 2.2) or the combined standard uncertainty, i.e. CSU (Eq. 2.3).

$$\bar{w} = \frac{\sum_{i=1}^n w_i}{n}, \quad (2.1)$$

$$Std(w) = \sqrt{\frac{\sum_{i=1}^n (w_i - \bar{w})^2}{n-1}}, \quad (2.2)$$

and

$$u_{\hat{P}}^2 = \sum_{i=1}^n \left(\frac{\partial f}{\partial w_i} \right)^2 u_{w_i}^2, \quad (2.3)$$

where n is the total number of observations, $u_{\hat{P}}$ is the combined standard uncertainty of a survey point, u_{w_i} is the standard uncertainty of an i -th observable quantity (e.g. distance, angle, height difference etc.), \hat{P} is an estimate of the location (3D position, expressible via specific x , y and z -coordinates) of the true location of the survey point P , f is the function $P = f(w_i)_{i=1,\dots,n}$ associated with the observations $(w_i)_{i=1,\dots,n}$. For instance, the coordinates can be derived from observables by

$$\begin{bmatrix} x_i \\ y_i \\ z_i \end{bmatrix} = \begin{bmatrix} \rho_i \cos \theta_i \cos \varphi_i \\ \rho_i \sin \theta_i \cos \varphi_i \\ \rho_i \sin \varphi_i \end{bmatrix}_{i=1,\dots,n}, \quad (2.4)$$

where ρ is the distance, θ is the horizontal angle accounted from the TLS device's x -axis, φ is the vertical angle (e.g. accounted from the horizontal plane).

The knowledge of the accuracy and precision of the surveying equipment is critical in order to meet the requirements of a survey project. However, due to the novelty and the complexity of the TLS technology, independent and reliable testing procedures provided by e.g. International Organization for Standardization (ISO) or German Institute for Standardization (DIN) are still missing for TLS (Tsakiri *et al.* 2015, Holst and Kuhlmann 2016, Pandžić *et al.* 2017). Such procedures exist for ordinary geodetic instruments, for example for levelling instruments (ISO 17123-2:2001) and for total stations (ISO 17123-5:2012). At present, according to ISO (iso.org) a standard for testing terrestrial laser scanners, under the name of ISO 17123-9, is under development.

Nevertheless, once the standard is available, the application of these standardized methods by the manufacturers of scanners will take some time. For the time being, the users of the TLS technology mainly rely on the accuracy characteristics provided by the manufacturers of scanners. The absence of uniform knowledge of the accuracy of TLS instruments makes it difficult to classify and make a selection from different brands and technologies for the use in a specific surveying project. The accuracy characteristics can be considered essential since the AEC/FM industry comprises the majority of the customers of the TLS hardware, software and service markets (Higgins 2007). In addition Bosché (2012) reported that for example the US General Services Administration (GSA), one of the world's largest facility owners, has strongly encouraged the use of TLS for building surveys. The use of the TLS technology in the AEC/FM industry shows a growing trend. Not knowing the quality of the obtained TLS survey data in terms of accuracy weakens the reliability of the obtained results.

2.2. TLS related uncertainties

2.2.1. Factors affecting TLS accuracy

TLS instruments, like any other conventional geodetic instruments, are influenced by many factors affecting the surveying accuracy and thus the final results. In combination, these factors increase measurement uncertainty. The factors affecting TLS accuracy are identified as follows:

- (i) Uncertainties caused by the user, i.e. human errors (also including the operator's mistakes). At engineering surveying, it is expected that the operator has basic land surveying and data processing skills, including a theoretical background and practical surveying experience. Thereby the operator is capable of minimizing and quantifying possible surveying errors by better planning the scanning works (Chilani and Wolf 2006, Schofield and Breach 2007, Hodge 2010). In laser scanning, human errors can occur for example due to insufficient placement and the number of used TLS targets for data registration purposes, unfavourable locations of TLS instruments and incorrect data processing.
- (ii) The metrological specifications of the TLS instruments used. The problem with the available TLS specifications is that they are obtained using calibration procedures not set by ISO or DIN standards (Gottwald 2008, Tsakiri *et al.* 2015, Pandžić *et al.* 2017).
- (iii) Uncertainties caused by the object's physical properties. Object-related uncertainties due to surface roughness, colour, temperature and moisture etc. are reported to have an influence on the scanning results by e.g. Määttä *et al.* (1993), Kersten *et al.* (2005), Pesci and Teza (2008), Hejbudzka *et al.*

(2010), Lichti (2010), Soudarissanane *et al.* (2011), Krooks *et al.* (2013) and Roca-Pardiñas *et al.* (2014).

(iv) A TLS survey can also be influenced by systematic errors. The sources of systematic errors are generally due to the imperfections of TLS instruments (Chow *et al.* 2012, Holst *et al.* 2014) and objects physical properties (Kersten *et al.* 2005 and 2009, Reshetyuk 2009). The presence of systematic errors and methods to minimize their effects are reported in many studies e.g. Reshetyuk (2009), Chow *et al.* (2012), Abbas *et al.* (2013), Tsakiri *et al.* (2015) and Holst and Kuhlmann (2014 and 2016).

In addition, a considerable number of researchers have investigated the effects of scanning geometry on TLS accuracy. The following section gives a brief overview of the matter as one of the factors affecting TLS accuracy.

2.2.2. Uncertainties due to scanning geometry

Scanning geometry describes the location of the scanning instrument with respect to the object of interest. The scanning geometry influences for example the density of the surveyed points on the surface and the angle of incidence values (Fig. 3).

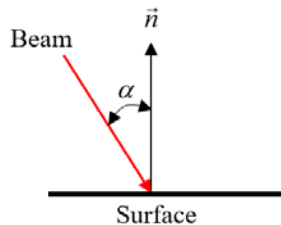


Figure 3. Angle of incidence (α), accounted with respect to the surface normal (\vec{n}).

The influence of the angle of incidence on TLS uncertainty is studied for example by Lichti (2007), Kaasalainen *et al.* (2009), Kersten *et al.* (2009), Soudarissanane *et al.* (2009 and 2011), Krooks *et al.* (2013) and Soudarissanane (2016). Many of these studies report that TLS measurement noise is mostly influenced by the scanning geometry. A large angle of incidence leads to the spreading of the laser footprint on the surface. The energy of the signal within the footprint does not therefore obey a symmetrical Gaussian distribution. This will increase the rise time of the backscatter signal pulse to reach a certain threshold for the returned signal to be registered precisely. Thus surveying noise is likely to occur (Deems and Painter 2006, Schaer *et al.* 2007, Vosselman and Maas 2010).

According to Lichti (2007), Soudarissanane *et al.* (2009 and 2011) and Soudarissanane (2016), the critical limit of the angle of incidence is reached

already at 60° . Exceeding this threshold yields a sharp increase in the overall noise. It should be noted that the aforementioned studies focused only on PS scanners. Less noise occurs when scanning under a smaller, i.e. near-zero angle of incidence values. At a near-zero angle of incidence the maximum backscatter signal power (i.e. the intensity of the emitted signal) is obtained (Weichel 1990, Hancock 1999, Wagner *et al.* 2006, Pesci and Teza 2008). Kaasalainen *et al.* (2009) explained that the digital signal processor in the TLS signal receiver unit of PS scanners optimizes the power of the backscatter signal, enabling thus the scanner to produce better results at a near-zero angle of incidence.

An empirical study by Kersten *et al.* (2009) investigated the effects of angle of incidence using both PS and TOF scanners. In the case of PS scanners, Kersten *et al.* (2009) reported similar results as reported, for example, by Soudarissanane *et al.* (2011). In contrast, TOF scanners did not exhibit significant effects due to the change of angle of incidence. The study by Kersten *et al.* (2009) thus concluded that a large angle of incidence is not critical in the case of TOF scanners.

Engineering surveying often deals with uneven and coarse-grained surfaces (e.g. historic and pre-manufactured contemporary structural elements). Thus a laser signal at a near perpendicular angle of incidence (i.e. 90° with respect to the surface normal) may easily backscatter from such coarse-grained surfaces. Nevertheless, further derivations aim to include the possible influence of the angle of incidence on ANU.

3. THE RESULTING METHOD FOR UNCERTAINTY ESTIMATION

Since the TLS technology has been used in many fields in the AEC/FM industry (e.g. in as-built surveys and quality assessment), there is a need for a method to estimate the range and spatial distribution of TLS uncertainties occurring during surveying of engineering structures. The users of TLS data are mainly interested in uncertainties in the direction of surface normal, i.e. ANU, as these influence most the geometric modelling of TLS data. The knowledge of the probable magnitudes of the ANU of a particular TLS instrument helps to better plan different scanning activities for different projects.

3.1. Development of the ANU calculation method

A methodology was developed in this study for calculating ANU values for engineering structures. This methodology allows conducting *a priori* quality assessment of the expected scanning results (**Paper I**). For this, the basic concept of CSU presented by Eq. 2.3 from JCGM 100:2008 was used, which originates from the classical theory of error propagation law of random variables (e.g. Bjerhammar 1973). For investigating the behaviour of ANU, various surveying scenarios were computer-simulated and studied. Theoretical derivations were numerically verified, and these results were compared with the results of previous empirical studies. The influence of along-normal noise on geometric modelling of surveyed surfaces was studied. In addition, suggestions were made for optimizing scanning locations that would yield reduced ANU values. The following sections elaborate on the method for calculating ANU values for the general surveying case.

In the general surveying cases the object's "natural" coordinate system is not parallel to the TLS coordinate system (see more detailed discussion of orientations of coordinate systems in **Paper I**). Point location uncertainty in the surface normal direction, as the developed method proposes, can be calculated stepwise: (i) calculating the horizontal angle (ω) between the x -axis (in the TLS system) and X -axis (in the object's system), (ii) calculating the inclination angle (ν) between the z -axis (in the TLS system) and the Z -axis (in the used object's system), (iii) projecting the axial CSU values ($u_{\hat{x}}$, $u_{\hat{y}}$ and $u_{\hat{z}}$ derived using Eqs. 3.3, 3.4 and 3.5, to be explained further on) onto the surface normal using the error propagation law of random variables.

The surface's horizontal rotation angle (ω) between the TLS coordinate system's x -axis and the object's X -axis in the 2D plane can be calculated by using the coordinates x and y of arbitrary points B and P on the xy -plane on the surface (cf. Fig. 4):

$$\omega = \tan^{-1} \frac{y_B - y_P}{x_B - x_P}. \quad (3.1)$$

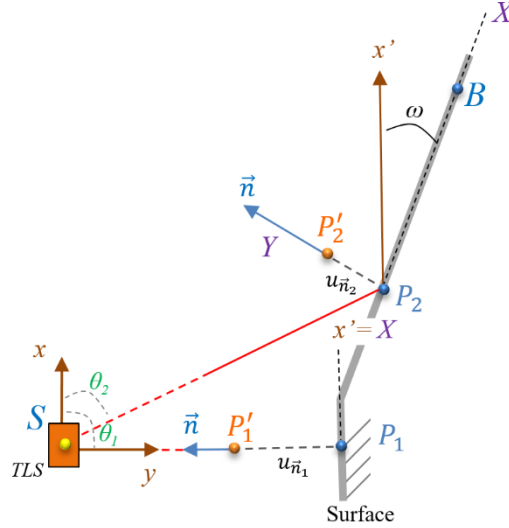


Figure 4. Top view of the vertical sub-surfaces, the furthest one being horizontally rotated to an angle ω (around z -axis) between the TLS coordinate system's x -axis and the object's X -axis. The uncertainties $u_{\vec{n}_1}$ and $u_{\vec{n}_2}$ are parallel to the object's Y -axis and coincide thus with the surface normal. Points P'_1 and P'_2 are shifted along the surface normal from their actual locations P_1 and P_2 due to the uncertainty in the surface normal direction ($u_{\vec{n}}$). θ_1 and θ_2 are the horizontal angles with respect to the TLS coordinate system's x -axis. Note that x and x' are parallel to each other.

The surface's inclination angle can be calculated using the coordinates y and z of an arbitrary surface point A that is located either above or below the point P (cf. Fig. 5):

$$\nu = \tan^{-1} \frac{y_A - y_P}{z_A - z_P}. \quad (3.2)$$

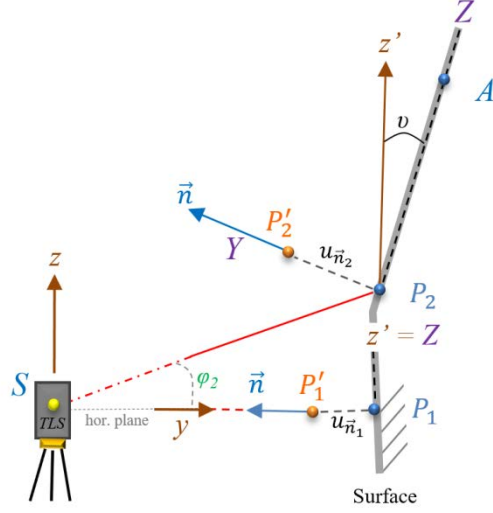


Figure 5. Side view of sub-surfaces, the top one is vertically inclined at an angle v (around the x -axis) between the surveying coordinate system's z -axis (z) and the object's coordinate system's z -axis (Z). The uncertainties $u_{\bar{n}_1}$ and $u_{\bar{n}_2}$ are parallel to the surface's Y -axis. Points P'_1 and P'_2 are shifted along the surface normal from their actual locations P_1 and P_2 due to the uncertainty in the surface normal direction ($u_{\bar{n}}$) and φ_2 is a vertical angle measured from the horizontal direction. Note that z and z' are parallel to each other. A is an arbitrary surface point.

The CSU equations for $u_{\hat{x}}$, $u_{\hat{y}}$ and $u_{\hat{z}}$ (Eqs. 3.3, 3.4 and 3.5, respectively) are obtained using the partial derivatives of TLS observations (Eq. 2.4) with respect to each variable (i.e. for x , $dx/d\rho$; $dx/d\varphi$; $dx/d\theta$; analogously, also for the y - and z -components, for more details see **Paper I**), and then inserted into Eq. 2.3, incorporating also the uncertainty parameters stemming from the results of the instrument's individual calibration or by the manufacturer.

$$u_{\hat{x}} = \left[\cos^2 \theta \cos^2 \varphi u_{dist}^2 + \rho^2 \cos^2 \varphi \sin^2 \theta u_{h.angle}^2 + \rho^2 \cos^2 \theta \sin^2 \varphi u_{v.angle}^2 \right]^{\frac{1}{2}}, \quad (3.3)$$

$$u_{\hat{y}} = \left[\sin^2 \theta \cos^2 \varphi u_{dist}^2 + \rho^2 \cos^2 \varphi \cos^2 \theta u_{h.angle}^2 + \rho^2 \sin^2 \theta \sin^2 \varphi u_{v.angle}^2 \right]^{\frac{1}{2}}, \quad (3.4)$$

$$u_{\hat{z}} = \left[\sin^2 \varphi u_{dist}^2 + \rho^2 \cos^2 \varphi u_{v.angle}^2 \right]^{\frac{1}{2}}, \quad (3.5)$$

where $u_{\hat{x}}$, $u_{\hat{y}}$ and $u_{\hat{z}}$ are the calculated CSU values along the respective TLS axes; u_{dist} is the scanner's standard distance uncertainty, $u_{h.angle}$ is the scanner's standard horizontal angle and $u_{v.angle}$ vertical angle uncertainty, respectively.

The ANU for the general cases can be calculated by projecting CSU values onto the surface normal. For the projection, right triangles can be formed using the calculated CSU values (Fig. 6). The CSU component ($u_{\hat{x}}$, $u_{\hat{y}}$ or $u_{\hat{z}}$) is the hypotenuse of the right triangle formed (cf. Fig. 6).

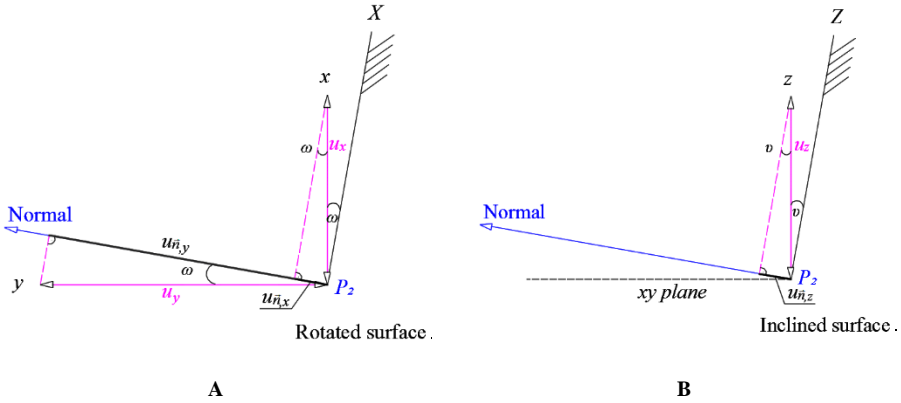


Figure 6. Geometric relations between CSU and the surface normal. (A) Top view of relations between CSU and the surface that is horizontally rotated to an angle (ω). (B) Side view of the case when the surface is vertically inclined to an angle (ν). $u_{\hat{n},x}$, $u_{\hat{n},y}$ and $u_{\hat{n},z}$ are axial uncertainties projected onto the surface normal.

After all the CSU components have been projected (using trigonometric relations in the formed triangles) onto the surface normal, using the error propagation law of random variables (e.g. Bjerhammar 1973), the ANU values are calculated for general cases by the following expression:

$$u_{\hat{n}} = \left[\sin^2 \omega u_{\hat{x}}^2 + \cos^2 \omega u_{\hat{y}}^2 + \sin^2 \nu u_{\hat{z}}^2 \right]^{\frac{1}{2}}, \quad (3.6)$$

where $u_{\hat{n}}$ is the sought uncertainty in the surface normal direction for the general case.

The maximum ANU estimates occur in special cases where the TLS axes and the object's axes are parallel (see a more detailed discussion of orientations of coordinate systems in **Paper I**). This is also considered as the worst case scenario. An investigation is carried out to reveal the correlations between the independent variables (angles and distances) with the ANU values. For this the TLS x -axis and the object's x -axis are taken to be parallel, thus the surface normal is parallel with the y -direction. The measured quantities θ and φ become 90° and 0° , respectively. In such a case, the ANU value is calculated using Eq. 3.4, which due to the properties of sine and cosine functions at 90° or 0° , eventually reduces to u_{dist} only (see Eq. 3.7). This indicates that ANU is correlated with the values of the measured angles θ and φ (cf. results in Fig. 7).

$$\begin{aligned}
u_{\hat{y}} &= \left[\sin^2 \theta \cos^2 \varphi u_{dist}^2 + \rho^2 \cos^2 \varphi \cos^2 \theta u_{h.angle}^2 \right. \\
&\quad \left. + \rho^2 \sin^2 \theta \sin^2 \varphi u_{v.angle}^2 \right]^{\frac{1}{2}} \xrightarrow{\text{with } \theta=90^\circ \text{ and } \varphi=0^\circ} \\
&\rightarrow \left[\sin^2 \theta \cos^2 \varphi u_{dist}^2 \right]^{\frac{1}{2}} = u_{dist} .
\end{aligned} \tag{3.7}$$

A numerical example of the worst case scenario is provided based on simulated data points that form a horizontal line on a vertical wall. The scanner is located at an arbitrary distance from the object, in this case, 4.3 m, a realistic surveying distance from an object. Metrological characteristics of an instrument are generally provided by manufacturers at a 68.3% (one sigma) confidence level. To have a more practical accuracy estimate, the characteristic must be multiplied by the factor 3, increasing the confidence level to 99.7% (three sigma), which is the generally accepted uncertainty tolerance in surveying. Therefore, rather than using the typical metrological parameter values of $u_{dist} = 0.004$ m and $u_{h.angle} = 12''$ (which are, for example, associated with widely-used TOF scanners, e.g. Leica C10 and Leica P20), three times larger values are used: $u_{dist} = 0.012$ m and $u_{h.angle} = u_{v.angle} = 36''$ in numerical verifications.

The results of the numerical example of the worst case scenario are illustrated in Fig. 7. A maximum ANU value of $u_{\hat{y}} = 0.012$ m is obtained, as expected (cf. Eq. 3.7), when θ is equal to 90° , at the closest distance to the scanner (i.e. 4.3 m). In the example (Fig. 7), as the distance (ρ) increases, the angle of incidence (α) also increases, whereas the horizontal angle (θ) decreases. The relationship between α and θ is in this case simply $90^\circ - \theta = \alpha$.

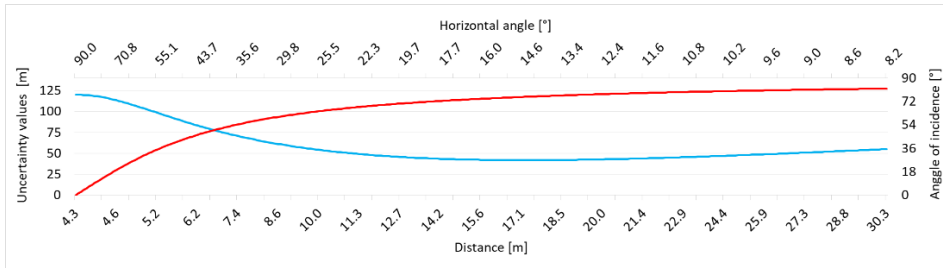


Figure 7. Calculated uncertainties of a horizontal line on a vertical wall. The blue line indicates ANU (values on the left-hand vertical scale); the red line indicates the angle of incidence (values on the right-hand vertical scale). The horizontal angle θ (top horizontal scale) at the closest point of 4.3 m equals 90° (i.e. $\alpha = 0^\circ$) and at the longest distance (30.3 m) approx. 8° (corresponding thus to the angle of incidence 82°).

In general, ANU values decrease (i.e. the accuracy of measurements increases) from the point where θ is equal to 90° (the angle of incidence is 0°) until reaching their minimum (i.e. the most accurate point) at approximately 17 metres from the scanner θ of 14° , i.e. $\alpha = 76^\circ$ (Fig. 7). This is because the influence of u_{dist} (0.012 m) decreases as the value of $\sin(\theta)$ decreases, cf. Eq. 3.7. Then ANU gradually begins to increase due to the increasing influence of the distance (ρ). Also, the value of $\cos(\theta)$ increases as θ decreases from 90° to zero. Apparently, increasing thus the angle of incidence affects ANU only insignificantly, cf. Fig. 7.

4. APPROBATION OF THE DEVELOPED METHOD

The following section provides the numerical verification of the derived ANU calculation method (Eq. 3.6). The achieved ANU values are compared to geometrical uncertainties (cf. Section 4.2.) and are also confirmed with those of previous empirical studies.

4.1. Set-up of the experiment

For verification purposes, a vertical surface that is horizontally rotated from its initial direction (i.e. $\omega = 0^\circ$) will be simulated, as in the empirical studies by Soudarissanane *et al.* (2009, 2011) and Soudarissanane (2016). In these studies, a PS type of TLS was located at a distance (20 m) from a plane-like surface which was rotated to different angles in increments of 10° within the interval $[0^\circ \leq \omega \leq 80^\circ]$, cf. Fig. 8. For each 10° turn, the surface was modelled from the TLS point cloud, and modelling residuals (i.e. deviations from the actual surface) were estimated. The goal of these empirical studies was to identify the effect of the angle of incidence (α) from the surveying results.

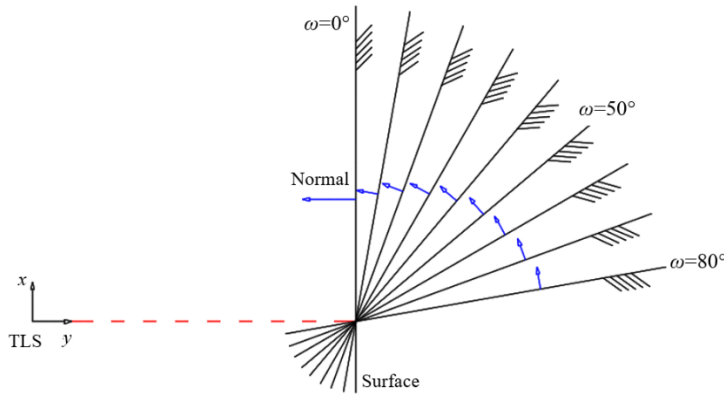


Figure 8. Top view of a vertical plane-like surface that is horizontally rotated $[0^\circ \leq \omega \leq 80^\circ]$ by an angle ω in increments of 10° . The red dashed line illustrates the laser beam from the scanner to the surface contact point (remains at a constant distance). The direction of the surface normal at different angles ω is shown by the blue arrows.

In the present example, as the surface is rotated only horizontally, both $u_{\hat{x}}$ and $u_{\hat{y}}$ have an effect on ANU. The third component, $u_{\hat{z}}$, can be neglected in this case since it describes uncertainty in the vertical direction. In order to follow the worst case uncertainty scenario (cf. Eq. 3.7), the TLS measurable quantities θ and φ are taken to be 90° and 0° , respectively. Initially, at $\omega = 0^\circ$, the surface normal is parallel to $u_{\hat{y}}$ (Fig. 8), and CSU values are calculated (by

Eqs. 3.3 and 3.4) to be $u_{\hat{x}} = 0.003$ m and $u_{\hat{y}} = 0.012$ m, respectively. Note that the effect of $u_{\hat{x}}$ on the surface normal can be completely neglected at $\omega = 0^\circ$, as this is uncertainty along the surface. In the contrasting case of $\omega = 90^\circ$, the ANU becomes equal to $u_{\hat{x}}$ only, as $\lim_{\omega \rightarrow 90^\circ} f(u_{\hat{n}}) \rightarrow u_{\hat{x}}$.

The numerical results of ANU values of the simulated surface are presented in Fig. 9. For the gradually rotated (with respect to the initial direction, $\omega = 0^\circ$) surface (see Fig. 8) the numerical values of the ANU are calculated by Eq. 3.6 using the $u_{\hat{x}}$ and $u_{\hat{y}}$ components.

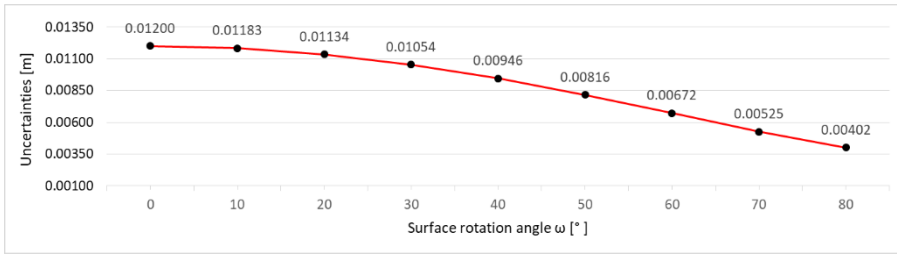


Figure 9. Results of the ANU of TLS survey points on a vertical surface that is horizontally rotated by the angle ω ; the rotation interval is $[0^\circ, 80^\circ]$ with the increments of 10° . The distance from the TLS to the surface is 20 m. Units in metres.

The results in Fig. 9 reveal that the ANU values decrease gradually as the angle ω increases. Notably, the numerical results at $\theta = 90^\circ$ and $\omega = 0^\circ$ (the y -axis is parallel to the surface normal) are influenced by u_{dist} only (cf. Eq. 3.7).

4.2. Geometrical proof of ANU

The achieved ANU values are first compared to geometrical uncertainties that are alternatively derived from the geometrical relations using the law of sines in conjunction with the measuring uncertainties u_{dist} and $u_{h.angle}$ (cf. Fig. 10):

$$u_{dist.h.angle} = \sqrt{(\rho_{h.angle} - \rho)^2 + u_{dist}^2}, \quad (4.1)$$

where $u_{dist.h.angle}$ is the total uncertainty (i.e. uncertainty in the direction of the laser beam) due to the distance measurement associated uncertainties $u_{h.angle}$ and u_{dist} , the scanner's standard horizontal angle measurement uncertainty and

the standard distance measurement uncertainties, respectively; $\rho_{h.angle}$ is the distance due to angular uncertainty ($u_{h.angle}$) obtained using the law of sines:

$$\frac{\rho}{\sin \tau} = \frac{\rho_{h.angle}}{\sin \gamma} \Rightarrow \rho_{h.angle} = \frac{\rho \sin \gamma}{\sin \tau}, \quad (4.2)$$

where a triangle is formed (Fig. 10A) using the distance ρ , which is also a side of the formed triangle; τ is the angle opposite to the side ρ and γ is the angle opposite to the side $\rho_{h.angle}$.

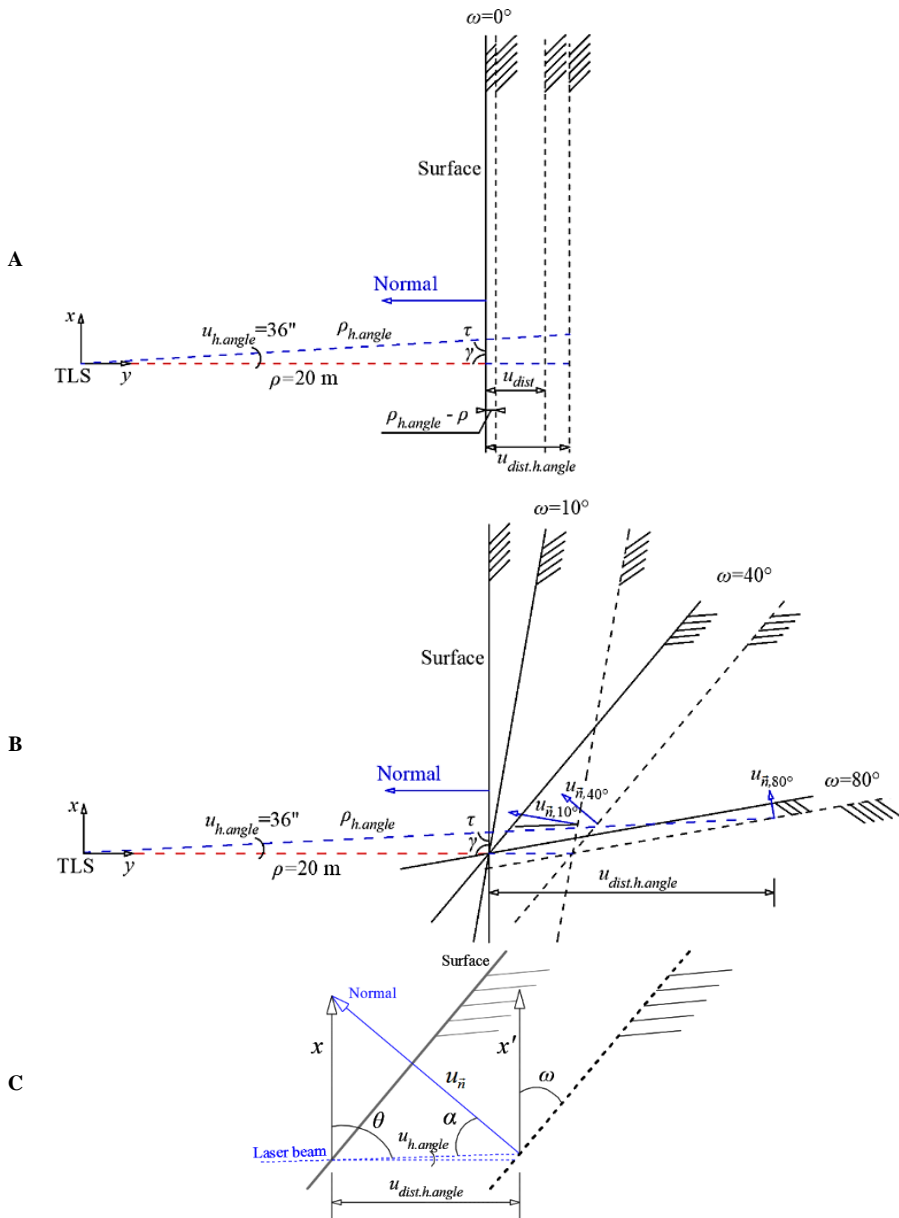


Figure 10. Geometrical relations between the ANU components and the surface of interest. (A) Top view of uncertainties in the direction of the laser beam ($u_{dist,h,angle}$), where $\rho_{h,angle}$ is the increased distance due to angular uncertainty $u_{h,angle}$, τ is the angle opposite the side ρ and γ is the angle opposite the side $\rho_{h,angle}$. The red dashed line indicates the true laser beam; the blue dashed line indicates the deviated laser beam; the solid line indicates the true location of the surface; the first dashed line (starting

from the left-hand side) indicates the surface's locational shift due to the lengthening of the laser beam by $(\rho_{h.angle} - \rho)$; the second dashed line indicates an additional shift due to the u_{dist} effect; the third dashed line is the total shift of the surface by $u_{dist.h.angle}$. **(B)** Uncertainties when the surface is rotated to different angles (ω) where $u_{\bar{n},10^\circ}$, $u_{\bar{n},40^\circ}$ and $u_{\bar{n},80^\circ}$ are the ANU at $\omega = 10^\circ, 40^\circ$ and 80° , respectively. **(C)** The geometric relations between the horizontal angle (θ), the angular uncertainty $u_{h.angle}$, the angle the surface is horizontally rotated to (ω) and the angle of incidence (α) are used to calculate the ANU ($u_{\bar{n}}$). Note that x and x' are parallel to each other.

The uncertainty in the direction of the laser beam is projected onto the surface normal using geometric relations (Fig. 10C):

$$u_{\bar{n}} = u_{dist.h.angle} \cos \alpha, \quad (4.3)$$

where the angle of incidence (α) can be determined by (Fig. 10C):

$$\alpha = 90^\circ - \theta + \omega. \quad (4.4)$$

For surfaces tilted with respect to the z -axis, the contribution of $u_{v.angle}$ can be accounted for by adding an additional term to Eq. 4.1:

$$u_{dist.h.angle} = \sqrt{(\rho_{h.angle} - \rho)^2 + u_{dist}^2 + u_{v.angle}^2}. \quad (4.5)$$

Therefore, by using Eq. 4.5 similar geometrical verifications (and plots) can be generated (by analogy) in the case of a vertically tilted surface.

4.3. Verification of numerical results

The results of the geometrically derived ANU (cf. Eq. 4.3) are presented in Fig. 11. The results indicate that uncertainties in the direction of the laser beam (yellow line, cf. Eq. 4.1) have a steep increase at larger surface rotation angles (ω). The projected ANU values (grey line, cf. Eq. 4.3) are identical to the results obtained by the proposed method using Eq. 3.6 (cf. Fig. 9 and Fig. 11).

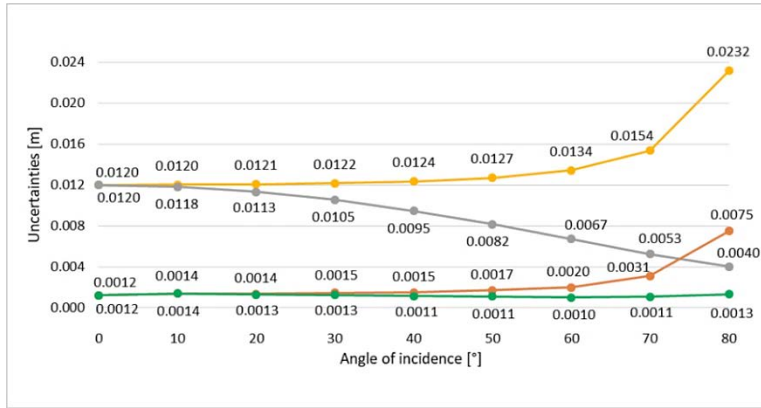


Figure 11. A comparison of the ANU estimated by the present study and that of the Soudarissanane *et al.* (2011) empirical study. The yellow line indicates uncertainties in the direction of the laser beam, derived from the geometric relations; the grey line indicates the ANU derived using Eq. 3.6, also equal to the numerical outcome to the geometrical uncertainties (cf. Eq. 4.3); the orange line indicates the (reconstructed) uncertainties in the direction of the laser beam estimated by Soudarissanane *et al.* (2011); and the green line indicates the (reconstructed) ANU estimated by Soudarissanane *et al.* (2011). The distance to the surface is 20 m in all cases.

The achieved ANU results are compared (cf. Fig. 11) with the results of previous empirical studies by Soudarissanane *et al.* (2009 and 2011) and Soudarissanane (2016). The residuals obtained by their empirical studies describe the noise in the direction of the laser beam (Fig. 11 orange line). The difference between the orange and the yellow graphs appears to occur due to a scaling factor (u_{dist} e.g. 0.012 m). The comparison results suggest thus that the manufacturer's specifications used in the present study could be somewhat too pessimistic. Arguably more accurate u_{dist} estimates can be obtained using the individual TLS calibration results, hence yielding a better agreement between the theoretical and empirical values.

The differences between the ANU results of the previous empirical studies (Fig. 11 green line) and the theoretical ones derived in this study (Fig. 11 grey line) decrease with the increasing angle of incidence. This is due to the difference in the magnitudes of the empirically obtained and the theoretically determined values of uncertainties in the direction of the laser beam (Fig. 11 orange and yellow lines), and due to their $\cos(\alpha)$ relation with the ANU (cf. Eq. 4.3).

Results in Fig. 11 show that the derived method can be used to obtain a realistic assessment of ANU and makes it possible to estimate uncertainties before the actual survey at the survey design stage.

In conclusion, the derived method was verified using the results of previous empirical case studies and geometrical relations.

5. MODELLING OF ANU DISTRIBUTION FOR ENGINEERING STRUCTURES

Further approbation of the ANU is tested on computer-simulated engineering structures, the façades of a building and the lower side of a bridge deck. Noise is then introduced in the data to simulate realistic survey data. These noise-contaminated data are then used for geometrical modelling in order to determine the influence of along-normal noise to the modelling outcome. In addition, optimal scanning locations in case the simulated engineering structures were determined based on the magnitude and the distribution of the calculated ANU values.

5.1. Set-up of the experiment

The ANU investigation was carried out on computer-simulated engineering structures including a building with dimensions of 60.000 m×10.000 m×6.000 m and a bridge deck with dimensions of 60.000 m×10.000 m. For both structures, the two-dimensional point step was chosen to be 0.100 m. The building was thus covered with a total of 85 400 points, whereas the simulated bridge surface consists of 60 701 points. The object's axes were set parallel to the TLS coordinate axes, allowing us to deal with the influences of maximum ANU values for the surveyed surfaces (cf. Section 3.1 worst case scenario).

For the building survey, the scanning stations were chosen at its corners so that two sides would be covered by one station (Fig. 12). This is a realistic surveying scenario. Two additional scanning stations (S4 and S5, cf. Fig 12) were added to obtain data from the potentially most suitable scanning location (S4) and a likely unsuitable location (S5) with respect to the side ④.

The simulated bridge deck data consists of two sets of point clouds acquired from two different scanner locations (Fig. 12). The scanning stations were located (i) under the bridge at the centre of the bridge deck (station B1); (ii) alongside the bridge deck at a horizontal distance of 6.0 m away from the deck (station B2, in practice it would be a riverbank as it was in the case study presented in **Paper II**).

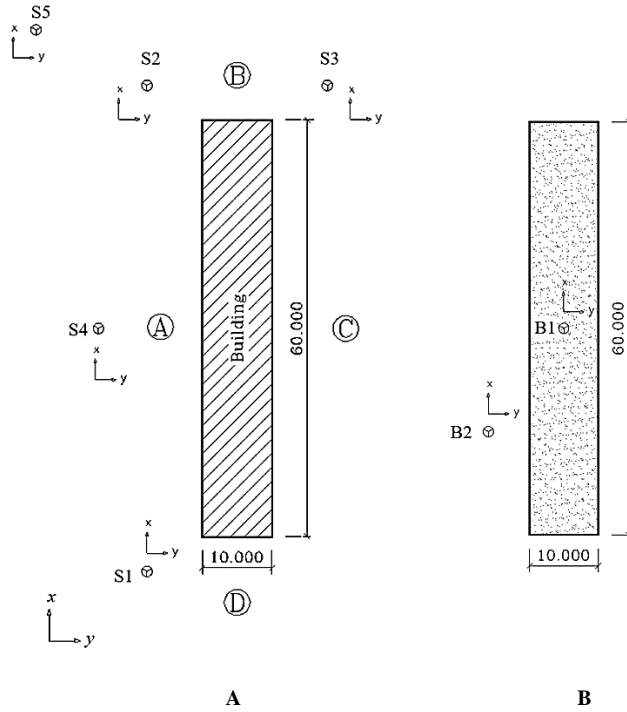


Figure 12. Top view of the locations of the scanning stations. **(A)** scanning locations S1, S2, S3, S4 and S5 for the building survey. The letters **(A)**, **(B)**, **(C)** and **(D)** denote sides of the building. **(B)** The underbridge scanning locations B1 and B2. TLS axes are shown near each scanning location, the object's axes are shown in the left-hand corner of figure **A**. Units are in metres.

5.2. Numerical results

The spatial distribution of uncertainties calculated using Eq. 3.4 (cf. TLS axes in Fig. 12) with the uncertainty parameters $u_{dist} = 0.012$ m and $u_{h.angle} = u_{v.angle} = 36''$ (as used in Section 3.1) indicated that the data from the most remote scanning station (station S5, max distance to the surface approximately 75 m) yielded the largest ANU values compared to other stations, e.g. station S1 or S4 (Fig. 13).

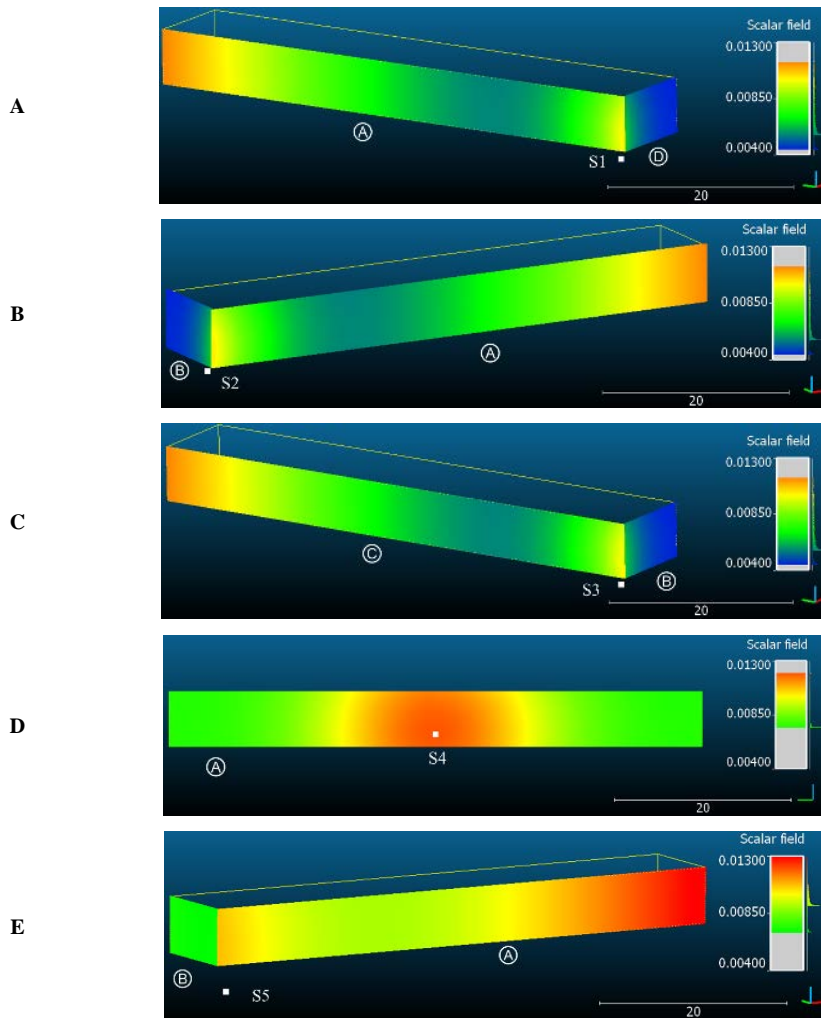


Figure 13. Side views of spatial distributions of ANU along the building façades for scanning stations S1, S2, S3, S4 and S5. The height of the vertical wall is 6 m. The coloured ANU scales are at the right-hand side. The grey colour in the fixed-value scale denotes the non-occurring ANU values in particular surveying cases. Units in metres.

For the building façades, the ANU values from stations S4 and S5 are clearly larger than those for data from stations S1, S2 and S3, while the ANU for data from stations S1, S2 and S3 are almost identical. The larger ANU values for data from station S4 are due to surveying in the perpendicular direction to the surface (α being close to 0° , cf. also Eq. 3.7). Station S5 was deliberately located relatively far from the north-west corner of the building façade (approx. 27 m), and as expected, the largest ANU values are associated with this station. Larger distances are also generally more likely to yield systematic errors, e.g. due to an increase in the backscatter signal to noise ratio (Eling 2009, Kersten *et*

al. 2009). However, station S5 also provided a more even distribution of ANU values over a larger part of the façade surface (cf. Fig. 13E).

In general, due to limited θ variation (less than $\pm 20^\circ$), ANU values do not vary significantly at the shorter sides (Ⓑ and Ⓓ) of the building. Note that the uniform fixed-value scale is applied to Figs. 13 and 14 in order to make the sub-plots comparable to each other.

As expected based on the result of Eq. 3.7, the largest ANU values for the bridge deck surveying cases were from station B1 located directly under the bridge deck (Fig. 14A).

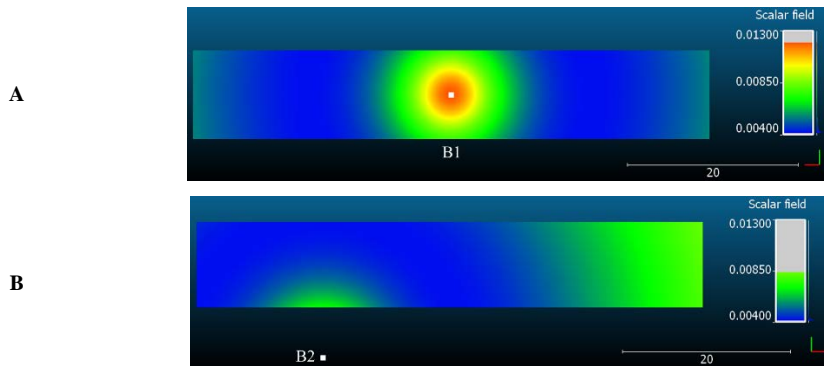


Figure 14. Top view of the spatial distribution of ANU estimates along the bridge deck surface for scanning stations B1 and B2. The images are rotated 90° . The locations of the stations are denoted by white dots. The grey colour in the fixed-value scale denotes the non-occurring ANU values at particular surveying cases. Units in metres.

In conclusion, the calculated ANU values are relatively large (Figs. 13 and 14). This is most likely due to apparently pessimistic metrological values provided by the manufacturers of the TLS instruments.

5.3. Results of geometric modelling of the noise-contaminated data

The one-signed (positive) ANU values determined by Eq. 3.6 do not fully represent the actual measuring uncertainties, which are in general random, thus having both negative and positive values. Therefore the simulated data are further contaminated with random along-normal noise of a zero expectation (yielding thus a near-zero mean value). For determining the influence of ANU for geometric modelling of surfaces, the noise-contaminated data are to geometrically modelled.

The modelling results indicated good surface fitting. This was most likely due to the fact that noise in the survey data did not include any significant systematic error and had a normal distribution with a near-zero mean value. The simulated along-normal noise did not produce significant effects on the geometric modelling of surfaces. The modelled surfaces were very similar to the

true dimensions of the surfaces (cf. Section 5.1). For detailed explanations of introducing noise to the simulated data and geometric modelling results see **Paper I**.

5.4. Optimization of scanning locations

The optimality criterion for identifying the optimal scanning locations was defined according to the magnitude and the distribution of the calculated ANU values (cf. Figs. 13 and 14).

Based on the analysis of different simulated scenarios (and the given metrological parameters), optimal scanning locations were determined for (i) the vertical surfaces of a building façade and (ii) the horizontal surfaces of a bridge deck.

In the first case, they were found to be the locations closest (less than 10 m) to the corners of the building (stations S1, S2 and S3). Approximately 85% of the ANU values for the longer sides ① and ③ obtained from these stations were less than 1 cm. This ratio was only 67% and 50% for stations S4 and S5, respectively (cf. Fig. 13). For the short sides of the building, the ANU values for stations S1, S2 and S3 were all less than 0.7 cm. In the second case, the optimal location was found to be at the side of the bridge deck (station B2), since all the ANU values obtained for data from this station were less than 1 cm (cf. Fig. 14). Thus, in the case of bridge surveys, it is recommended that the TLS station should be placed to the side of the bridge. This suggestion, however, will only help to minimize possible ANU values. At side locations, some structural elements of a bridge may remain hidden from the scanner's field of view. Therefore, in some cases, the expected ANU values may not compensate the data void.

It is shown that maximum ANU values are expected when the surveying is carried out in a direction perpendicular to the surface. As the surveying distance also has a significant impact on the magnitude of the ANU, the optimal scanning distance at which ANU can be reduced is between 10 and 25 metres (cf. results in Fig. 7, which demonstrates that the smallest uncertainties occur within this interval, and that beyond 25 m the uncertainties start to increase). For detailed explanations of the optimal scanning locations see **Paper I**.

6. TESTED TLS APPLICATIONS

A TLS instrument is capable of recording a countless number of survey points within a relatively short period of time. A large number of survey points enable acquiring information of the spatial distribution of surface deformations, rather than describing single point movements obtained by classical pointwise measuring techniques (e.g. total station surveys). A TLS technology, in particular a TOF technology, was applied for deformation monitoring purposes to monitor bridge deformations occurring during a static load test (**Paper II**) and in investigating road surface deformations due to the effects of frost heave (**Paper III**). In addition, the methodology for calculating ANU values (see Chapter 3) as proposed in **Paper I** was tested and proved by the results achieved in the aforementioned case studies (**Papers II** and **III**).

6.1. TLS for monitoring deformations of engineering structures

The application of the TLS technology was investigated in the case study of monitoring deformations occurring during a static bridge load testing (**Paper II**). The structure of the bridge was of beam type with two concrete cantilevers. The TLS measurements were carried out alongside of the bridge (Fig. 15, cf. also Fig. 12B). According to the literature, e.g. Soudarissanane *et al.* (2009 and 2011), TLS surveys are expected to be noisy due to large values of the angle of incidence (ranging approx. from 80° to 87°) and relatively poor reflectivity conditions (e.g. Kersten *et al.* 2005) of the lower sides of the concrete cantilever beams (approx. reflectivity of concrete is 24%, Wehr and Lohr 1999). Since TLS survey results can suffer some accuracy limitations reported by e.g. Holst and Kuhlmann (2016), alternative geodetic survey methods (such as precise levelling) were applied as well. The TLS monitoring results were also compared with results obtained from using the 3D finite element simulation model.

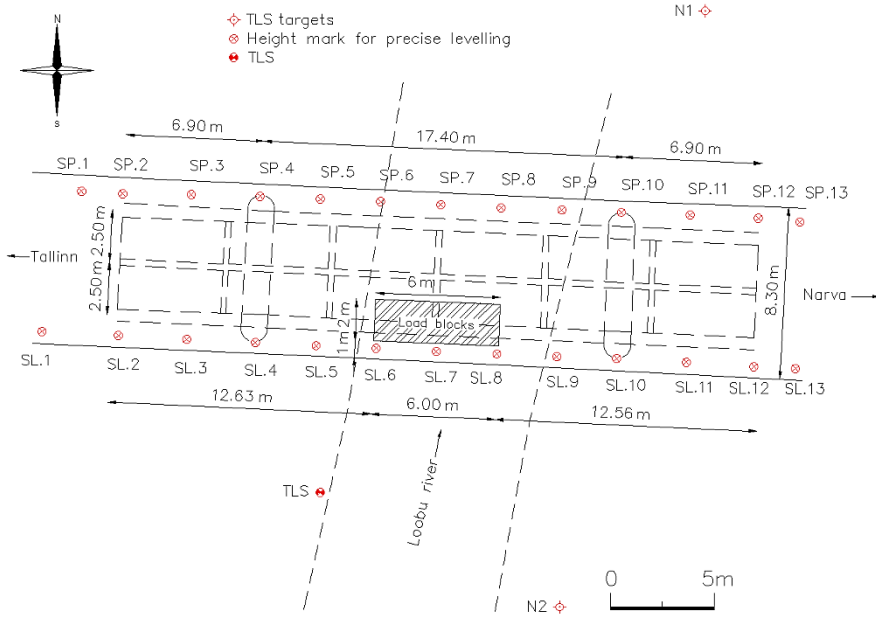


Figure 15. Scheme of the bridge structure (columns, cantilever beams illustrated by dashed lines) with locations of TLS stations, TLS targets, load blocks and levelling height marks.

The methodology for calculating ANU values (as proposed in **Paper I**) was used to assess the theoretical TLS uncertainty in the monitoring of a bridge load test. For this, the observation equation

$$z = \rho \cos \kappa, \quad (6.1)$$

was used to determine the height of a survey point on the lower side of a cantilever beam. Note that in the observation equation κ is the measured zenith angle (cf. Eq. 2.4). The estimated ANU values for the heights of the survey points on the beams were obtained by (cf. Eq. 3.5).

$$u_{\hat{z}} = \left[\cos^2 \kappa u_{dist}^2 + \rho^2 \sin^2 \kappa u_{v.angle}^2 \right]^{1/2}, \quad (6.2)$$

where $u_{\hat{z}}$ is the estimated ANU value for the heights (z -component) of the survey points on a beam, ρ is the measured distance, u_{dist} is the scanner's standard distance measuring uncertainty, $u_{v.angle}$ is the scanner's standard vertical angle measuring uncertainty. For detailed explanations of the uncertainty estimations see **Paper II**.

The application of the TLS technology was also investigated in the case study of detecting road surface deformations (**Paper III**) occurring due to frost heave (the occurrence of which is common for seasonal frost regions) of roads (Fig. 16). To study the effects of frost heave of roads, TLS surveys were expected to be affected by environmental conditions, the near-perpendicular angle of incidence values and the relatively poor reflectivity of the asphalt concrete surface of the road (approx. reflectivity of dry asphalt is 17%, Wehr and Lohr 1999). The scanning works were carried out at near-zero air temperatures (+1 °C and +4 °C) and contrasting air humidity (98% and 3%). According to e.g. Lerma García *et al.* (2008) and Hejbudzka *et al.* (2010), such combinations of atmospheric conditions can have a significant influence on the survey data quality.

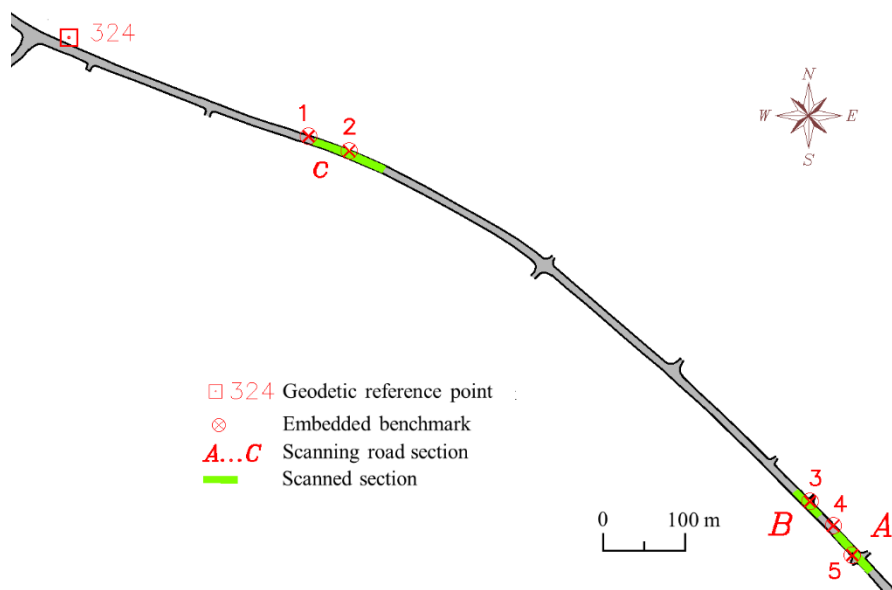


Figure 16. Locations of the scanned areas (depicted in green) and the levelling benchmarks. Section A was scanned from benchmark 5, section B from benchmark 3 and section C from benchmark 2.

The methodology for calculating ANU values (as proposed in **Paper I**) was used to assess the theoretical TLS uncertainty in detecting road surface deformations. For the theoretical uncertainty assessment, an observation equation (Eq. 6.3) for the calculation of the absolute height (above sea level) of the survey point was used. Note that the observation equation takes into account the geometrically levelled height of the benchmark (z_b) and the tape measured height of the instrument above the benchmark (i_{TLS}). Also in this case, κ is the measured zenith angle. The estimated ANU values for the heights of the survey points were obtained by (cf. Eq. 3.5)

$$H = z_b + i_{TLS} + \rho \cos \kappa, \quad (6.3)$$

and

$$u_{\hat{H}} = \left[u_{\hat{z}_b}^2 + u_{\hat{i}_{TLS}}^2 + \cos^2 \kappa u_{dist}^2 + \rho^2 \sin^2 \kappa u_{v.angle}^2 \right]^{\frac{1}{2}}, \quad (6.4)$$

where H is the absolute height of the survey point; $u_{\hat{H}}$ is the ANU of the height of a survey point, $u_{\hat{z}_b}$ is the estimated uncertainty of the benchmark height determined by geometric levelling and $u_{\hat{i}_{TLS}}$ is the estimated uncertainty of the tape measured height of the instrument. The estimated values for the worst case scenario for $u_{\hat{z}_b}$ and $u_{\hat{i}_{TLS}}$ were 3 and 2 mm, respectively. For detailed explanations of the uncertainty estimations see **Paper III**.

6.1.1. Results of deformation monitoring

For either case study, no significant unfavourable behaviour was detected in the obtained point clouds, e.g. due to surveying under a large angle of incidence values. According to results of studies by Kersten *et al.* (2009) and Hiremagalur *et al.* (2009), TLS of TOF type are not very sensitive to scanning under a large angle of incidence values. The latter is also supported by the results reported in **Paper I**.

The result of the theoretical uncertainty assessment for the bridge deformation monitoring is reported in **Paper II**. The estimated ANU (Eq. 6.2) for sequential TLS data sets for the lower surface of the cantilever beam reached 2.8 mm ($\pm 2.0\sqrt{2}$) at 95% confidence level (two sigma). The differences of the obtained beam deflection magnitudes (TLS vs. precise levelling) in the central parts of both cantilever beams (Fig. 15) were of the ± 2 mm magnitude.

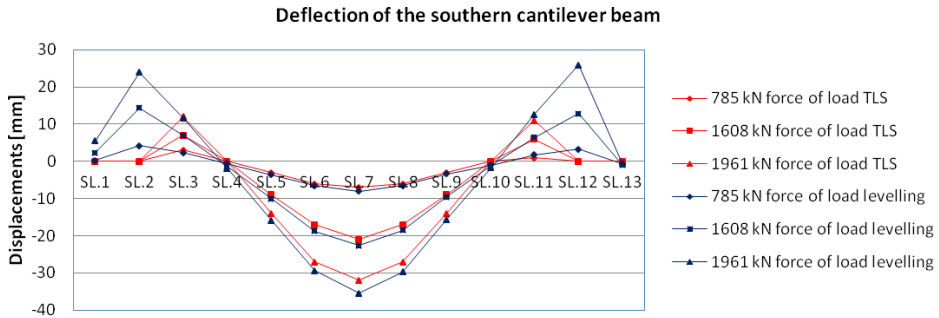


Figure 17. Comparison of TLS and levelling results of the southern beam. At the centre of the beam (SL.7) the deflection difference between TLS and levelling is under 785 kN +0.108 cm; under 1608 kN +0.169 cm; under 1961 kN +0.342 cm.

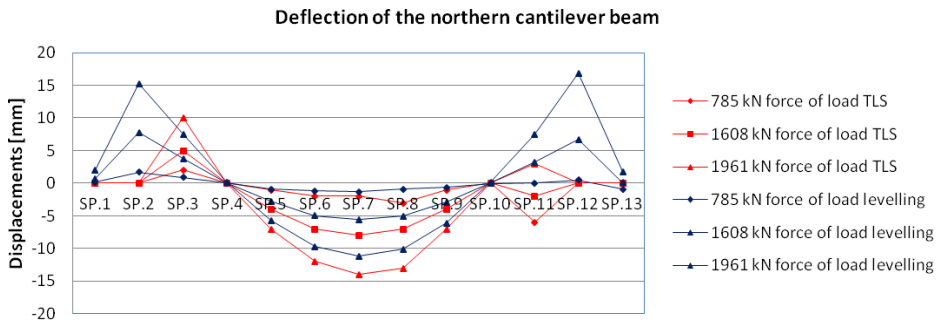


Figure 18. Comparison of TLS and levelling results of the northern beam. At the centre of the beam (SP.7) the deflection difference between TLS and levelling is under 785 kN -0.177 cm; under 1608 kN -0.24 cm; under 1961 kN -0.289 cm.

Precise levelling shows slightly larger deflection values for the southern beam (cf. Fig. 17). In the case of the northern beam, precise levelling results show slightly smaller deflection values (cf. Fig. 18). They remain just within millimetres (see detailed values in Table 1).

Table 1. Comparison of deformation results

Load [kN]	Differences at the centre of the beams [cm] (TLS – Precise levelling)	
	Southern beam	Northern beam
758	+0.108	-0.177
1608	+0.169	-0.240
1961	+0.342	-0.289

These differences between TLS and precise levelling results (cf. Figs. 17 and 18) occurred for the following reasons: (i) the large angle of incidence values

(close to 90°) associated with the TLS measurements, (ii) the eccentric placement of the levelling marks on the bridge deck with respect to the TLS monitored bridge beams, (iii) different deformation behaviour of the bridge deck and the bridge beams, and (iv) the asymmetric placement of the load with respect to the bridge deck and the two beams. These reasons are also summarized and confirmed by Löhmus *et al.* (2017).

The predicted maximum deflection of the beams using the 3D finite element simulation model was 50.3 mm, the obtained maximum with TLS was 30.2 mm, which is 1.6 times less than predicted (see **Paper II**). Since the 3D finite element simulation model relied on the idealized geometry of the structure, not based on its existing geometry, such differences can be considered reasonable (Riveiro *et al.* 2011). In general, geodetic surveying results can be considered an indispensable source of information to test and adjust theoretical assessments made by bridge engineers. For more detailed information about the obtained case study results see **Paper II**.

In the case study of detecting the magnitude and spatial distribution of frost heave (**Paper III**), the theoretical ANU assessment for two sequential TLS data sets in the case for the road surface surveying (Eq. 6.4) was 11.3 mm ($\pm 8.0\sqrt{2}$) at 95% confidence level (two sigma). Such results were obtained by averaging the results of four ANU values calculated for the survey points at distances 5, 10, 25 and 50 metres. The verification of TLS surveyed heights was carried out using the benchmark heights obtained by geometric levelling. The verification results indicated ± 2.9 mm for TLS surveying accuracy. The verified accuracy differed from the theoretically estimated TLS uncertainty by 5.1 mm (2.9 mm vs. 8.0 mm). This indicates that the actual TLS surveying accuracy is better than the theoretical one. The maximum estimated magnitude of frost heave was determined to be 90.0 mm in a small part of road section A (Fig. 19A). The main parts (up to 50%) of the selected road sections indicated a rise from 22 mm up to 63 mm, the rest of the areas indicated smaller or no rise at all. According to the guide for the design of elastic pavements from the Estonian Road Administration (2001), the maximum allowed pavement vertical rise for asphalt concrete pavements is 40 mm. Thus the obtained deformations due to frost heave were generally a little over the normative threshold. To conclude, the TLS technology benefits in determining accurate magnitudes and spatial distribution of frost heave of roads, which may also be an evidence of relatively poor road design quality.

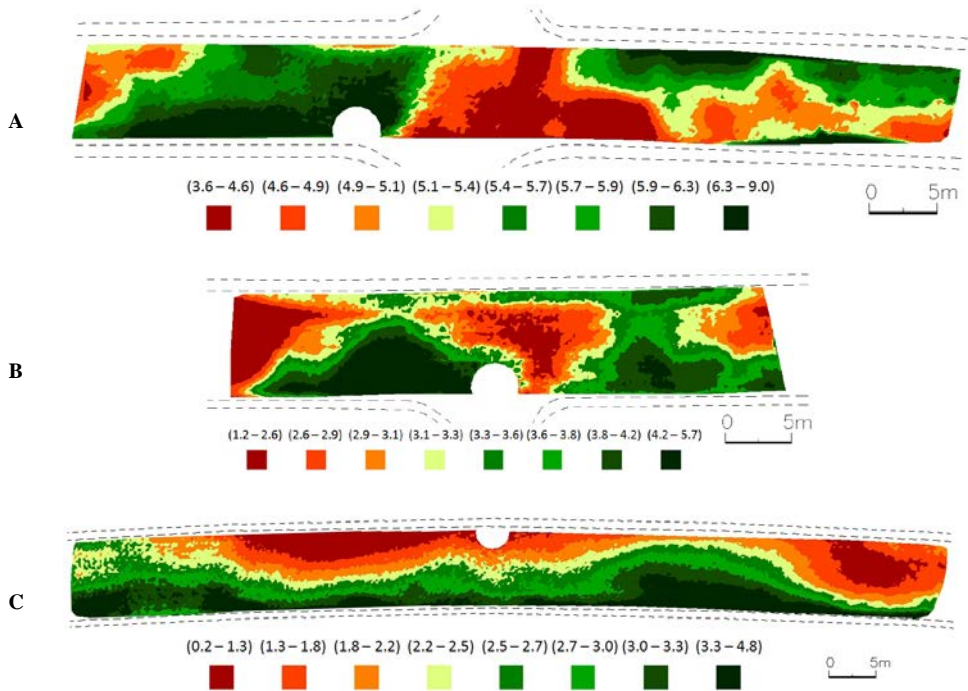


Figure 19. Comparison of road surface models November 2012 vs. April 2013 (cf. Fig. 16). (A) Road section A; length of the section 63 m. (B) Road section B; length of the section 42 m. (C) Road section C; length of the section 94 m. The non-coloured half-circle indicates the location of the scanner, dashed lines denote roughly the edges of tarmac and the widths of road shoulders.

6.2. TLS for road surveying purposes

Since TLS implements contactless surveying, the technology has advantages for road surveying purposes over conventional geodetic surveying methods. These advantages include the reduced need for traffic lane closures and the safety of surveyors. For example, Yu and Lo (2005) and Lee (2009) reported that there are three major items affecting the social costs of road construction: traffic interruptions, road closures and accidents. The study by Yu and Lo (2005) concluded that the monetary value of the social cost itself can be more than five times higher than the road construction cost. The surveyor safety of using the TLS technology for road surveys has been addressed in the literature by e.g. Chow (2007), Hiremagalur *et al.* (2009) and El-Ashmawy (2016). In general, TLS can reduce road construction project costs because of not closing down lanes for traffic for surveys. Due to contactless surveying, TLS also increases the safety of the surveyor.

6.2.1. Comparison of TLS and conventional surveying techniques in road surveys

A comparison of two road surveying techniques, TLS and a traditional total station surveying, was carried out and the results are reported in **Paper V**. The study also investigated the benefits of TLS for road surveying purposes. The asphalt concrete pavement surface of the road section selected (37 metre long strip) was described by apparent rutting and shoving (Fig. 20). The road section was planned to be renovated soon after the surveys for the study were carried out. The renovations planned included only replacing the top layer of the asphalt concrete surface. Thus the study also aimed to identify differences in the material quantities (material that should be milled off and material required for filling) obtained by using TLS and total station survey data.



Figure 20. The road section selected is characterized by shoving and rutting.

The optimal scanning distances of using TLS for road surveys are identified based on **Papers III** and **V** to be approximately 30 to 70 metres for road surveys using a TOF type scanner.

6.2.2. Results of the comparisons and the optimal scanning distance for road surveys

The results of the study investigating the application of TLS for road surveys (**Paper V**) confirmed expectedly the surveyor safety feature of TLS. Therefore the technology is well suitable for road surveys under non-stop traffic. According to the traffic count in 2007 by Teede Tehnokeskus AS (2007), the average daily traffic density is more than 8400 vehicles on this particular road section. Also, a benefit of using the TLS technology for road surface surveys is clearly the high level of detail in the obtained data. Detailed information of the surface of the road (Fig. 21) makes it possible to optimize the quantities of material needed for reconstruction.

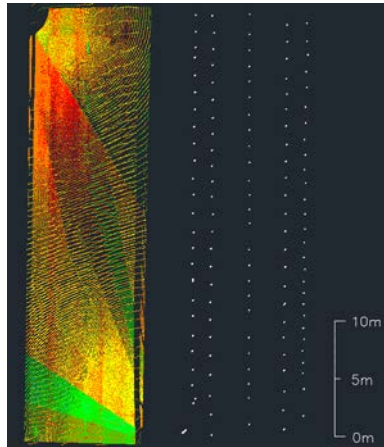


Figure 21. TLS measured points with intensity values (left) and total station survey points (right).

The case study in **Paper V** also indicated that TLS surveys are dependent on the weather conditions, especially precipitation. The TLS surveys were conducted on a day with some rainfall, and some noise in the obtained point clouds was caused by the reflection of the laser beams from raindrops.

Based on the analysis of the data and the results obtained during the case study reported in **Papers III** and **V**, the optimal scanning distance from the scanner is approximately 30 to 70 metres for road surveys using a TOF type scanner. However, the exact value for the optimal scanning distance for road surveys is rather challenging to suggest. This is mainly due to the fact that a TLS survey is dependent on the scanner type and surveying conditions, e.g. pavement type, the longitudinal and transverse profile of the road, atmospheric conditions, moisture etc. In addition, the scanning distance is influenced by the larger angle of incidence values in road surveys and relatively poor surface reflectivity (recall that the approx. reflectivity of dry asphalt is 17%, Wehr and Lohr 1999). As the angle of incidence increases the laser signal footprint on the surface elongates (e.g. Deems and Painter 2006). Because of this, the power of the signal attenuates up to an energy level that the backscatter signal may not be recorded at all. The problem is even more critical when the asphalt concrete surface of the road is wet (cf. Section 6.1. and Fig. 22). In such a case a lot of points attenuate completely due to the absorption of electromagnetic radiation by water. In general, the survey points at longer distances become more sparsely distributed on the surface. The ANU values in the vertical direction of those points increase with the increasing distance (e.g. Eling 2009, Barbarella *et al.* 2017, **Paper I**).



Figure 22. The point cloud of the road section C used in **Paper III** (A) and photo illustrating scanning conditions in early spring (B). The scanning conditions were very good, the surface of the road was mainly dry (air temperature +4 °C and humidity 3%). The expected surface reflectivity of the asphalt was improved partly due to some influence of the dried chloride used for anti-icing on roads in frost seasons.

6.3. TLS for building surveying purposes

For the AEC/FM industry parametric modelling, the basic concept of BIM has become of great importance for efficient resource management. For new buildings, the major benefits of BIM according to Volk *et al.* (2014) are the consistency and visualization, cost estimations, clash detection, implementation of lean construction and improved stakeholder collaboration. For existing buildings the benefits lie for example in the documentation of objects of cultural heritage (Murphy *et al.* 2013, Wilson *et al.* 2013), as-built surveys and quality assessment (Boukamp and Akinci 2007), maintenance (Becerik-Gerber *et al.* 2012), retrofit planning (Larsen *et al.* 2011) etc. The data for creating parametric models of existing buildings are usually obtained using a geodetic survey, e.g. total station survey or TLS survey. Other survey methods applying simple techniques such as tape measuring or laser distance measuring are also used. Note that according to COBIM (2012), building models based on measurements using laser distance measuring instruments are not considered geometrically reliable. In building surveys, in general, a TLS data cloud is geometrically modelled to determine e.g. the object's conformance with design parameters etc. The ANU plays a significant role in geometric modelling results (**Paper I**). In addition, Tang *et al.* (2011) pointed out that one of the main quality assurances for TLS surveying results can be done by assessing ANU values. The main challenge, however, of creating a BIM model using TLS data is in linking data from different surveys together, e.g. data from separate rooms or floors (Tang *et al.* 2011, Bosché 2012).

6.3.1. TLS for BIM purposes

The applicability of the TLS technology for building surveys was investigated in the case study presented in **Paper IV**. The general aim of this study was to generate a BIM model of an existing building with the level of detail 300 (Weygant 2011) allowing functionalities regarding design, construction and maintenance processes. The survey data were collected using a TLS survey and a total station survey. Also here one of the main challenges is linking different surveys together (e.g. different building floor levels etc.) to provide data in a common reference frame (Tang *et al.* 2011, Bosché 2012). For this purpose, a classical geodetic control network was established around and inside the building (Fig. 23).

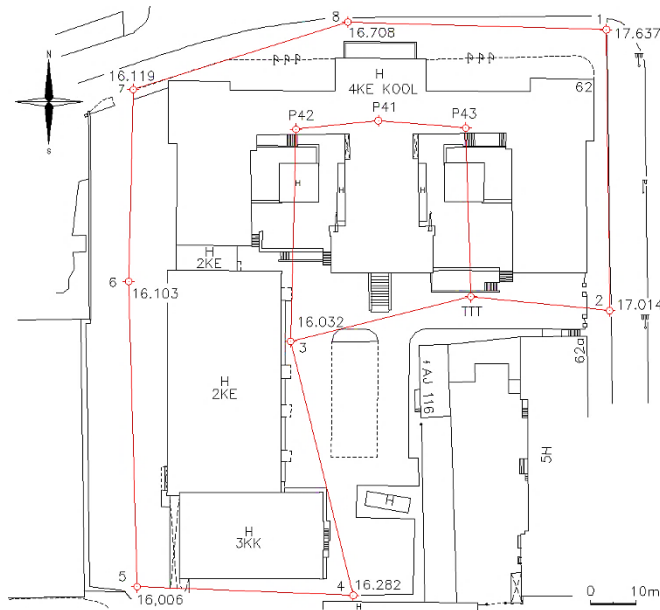


Figure 23. The established survey traverse. Points P41, P42 and P43 represent control points on the fourth floor of the building.

Using a control network for building survey purposes is also suggested by GSA (2009). The control network allowed all TLS surveys, including total station surveys, to be directly carried out in a uniform reference frame. Using the control network assured the alignment of the survey data between different TLS stations. In addition, a control network allows verifying the obtained data quality (**Paper III**).

6.3.2. Results of building surveying

The results of the building survey study (**Paper IV**) indicated that using highly detailed TLS data for the generated BIM model of an existing building makes it

possible to detect and determine the magnitudes of e.g. façade damage areas that are in need of refurbishing. Also, TLS data make it possible to detect spatial conflicts between the designed and the existing objects (i.e. clash detection). For example, the shape and the size of the pyramid-shaped skylight in the courtyard of the building under investigation differed largely between reality and the fire zone drawings (Fig. 24). Such an example illustrates possible shortcomings in the building management documents.

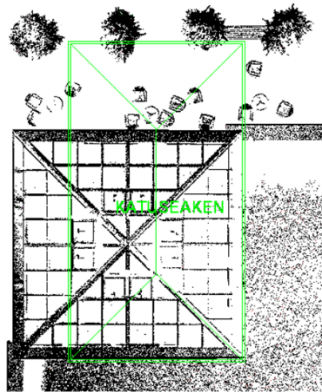


Figure 24. The pyramid-shaped skylight in the courtyard of the studied building (black and white) and the skylight in the fire zone drawings (green).

The results of this study indicated also some problematic areas concerning the usage of TLS data for BIM purposes. Problems arose when adding supplementary point cloud data to the BIM model that was in the processing stage. Merging of additional data is generally done manually. Another problem is the lack of the best fitting functions for surfaces. The modellers draw the surface into the point cloud using their best intuition. In general, the results of the case study brought out that the usage of TLS data for BIM purposes is limited due to low automation possibilities for data processing. Nevertheless, TLS data proved to be indispensable for modelling older and historic buildings with e.g. non-vertical walls.

In addition, as the scanning of the façade of the four storey building (see building details in **Paper IV**) was conducted at the ground level, TLS surveys were expected to be also challenged by the large values of the angle of incidence and relatively poor reflectivity conditions. However, no significant unfavourable behaviour was detected in the obtained point clouds caused by surveying under the large angle of incidence values. This may also be due to the fact that the major part of the façade surface is covered by an uneven limestone surface and thus the laser signal at the near perpendicular angle of incidence could be reflected back from the coarse-grained surface (Fig. 25).

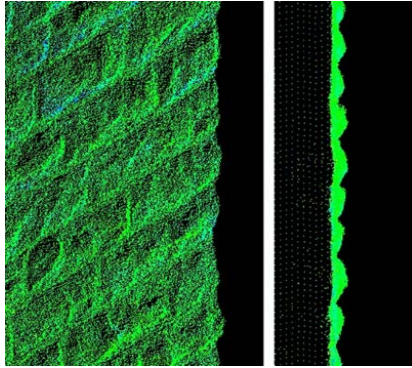


Figure 25. An example of a point cloud of the building's limestone façade (**Paper IV**); front view (left) and side view (right). The limestone joints are at intervals of approx. 15 cm.

7. DISCUSSION

The objective of the PhD studies was to investigate certain TLS applications for engineering structure surveys. For this purpose, a novel method that enables assessment of along-normal uncertainties was developed. The developed ANU calculation method supports a wide range of users of the TLS technology with a tool for quality assessment of TLS surveys. The method also contributes to a variety of methods of assessment of measurement uncertainties occurring during the surveying of engineering structures. The significance of the proposed ANU calculation method is that the method focuses in particular on assessing ANU. The ANU have a critical influence on geometric modelling and they can be used for quality assessment of TLS data (e.g. Tang *et al.* 2011).

The developed ANU calculation method makes it possible to carry out uncertainty assessments both before and after the actual surveys. Having a possibility of assessing the obtainable uncertainty of the surveys helps to better plan the work ahead. For example, the knowledge of the expected accuracy allows assessing, in general, whether the existing scanning device can ensure the accuracy of the results needed for meeting the accuracy requirements of the project. The knowledge of the obtainable surveying results is essential especially in construction engineering where the accuracy requirements are rigorous.

The thesis also addressed the main limitations (large angle of incidence, atmospheric conditions and validating TLS results) of using TLS for the surveying of engineering structures. As claimed in the literature (e.g. Lichti 2007, Soudarissanane *et al.* 2009, 2011), the most crucial limitation is surveying under a large angle of incidence. Arguably, exceeding the 60° threshold is expected to yield a sharp increase in the overall measurement noise. Based on the results of the present study, however, the influence of a large angle of incidence appeared to be rather insignificant for a TOF type instrument. Such results are similar to the findings reported by Kersten *et al.* (2009). Nonetheless, the possible effects of a large angle of incidence should not be neglected in the process of planning TLS surveys and should be addressed with some caution (cf. aforementioned literature sources). In general, the effects of a large angle of incidence on TLS surveys need to be investigated more thoroughly. This should be done for example by testing different TLS distance measuring principles, similarly to Kersten *et al.* (2009).

7.1. Suggestions for future research

The developed method for calculating ANU values for the general TLS surveying cases as described in Chapter 3 of this thesis allows conducting both *a priori* and *a posteriori* quality assessment of the scanning results. Thus the developed method can help to better plan the TLS surveys ahead.

Considering that up-to-date total stations enable laser scanning, in future studies, it would be worth investigating the ANU values for total stations as well.

The proposed ANU calculation method can be developed and extended further by incorporating for example atmospheric factors (e.g. air humidity and temperature). In addition, a computer program can be developed that calculates the estimated ANU values. The program should include a simulation of a standard scanning scenario of an engineering structure (e.g. a vertical surface representing a building façade). The location of the scanner with respect to the structure should be freely changeable. This can be used to test different scanning locations to obtain ANU values. Such developments would allow surveyors to better plan different scanning activities. Also, it would help to better optimize scanning work and improve the quality of TLS survey data in terms of ANU values. In addition, investigations should be conducted to study how to incorporate the estimated ANU values in the post-processing of TLS data to improve the obtained scanning results.

In engineering surveying the surveying environments are sometimes very challenging having dusty, cold, hot, wet etc. conditions. The magnitude of the surveying projects can vary from very small to very large. Also, surveys can involve to some accuracy restrictions (e.g. GSA 2009, Caltrans 2011, Fraunhofer IFF 2015). As different TLS working principles (generally TOF and PS) are available, it is worth investigating the optimal TLS type for a specific field of work, e.g. as-built surveys, road surveys etc. Different TLS principles should be tested in homogeneous conditions. The conditions should vary for example by different surface properties (e.g. reflectance and material) and environmental conditions (e.g. air humidity and temperature). As a result, such investigation should also reveal the cost benefits of different TLS principles in terms of for example the estimated working time, the optimal scanning distances (e.g. road surveys) etc.

For traditional geodetic instruments (e.g. levelling instruments and total stations) there are regulations describing the accuracy requirements for the instruments used in specific geodetic surveying projects (e.g. ISO 8322-1:1989 Building construction - Measuring instruments). However, no specific regulations exist for the TLS technology. In future studies, suggestions should be made for the AEC/FM industry to help to determine criteria for the TLS technology. The criteria would help to distinguish between instruments that are acceptable for rigorous geodetic surveys and instruments that are suitable only for mapping and documenting purposes where the accuracy requirements are not very high.

Since the TLS technology has been used quite widely in the AEC/FM industry, future studies should focus more on investigating the possibilities of improving data processing and data management. The focus should be more on how to derive quickly, for example, as-built and quality control results using TLS data. In particular, identification of the significance of the obtained results following, for example, project-specific and standardized construction specifications (e.g. ACI 117-10 2010) need to be addressed.

8. CONCLUSIONS

8.1. Contribution to estimating TLS along-normal uncertainties

The PhD studies were aimed at contributing to the methods of the assessment of measurement uncertainties occurring during the surveying of engineering structures. The developed method makes use of the concept of combined standard uncertainty (CSU), which originates in the classical theory of geodetic measurement errors (e.g. Bjerhammar 1973) and has been adopted in contemporary guidelines for the measurement industry (JCGM 100:2008). Although, at the moment, no standardized testing procedures of TLS instruments exist, the results reported in Chapter 4 indicate that the derived method to calculate along-normal uncertainties (ANU) using a classical error propagation method is very promising. This is due to the fact so far manufacturers of scanners provide only the general metrological specifications of an instrument. The results in Chapter 4 suggest that these specifications are rather too pessimistic. This is confirmed by the results obtained in empirical deformation monitoring case studies (**Papers II and III**), where the theoretically estimated uncertainties obtained were larger than the actual uncertainty. However, using the available TLS characteristics, the expected magnitudes of ANU values can be assessed *a priori* and *a posteriori*. Such a solution is very beneficial especially for surveying projects where the magnitude of deformations is small and repeating the measurements is not possible.

Specifications of TLS accuracy should be obtained by using uniform testing methods (according to ISO.org, standards for testing TLS are being developed). This is essential for example because already a significant number of studies conducted have relied on specifications provided by the manufacturers of scanners (e.g. Boukamp and Akinci 2007, Golparvar-Fard *et al.* 2011, Riveiro *et al.* 2011, Bosché and Guenet 2014 etc.). The available specifications for TLS are generally not evaluated independently. According to GSA (2009) and Fraunhofer IFF (2015), the surveying instruments (i.e. TLS) used in the projects are required to be calibrated before the start of the project and should have been calibrated within the 12 months prior to the project start date. Today a lot of effort is required for developing calibration methods for each specific scanning project (e.g. Holst *et al.* 2014, Wang *et al.* 2015). This is eventually very time-consuming, and is also a general problem in the AEC/FM industry concerning the usage of TLS.

The ANU results (Chapters 4, 5 and 6) suggest that the uncertainties provided by instrument manufacturers should be looked over critically. It is expected that with the establishment of standardized calibration methods for TLS more accurate estimations of ANU can be made.

8.2. Engineering structure surveys using the TLS technology

Today the TLS technology is widely used in the AEC/FM industry. Many previous studies, as well as the present study, have indicated that the TLS technology benefits from a high level of detail of survey data and fast data acquisition rates (exceeding 1 MHz). A problematic area of using TLS for engineering structure surveys is the assurance of the quality of the survey data (e.g. Holst and Kuhlmann 2016, Soudarissanane 2016). In addition, TLS accuracy can be influenced by systematic errors (Holst and Kuhlmann 2014), a large angle of incidence (e.g. Soudarissanane *et al.* 2009, 2011) and atmospheric conditions (Lerma García *et al.* 2008, Hejbudzka *et al.* 2010). The aforementioned problematic areas are investigated in the empirical studies (**Papers II to V**).

The following conclusions can be drawn on the basis of the empirical case studies carried out during the doctoral studies:

- (i) The results of the empirical case studies presented in Chapter 6 (**Papers II, III and IV**) indicated no significant effects of a large angle of incidence in the data. For both case studies, a TOF scanner was used. The influence of a large angle of incidence values on the quality of point cloud may be a critical factor for PS scanners, which use the digital signal processing of continuous wave lasers (Hiremagalur *et al.* 2009, Kersten *et al.* 2009).
- (ii) As reported in the literature (e.g. Lerma García *et al.* 2008), atmospheric conditions can have an influence on TLS survey data. The case studies presented in Section 6.2 (**Papers V and III**) indicated that atmospheric conditions affecting TLS surveys are mainly related to precipitation and the object's surface reflectivity deterioration due to moisture. Precipitation can generate noise due to laser signals reflecting back from raindrops (**Paper V**). Common construction materials like concrete and asphalt have generally a low level of reflectance. If these materials were wet, the reflectance would be even more degraded. The results in Section 6.2.2 indicated that wet surfaces reduce the number of backscattered points.
- (iii) Due to the fact that the specific construction of each laser scanner is hidden the actual measuring principles are not known (Holst and Kuhlmann 2014). Therefore it is difficult to rely solely on the scanning data for providing reliable results for e.g. deformation monitoring. Supplementary geodetic measurements are still suggested to validate TLS surveys. These are also suggested for the cases where it is necessary to validate results, e.g. in building surveys (**Paper IV**) and in road surveys (**Paper III**) with TLS data. This is also supported by the guidelines from the AEC/FM industry, e.g. GSA (2009), Caltrans (2011), BIM Task Group (2013) and Fraunhofer IFF (2015).

In conclusion, based on the empirical studies and the gained experiences obtained throughout the conducted work, it can be said that the TLS technology is beneficial for surveying engineering structures. Naturally, this agrees with the general opinions found in the literature. However, for the sake of certainty, for the most demanding engineering applications TLS results still need to be verified using other geodetic surveying technologies.

LIST OF REFERENCES

- Abbas, M. A., Setan, H., Majid, Z., Lichti, D. D. and Chong, A. K. (2013). A self-calibration of the Leica ScanStation C10 scanner. *Business Engineering and Industrial Applications Colloquium* (pp. 262–266). Langkawi, Malaysia: IEEE.
- ACI 117-10 (American Concrete Institute). (2010). Tolerances for Concrete Construction Anparkd Materials. Detroit: ACI Committee.
- Akgul, M., Yurtseven, H., Akburak, S., Demir, M., Cigizoglu, H. K., Ozturk, T., Eksi, M. and Akay, A. O. (2017). Short term monitoring of forest road pavement degradation using terrestrial laser scanning. *Measurement*, 103, 283–293.
- Alkhatib, H., Neumann, I. and Kutterer, H. (2009). Evaluating uncertainties of laser scanner measurements by using a joint Monte Carlo and Fuzzy approach. *XIX IMEKO World Congress Fundamental and Applied Metrology* (pp. 2394–2399). Lissabon, Portugal: IMEKO.
- Armesto-González, J., Riveiro-Rodríguez, B., González-Aguilera, D. and Rivas-Brea, M. T. (2010). Terrestrial laser scanning intensity data applied to damage detection for historical buildings. *Journal of Archaeological Science*, 37, 3037–3047.
- Barbarella, M., De Blasiis, M. R. and Fiani, M. (2017, online). Terrestrial laser scanner for the analysis of airport pavement geometry. *International Journal of Pavement Engineering*, 1–15. DOI: 10.1080/10298436.2017.1309194
- Bayoud, F. A. (2006). Leica's pinpoint EDM technology with modified signal processing and novel optomechanical features. *XXIII FIG Congress Shaping the change* (pp. 1–16). Munich, Germany: FIG.
- Becerik-Gerber, B., Jazizadeh, F., Li, N. and Calis, G. (2012). Application areas and data requirements for BIM-enabled facilities management. *Journal of Construction Engineering and Management*, 138(3), 431–442.
- BIM Task Group. (2013). Client Guide to 3D Scanning and Data Capture. London: The Building Information Modelling (BIM) Task Group.
- Bjerhammar, A. (1973). *Theory of Errors and Generalized Matrix Inverses*. Amsterdam: Elsevier Science Ltd.
- Bosché, F. (2012). Plane-based registration of construction laser scans with 3D/4D building models. *Advanced Engineering Informatics*, 26(1), 90–102.
- Bosché, F. and Guenet, E. (2014). Automating surface flatness control using terrestrial laser scanning and building information models. *Automation in Construction*, 44, 212–226.
- Bosché, F., Haas, C. T. and Akinci, B. (2009). Automated recognition of 3D CAD objects in site laser scans for project 3D status visualization and performance control. *Journal of Computing in Civil Engineering*, 23(6), 311–318.

- Boukamp, F. and Akinci, B. (2007). Automated processing of construction specifications to support inspection and quality control. *Automation in Construction*, 17(1), 90–106.
- Caltrans (California Department of Transportation). (2011). Terrestrial laser scanning specifications. California: Caltrans.
- Chen, X., Zhang, G., Hua, X. and Xuan, W. (2016). An average error-ellipsoid model for evaluating TLS point-cloud accuracy. *The Photogrammetric Record*, 31, 71–87.
- Chilani, C. D. and Wolf, P. R. (2006). *Adjustment Computations: Spatial Data Analysis*. Hoboken: Wiley.
- Chow, J., Lichti, D. and Teskey, W. (2012). Accuracy assessment of the FARO Focus3D and Leica HDS6100 panoramic type terrestrial laser scanners through point-based and plane-based user self-calibration. *FIG Working Week 2012* (pp. 1–15). Rome, Italy: FIG.
- Chow, K. L. (2007). Engineering survey applications of terrestrial laser scanner in highways department of the government of Hong Kong special administration region. *FIG Working Week 2007 Strategic Integration of Surveying Services* (pp. 1–12). Hong Kong, China: FIG.
- COBIM. (2012). Common BIM Requirements, Series 2: Modelling of the Starting Situation. Senate Properties. Helsinki: BuildingSMART Finland.
- Cuartero, A., Armesto, J., Rodríguez, P. G. and Arias, P. (2010). Error analysis of terrestrial laser scanning data by means of spherical statistics and 3D graphs. *Sensors*, 10, 10128–10145.
- Deems, J. and Painter, T. (2006). Lidar measurement of snow depth: accuracy and error sources. *International Snow Science Workshop* (pp. 330–338). Telluride, USA: Montana State University Library.
- Ehrlich, C. (2014). Terminological aspects of the Guide to the Expression of Uncertainty in Measurement (GUM). *Metrologia*, 51(4), S145–S154.
- El-Ashmawy, K. L. (2016). A simple technique for road surface modelling. *Geodesy and Cartography*, 42(3), 106–114.
- Eling, D. (2009). Terrestrisches laserscanning für die bauwerksüberwachung [Terrestrial laser scanning for building monitoring]. PhD thesis. Leibniz University of Hanover.
- Estonian Road Administration. (2001). Elastsete teekatendite projekteerimise juhend [Guide for the design of elastic pavements]. Tallinn: Estonian Road Administration, 1–50.
- Estonian Road Administration. (2008). Täiendavad nõuded topo-geodeetiliste uurimistöodele teede projekteerimisel [Additional requirements for topographic research in road design]. Tallinn: Estonian Road Administration, 1–10.
- Fraunhofer IFF. (2015). Fraunhofer Institute for Factory Operation and Automation (IFF), Guidelines on Laser Scanning in Plant Design. Magdeburg: Fraunhofer IFF.

- Golparvar-Fard, M., Bohn, J., Teizer, J., Savarese, S. and Peña-Mora, F. (2011). Evaluation of image-based modeling and laser scanning accuracy for emerging automated performance monitoring techniques. *Automation in Construction*, 20, 1143–1155.
- González-Jorge, H., Gonzalez-Aguilera, D., Rodriguez-Gonzalvez, P. and Arias, P. (2012). Monitoring biological crusts in civil engineering structures using intensity data from terrestrial laser scanners. *Construction and Building Materials*, 31, 119–128.
- Gottwald, R. (2008). Field procedures for testing terrestrial laser scanners (TLS) - a contribution to a future ISO standard. *FIG Working Week 2008 Integrating Generations* (pp. 1-14). Stockholm, Sweden: FIG.
- Gruen, A. and Akca, D. (2005). Least squares 3D surface and curve matching. *Journal of Photogrammetry and Remote Sensing*, 59, 151–174.
- GSA (U.S. General Services Administration). (2009). BIM Guide 03 – 3D Laser Scanning. Washington: GSA.
- Hancock, J. A. (1999). Laser intensity-based obstacle detection and tracking. Licentiate thesis. Carnegie Mellon University, USA.
- Hejbudzka, K., Lindenbergh, R., Soudarissanane, S. and Humme, A. (2010). Influence of atmospheric conditions on the range distance and number of returned points in Leica ScanStation 2 point clouds. *International Archives of Photogrammetry, Remote Sensing and Spatial Information Sciences, Vol. XXXVIII* (pp. 282–287). Newcastle, England: ISPRS.
- Higgins, S. (2007). 3D laser scanning market red hot: 2006 industry revenues \$253 million, 43% growth. *SparView*. Retrieved from www.spar3d.com.
- Hiremagalur, J., Yen, K. S., Lasky, T. A. and Ravani, B. (2009). Testing and performance evaluation of fixed terrestrial 3D laser scanning systems for highway applications. *TRB 88th Annual Meeting CD-ROM* (pp. 1–20). Washington, USA: National Academies of Sciences, Engineering, and Medicine.
- Hodge, R. A. (2010). Using simulated terrestrial laser scanning to analyse errors in high-resolution scan data of irregular surfaces. *ISPRS Journal of Photogrammetry and Remote Sensing*, 65, 227–240.
- Holst, C. and Kuhlmann, H. (2014). Aiming at self-calibration of terrestrial laser scanners using only one single object and one single scan. *Journal of Applied Geodesy*, 8(4), 295–310.
- Holst, C. and Kuhlmann, H. (2016). Challenges and present fields of action at laser scanner based deformation analyses. *Journal of Applied Geodesy*, 10(1), 1–9.
- Holst, C., Artz, T. and Kuhlmann, H. (2014). Biased and unbiased estimates based on laser scans of surfaces with unknown deformations. *Journal of Applied Geodesy*, 8(3), 169–184.
- ISO 8322-1:1989 Building construction - Measuring instruments. Brussels: European Committee for Standardization.
- JCGM 100:2008. Evaluation of measurement data - Guide to the expression of uncertainty in measurement. Sèvres Cedex, Paris: BIPM.

- Kaasalainen, S., Krooks, A., Kokko, A. and Kaartinen, H. (2009). Radiometric calibration of terrestrial laser scanners with external reference targets. *Remote Sensing*, 144–158.
- Kersten, T. P., Mechelke, K., Lindstaedt, M. and Sternberg, H. (2009). Methods for geometric accuracy investigations of terrestrial laser scanning systems. *Photogrammetrie - Fernerkundung - Geoinformation*, 9(4), 301–315.
- Kersten, T. P., Sternberg, H. and Mechelke, K. (2005). Investigations into the accuracy behaviour of the terrestrial laser scanning system Mensi GS100. *Optical 3-D Measurement Techniques VII* (pp. 122–131). Vienna, Austria: Vienna University of Technology.
- Koch, K.-R. (2008). Determining uncertainties of correlated measurements by Monte Carlo simulations applied to laser scanning. *Journal of Applied Geodesy*, 2(3), 139–147.
- Krooks, A., Kaasalainen, S., Hakala, T. and Nevalainen, O. (2013). Correction of intensity incidence angle effect in terrestrial laser scanning. *ISPRS Annals of the Photogrammetry, Remote Sensing and Spatial Information Sciences. II-5/W2* (pp. 145–150). Antalya, Turkey: ISPRS.
- Larsen, K. E., Lattke, F., Ott, S. and Winter, S. (2011). Surveying and digital workflow in energy performance retrofit projects using prefabricated elements. *Automation in Construction*, 20(8), 999–1011.
- Lee, H.-H. (2009). Optimizing schedule for improving the traffic impact of work zone on roads. *Automation in Construction*, 18, 1034–1044.
- Lerma García, J. L., Van Genechten, B., Heine, E. and Santana Quintero, M. (2008). *Theory and Practice on Terrestrial Laser Scanning: Training Material Based on Practical Applications*. Valencia: Universidad Politecnica de Valencia Editorial.
- Lichti, D. D. (2007). Error modelling, calibration and analysis of an AM–CW terrestrial laser scanner system. *ISPRS Journal of Photogrammetry and Remote Sensing*, 61(5), 307–324.
- Lichti, D. D. (2010). Terrestrial laser scanner self-calibration: correlation sources and their mitigation. *ISPRS Journal of Photogrammetry and Remote Sensing*, 65(1), 93–102.
- Löhmus, H., Ellmann, A., Märdla, S. and Idnurm, S. (2017, online). Terrestrial laser scanning for the monitoring of bridge load tests – two case studies. *Survey Review*, 1–15. DOI:10.1080/00396265.2016.1266117
- Maar, M. and Zogg, H.-M. (2014). WFD – wave form digitizer technology. *Leica White Paper*, 1–12. Retrieved from www.leica-geosystems.com.
- Määttä, K., Kostamovaara, J. and Myllylä, R. (1993). Profiling of hot surfaces by pulsed time-of-flight laser rangefinder techniques. *Applied Optics*, 32(27), 5334–5347.
- Mao, Q., Zhang, L., Li, Q., Hu, Q., Yu, J., Feng, S., Ochieng, W. and Gong, H. (2015). A least squares collocation method for accuracy improvement of mobile LiDAR systems. *Remote Sensing*, 7(6), 7402–7424.

- Murphy, M., McGovern, E. and Pavia, S. (2013). Historic building information modelling – adding intelligence to laser and image based surveys of European classical architecture. *ISPRS Journal of Photogrammetry and Remote Sensing*, 76, 89–102.
- Niemeier, W. and Tengen, D. (2016). Uncertainty assessment in geodetic network adjustment by combining GUM and MC. *3rd Joint International Symposium on Deformation Monitoring (JISDM)* (pp. 1–11). Vienna, Austria: Vienna University of Technology.
- Nuttens, T., Stal, C., De Backer, H., Schotte, K., Van Bogaert, P. and De Wulf, A. (2014). Methodology for the ovalization monitoring of newly built circular train tunnels based on laser scanning: Liefkenshoek Rail Link (Belgium). *Automation in Construction*, 43, 1–9.
- Pandžić, J., Pejić, M., Božić, B. and Erić, V. (2017). Error model of direct georeferencing procedure of terrestrial laser scanning. *Automation in Construction*, 78, 13–23.
- Pejić, M. (2013). Design and optimisation of laser scanning for tunnels geometry inspection. *Tunnelling and Underground Space Technology*, 37, 199–206.
- Pesci, A. and Teza, G. (2008). Effects of surface irregularities on intensity data from laser scanning: an experimental approach. *Annals of Geophysics*, 51(5/6), 839–848.
- Pesci, A., Teza, G., Bonali, E., Casula, G. and Boschi, E. (2013). A laser scanning-based method for fast estimation of seismic-induced building deformations. *ISPRS Journal of Photogrammetry and Remote Sensing*, 79, 185–198.
- Reshetyuk, Y. (2009). Self-calibration and direct georeferencing in terrestrial laser scanning. PhD thesis. KTH Royal Institute of Technology in Stockholm.
- Riveiro, B., Morer, P., P., A. and De Arteaga, I. (2011). Terrestrial laser scanning and limit analysis of masonry arch bridges. *Construction and Building Materials*, 25(4), 1726–1735.
- Roca-Pardiñas, J., Argüelles-Fraga, R., López, F. d. and Ordóñez, C. (2014). Analysis of the influence of range and angle of incidence of terrestrial laser scanning measurements on tunnel inspection. *Tunnelling and Underground Space Technology*, 43, 133–139.
- Rönholm, P., Nuikka, M., Suominen, A., Salo, P., Hyyppä, H., Pöntinen, P., Haggrén, H., Vermeer, M., Puttonen, J., Hirsi, H., Kukko, A., Kaartinen, H., Hyyppä, J. and Jaakkola, A. (2009). Comparison of measurement techniques and static theory applied to concrete beam deformation. *The Photogrammetric Record*, 24(128), 351–371.
- Schaer, P., Skaloud, J., Landtwing, S. and Legat, K. (2007). Accuracy estimation for laser point cloud including scanning geometry. *The 5th International Symposium on Mobile Mapping Technology* (pp. 1–8). Padua, Italy: ISPRS.

- Schofield, W. and Breach, M. (2007). *Engineering Surveying, Sixth edition*. Elsevier.
- Schulz, T. (2007). Calibration of a terrestrial laser scanner for engineering geodesy. PhD thesis. Swiss Federal Institute of Technology in Zurich.
- Sładek, J. A. (2016). *Coordinate Metrology. Springer Accuracy of Systems and Measurements*. Springer.
- Soudarissanane, S. (2016). The geometry of terrestrial laser scanning; identification of errors, modeling and mitigation of scanning geometry. PhD thesis. Delft University of Technology.
- Soudarissanane, S., Lindenbergh, R., Menenti, M. and Teunissen, P. (2009). Incidence angle influence on the quality of terrestrial laser scanning points. *ISPRS Workshop Laserscanning*. Volume XXXVIII (pp. 183–188). Paris, France: ISPRS.
- Soudarissanane, S., Lindenbergh, R., Menenti, M. and Teunissen, P. (2011). Scanning geometry: influencing factor on the quality of terrestrial laser scanning points. *ISPRS Journal of Photogrammetry and Remote Sensing*, 66(4), 389–399.
- Tang, P. and Akinci, B. (2012). Formalization of workflows for extracting bridge surveying goals from laser-scanned data. *Automation in Construction*, 22, 306–319.
- Tang, P., Anil, E., Akinci, B. and Huber, D. (2011). Efficient and effective quality assessment of as-is building information models and 3D laser-scanned data. *ASCE International Workshop on Computing in Civil Engineering* (pp. 488–493). Florida, USA: ASCE.
- Teede Tehnokeskus AS. (2007). Liiklusloenduse tulemused 2007 aastal [Results of traffic count in 2007]. Tallinn: Teede Tehnokeskus AS.
- Tsakiri, M., Pagounis, V. and Arabatzi, O. (2015). Evaluation of a pulsed terrestrial laser scanner based on ISO standards. *Surface Topography: Metrology and Properties*, 3(1), 1–9.
- Volk, R., Stengel, J. and Schultmann, F. (2014). Building Information Modeling (BIM) for existing buildings – literature review and future needs. *Automation in Construction*, 38, 109–127.
- Vosselman, G. and Maas, H.-G. (2010). *Airborne and Terrestrial Laser Scanning*. Whittles Publishing.
- Wagner, W., Ullrich, A., Ducic, V., Melzer, T. and Studnicka, N. (2006). Gaussian decomposition and calibration of a novel small-footprint full-waveform digitising airborne laser scanner. *ISPRS Journal of Photogrammetry and Remote Sensing*, 60(2), 100–112.
- Wang, J., Kutterer, H. and Fang, X. (2015). External error modelling with combined model in terrestrial laser scanning. *Survey Review*, 47(346), 11.
- Wehr, A. and Lohr, U. (1999). Airborne laser scanning—an introduction and overview. *ISPRS Journal of Photogrammetry and Remote Sensing*, 54(2-3), 68–82.

- Weichel, H. (1990). *Laser Beam Propagation in the Atmosphere*. Bellingham: SPIE Press.
- Weygant, R. S. (2011). *BIM Content Development: Standards, Strategies, and Best Practices*. Hoboken: Wiley.
- Wilson, L., Rawlinson, A., Mitchell, D. S., McGregor, H. C. and Parsons, R. (2013). The Scottish Ten project: collaborative heritage documentation. *International Archives of the Photogrammetry*. Volume XL-5/W2 (pp. 685–690). Strasbourg, France: ISPRS.
- Wunderlich, A. T. (2003). Terrestrial laser scanners - an important step towards construction information. *FIG Working Week 2003* (pp. 1–11). Paris, France: FIG.
- Wunderlich, A. T., Niemeier, W., Wujanz, D., Holst, C., Neitzel, F. and Kuhlmann, H. (2016). Areal deformation analysis from TLS point clouds - the challenge. *Allgemeine Vermessungs-Nachrichten*, 123(11–12), 340–351.
- Xiong, X., Adan, A., Akinci, B. and Huber, D. (2013). Automatic creation of semantically rich 3D building models from laser scanner data. *Automation in Construction*, 31, 325–337.
- Xuan, W., Hua, X., Zou, J. and He, X. (2016). Determining the deformation monitorable indicator. *Journal of the Indian Society of Remote Sensing*, 45(1), 1–9.
- Yang, H., Omidalizarandi, M., Xu, X. and Neumann, I. (2017). Terrestrial laser scanning technology for deformation monitoring and surface modeling of arch structures. *Composite Structures*, 169, 173–179.
- Yu, W.-D. and Lo, S.-S. (2005). Time-dependent construction social costs model. *Construction Management and Economics*, 23(3), 327–337.
- Zhengchun, D., Zhaoyong, W. and Jianguo, Y. (2016). Point cloud uncertainty analysis for laser radar measurement system based on error ellipsoid model. *Optics and Lasers in Engineering*, 79, 78–84.
- Zogg, H.-M. and Ingensand, H. (2008). Terrestrial laser scanning for deformation monitoring – load tests on the Felsenau viaduct (CH). *XXI ISPRS Congress* (pp. 555–562). Beijing, China: ISPRS.

ACKNOWLEDGEMENTS

This thesis was conducted in the Road Engineering and Geodesy Research Group in the Department of Civil Engineering and Architecture of Tallinn University of Technology.

I would like to express my sincere gratitude to my supervisor Prof. Artu Ellmann for his encouragement, guidance and support throughout my doctoral studies. I also thank him for the effort and time he has put in helping me to write the papers and this thesis.

I am very thankful to all my colleagues at the TTK University of Applied Sciences. Especially I would like to express my gratitude to the former Dean Jüri Tamm and the present Dean Prof. Martti Kiisa for encouraging me and providing me with the opportunity to pursue my doctoral studies. Also, I am sincerely grateful for the encouragement and support from Associate Prof. Raivo Ranne. My sincere gratitude goes to Siiri Künnapas for her help, valuable comments and advice throughout my studies.

Last but not least, I am very grateful to my wife and my children for their endless love and support. My special thanks go to my father and my mother, my brothers and sisters and their families. I also thank my relatives and friends for their support.

ABSTRACT

The terrestrial laser scanning technology (TLS) has existed for almost two decades. The TLS technology has been widely used in the architectural, engineering, construction and facility management (AEC/FM) industry for different purposes (e.g. designing, documentation etc.). The objective of the present doctoral thesis is to investigate TLS applications for engineering structure surveys. The thesis consists of two parts.

In the first part of the thesis, a method for estimating the range and spatial distribution of TLS uncertainties occurring while surveying engineering structures is presented. The emphasis is on along-normal uncertainties (ANU) of the surfaces to be surveyed. The presented methodology is numerically verified, and the results are compared with the results of previous empirical studies. The developed method for calculating ANU values make it possible to better plan different scanning activities. It helps better to optimize scanning work and improve the quality of TLS survey data in terms of ANU values. The proposed ANU calculation method is found to be especially very beneficial for surveying projects where deformations are small and repeating the measurements is not possible.

The second part of the thesis focuses on the application of the TLS technology for engineering structure surveys. The developed method for calculating ANU values, proposed in the first part, was tested in two empirical case studies. The first case study deals with the monitoring of deformations occurring during a unique static bridge load test using the TLS technology. The results obtained by TLS were verified by precise levelling. The second case study deals with the monitoring of road surface deformations occurring due to frost heave at selected road sections using the TLS technology. The results obtained by TLS were verified by geometric levelling. The result of using ANU values for the empirical case studies indicated benefits in assessing the uncertainties of the obtainable results. The application of TLS for road surveying and for building surveying purposes is also investigated considering limitations stated in the literature: *(i)* scanning under a large angle of incidence, *(ii)* the influence of atmospheric conditions to TLS surveying and *(iii)* validation of the obtained TLS results in engineering applications. The results indicated that a large angle of incidence does not have a significant effect on scanning results of TOF technology. This is also confirmed by the results of studies from the literature. Atmospheric conditions were mainly related to precipitation where laser signals were reflecting back from raindrops, and to the object's surface reflectivity deterioration due to becoming wet. The results of the study indicated that supplementary geodetic measurements are also suggested for the cases where it is necessary to validate TLS results, e.g. in building surveys and in road surveys with TLS data.

Keywords: *surveying uncertainties, measuring noise, error, point cloud, geometric modelling.*

KOKKUVÕTE

Terrestriline laserskaneerimine (TLS) on eksisteerinud üle kahe aastakümne. Tänu kogutavate ruumiandmete detailsusele on TLS leidnud laialdast kasutust nii arhitektuuri, inseneeria ja ehituse valdkonnas, aga ka rajatiste haldamise valdkonnas. Käesoleva doktoriväitekirja eesmärgiks on uurida TLS-i rakendust peajasjalikult ehitusvaldkonnas. Käesolev doktoriväitekiri on jaotatud kahte ossa.

Doktoriväitekirja esimeses osas esitletakse uudset meetodit, kuidas hinnata tasapinna normaalisuunalist mõõtemääramatust (ANU) TLS mõõdistamisel. Tuletatud meetodit kontrolliti läbi geomeetriliste seoste. Samuti võrreldi saadud tulemusi eelnevalt kirjanduses esitatud empiiriliste katsete tulemustega. Lisaks katsetati loodud meetodit kahe ehitusmõõdistamise juhtumi puhul. Esimene mõõdistamisjuhtum käsitles betoonsilla koormuskatsetuse TLS monitooringut. Teine mõõdistamisjuhtum käsitles maantee külmakergetest põhjustatud deformatsioonide TLS monitooringut. Uuringu tulemusel järeldati, et esitletud ANU arvutusmeetod on sobiv viis hindamiseks saadavaid mõõtemääramatuseid nii mõõdistuseelselt kui ka -järgselt. See on kindlasti abiks erinevate suuremat täpsust nõudvate mõõdistustööde planeerimisel ja ka teostamisel. Samuti järeldati, et kuna hetkel puuduvad TLS seadmetele ühtsed täpsuslikud standardid on instrumendi tootjate poolsed täpsuslikud parameetrid pigem üldsõnalised.

Doktoriväitekirja teises osas keskenduti TLS-i rakendamise uurimisele ehitusvaldkonnas. Vaatluse alla on võetud kirjanduses käsitletud ühed TLS-i märkimisväärsemad rakendamise piirangud nagu: (i) TLS mõõdistamisel suur langemisenurk, (ii) TLS-i mõõdistuskeskkonna mõju, ja (iii) TLS-i mõõdistustulemuste usaldusväarsuse tagamine. Uuringu tulemusel järeldati, et läbiviidud TLS mõõdistustel ei täheldatud suure langemisenurga ebaproportsionaalset mõju mõõdistamise müra kasvule. Tõdeti, et langemisenurga mõju võib olla seotud kasutatava TLS-i tehnoloogiaga. Mõõdistuskeskkonna mõju on seotud enamasti sademetega, kus mõõdistuse müra võib tekkida tänu lasersignaali tagasipeegeldumisele näiteks vihmapiiskadelt. Samuti mõjutavad sademed ka pinna peegeldumisomadusi. Täheldati, et tänu pinna peegeldusomaduste halvenemisele väheneb märkimisväärselt mõõdistavate punktide arv. Käesoleval hetkel puuduvad TLS seadmete täpsusstandardid, mille alusel on seadmete täpsuslikud parameetrid määratletud. Sellega seoses on TLS mõõdistustulemuste valideerimiseks kindlaim viis kasutada mõnda suurema täpsusega tehnoloogiat (geomeetiline nivelleerimine või tahhümeetria).

PUBLICATIONS

Mill, T. and Ellmann, A. (2017, online). Assessment of along-normal uncertainties for application to terrestrial laser scanning surveys of engineering structures. *Survey Review*, 1–16. DOI: 10.1080/00396265.2017.1361

Assessment of along-normal uncertainties for application to terrestrial laser scanning surveys of engineering structures

Tarvo Mill * and Artu Ellmann

A method for estimating the range and spatial distribution of terrestrial laser scanning uncertainties occurring during the survey of engineering structures is presented and numerically verified. The emphasis is on the assessment of along-normal uncertainties of the surface to be surveyed. To investigate the behaviour of such uncertainties, various surveying scenarios are simulated and studied. Theoretical derivations are numerically verified, and these results are compared with those of previous empirical studies. The influence of along-normal noise on geometric modelling of surveyed surfaces is studied. In addition, suggestions are provided for how to optimise scanning locations, yielding the reduced ANU.

Keywords: Surveying uncertainties, Data noise, Error, Data simulation, Optimisation of TLS surveys

Introduction

Terrestrial laser scanning (TLS) technology has many applications due to its ability to determine the detailed 3D geometry of engineering structures within a relatively short period of time. For instance, TLS has been used in various engineering applications, such as the surveying of technical structures (Riveiro *et al.* 2011, Pejić 2013, Mill *et al.* 2014, Nuttens *et al.* 2014) and the monitoring of structural deformations (González-Aguilera *et al.* 2008, Pesci *et al.* 2013, Mill *et al.* 2015). A TLS survey provides a more complete spatial overview than that achieved using a limited number of conventional surveying points at pre-selected locations.

Although TLS would be an appealing tool for as-built surveying and the determination of the ranges and spatial distribution of deformations of the surface of interest, two very challenging problems remain: (i) gaining sufficient knowledge of the accuracy of TLS data and (ii) determining optimal data processing methods. These two problems have required the use of conventional reference geodetic technology (e.g. precise levelling or tacheometry) to verify TLS results.

This study is concerned primarily with the first problem, and its aim is to assess uncertainties in TLS data that occur during the surveying of engineering structures. The study makes use of the concept of combined standard uncertainty (CSU), which originates from the classical theory of geodetic measurement errors (e.g. Bjerhammar 1973) and has been adopted in contemporary guidelines for the measurement industry (JCGM 100:2008). CSU

has been used in many previous studies, e.g. Koch (2008), Alkhatib *et al.* (2009), Mill *et al.* (2014, 2015) and Niemeier and Tengen (2016). In addition, Cuartero *et al.* (2010) analysed survey point locational errors by statistically analysing spherical data, and Zhengchun *et al.* (2016), Chen *et al.* (2016) and Xuan *et al.* (2016) investigated TLS uncertainties by modelling an error ellipsoid. Nevertheless, these studies generally focus on survey point uncertainties relative to the TLS coordinate origin, rather than with respect to the principal axes of the object itself. In contrast, the present study focuses on along-normal uncertainties (ANU) of TLS-surveyed surfaces, as these uncertainties have a critical influence on geometric modelling results. The ANU are calculated using estimates of CSU.

This study also investigates the optimisation of scanning locations with the aim of reducing ANU. Optimisation issues have been addressed in a few previous studies. For example, Argüelles-Fraga *et al.* (2013) and Roca-Pardiñas *et al.* (2014) sought to determine optimal scanning locations for tunnel surveys, and Soudarissanane *et al.* (2009) and Soudarissanane (2016) introduced a method for optimising scanning locations for building surveys. These studies were primarily concerned with the problem of how to avoid surveying with large angles of incidence, which are considered by some to be the main cause of surveying noise (e.g. Lichti 2007, Soudarissanane *et al.* 2009, 2011). It is, however, also possible to provide suggestions for optimal scanning locations based on estimated ANU and the approximate geometry of the object. Different TLS station locations can be selected and tested to determine expected measurement uncertainty. It may be necessary to simulate different scenarios to ensure that the final survey has been rigorously carried out, especially when failure is not an option (e.g. in the case of bridge load tests, deformation measurements, as-built

Road Engineering and Geodesy Research Group, Department of Civil Engineering and Architecture, School of Engineering, Tallinn University of Technology, Ehitajate tee 5, 19086 Tallinn, Estonia

*Corresponding author, email tarvo.mill@tkk.ee

surveys). The study also investigates the along-normal influence of surveying noise on geometric modelling from TLS point cloud.

The paper is structured as follows. The introduction is followed by a review of TLS uncertainties, with an emphasis on scanning geometry. Then a method is presented for calculating ANU, accompanied with numerical verification. The next section investigates the distribution of ANU on simulated engineering structures. In the following section, random noise is imposed on the data to simulate realistic conditions, and the data are then geometrically modelled. Conclusions are then drawn on the basis of modelling results. This is followed by a discussion of how scanning locations can be optimised in the case of simulated engineering structures. A brief summary concludes the paper.

CSU expressions for the TLS survey

TLS uncertainties

Similarly to conventional surveying technologies, TLS is also subject to different sources of uncertainties – related to equipment, object properties, scanning geometry, environmental conditions and even human error. Each of these sources of uncertainty contributes to the overall uncertainty budget of TLS surveys. In some cases, there is a need to pre-assess the magnitude and distribution of possible uncertainties due to these sources.

As in the case of other geodetic instruments, the person carrying out the TLS survey can be a source of human error. The magnitude of this error depends on the level of the operator’s basic land surveying and data processing skills, as well as on his or her theoretical background and practical surveying experience. Human error, however, will not be considered in this study.

Uncertainties related to equipment depend largely on the metrological characteristics of the instrument used. Unfortunately, the manufacturers of scanners usually provide only the general technical specifications of an instrument, omitting the instrument’s individual calibration results. Stated characteristics often do not follow generally accepted criterion set by ISO, DIN or other standards. In effect, these characteristics are just estimates (Gottwald 2008, Cuartero *et al.* 2010, Tsakiri *et al.* 2015).

Object-related uncertainties are associated with the object’s physical properties, such as surface colour, reflectivity, roughness, temperature and moisture level (Kersten *et al.* 2005, Pesci and Teza 2008, Lichti 2010, Soudarissanane *et al.* 2011, Roca-Pardiñas *et al.* 2014).

Atmospheric and environment uncertainties are mainly associated with atmospheric effects (humidity, dust, temperature, etc.) on the scanning device (Borah and Voelz 2007, Pfeifer *et al.* 2007).

TLS survey can also be influenced by systematic effects, which may significantly distort the expected results (e.g. Kersten *et al.* 2005, Holst *et al.* 2014a). The presence of systematic effects can be determined and minimised using different calibration methods, as proposed, for example, by Reshetyuk (2009), Chow *et al.* (2012), Tsakiri *et al.* (2015) and Holst and Kuhlmann (2014, 2016). Accounting for systematic effects is not, however, within the scope of the present study.

In general, the combined uncertainty of a survey point, including the uncertainties arising due to the instrument,

environment, object properties and scanning geometry, can be estimated using the following equation (Soudarissanane 2016):

$$u_{\hat{p}} = \sqrt{u_{\text{instr}}^2 + \eta_{\text{atm}}^2 + u_{\text{material}}^2 + u_{\text{geom}}^2} \quad (1)$$

where $u_{\hat{p}}$ represents the estimated combined uncertainty of a TLS survey point, u_{instr} is the instrumental CSU, which comprises uncertainties, e.g. due to the instrument’s mechanical design, technical limitations and hardware, η_{atm} is uncertainty due to atmospheric transmittance, u_{material} is uncertainty due to object surface properties and u_{geom} is uncertainty due to scanning geometry.

For the purposes of the present study, it is assumed that errors are normally distributed and uncorrelated. In this case, for each term on the right-hand side of equation (1), the combined standard uncertainty (CSU) values for an individual TLS survey point can be calculated by summing up the partial contributions of all relevant uncertainty sources (JCGM 100:2008):

$$u_{\hat{p}}^2 = \sum_{i=1}^n \left(\frac{\partial f}{\partial w_i} \right)^2 u_{w_i}^2 \quad (2)$$

where $u_{\hat{p}}$ is the standard uncertainty of a survey point, whereas \hat{P} is an estimate of the location (3D position, expressible via specific x , y and z -coordinates) of the actual survey point P , f is the function $P = f(w_i)$ associated with the observations (w_i), where $i = 1, \dots, n$. The symbol u_{w_i} is the standard uncertainty of an i -th observable (e.g. distance, angle, height difference).

The total magnitude of CSU is obtained by adding up the components on the right-hand side of equation (1). It should be noted that the contribution to CSU by atmospheric conditions (η_{atm}) and object surface properties (u_{material}) is not considered in this study. Note that this contribution is quite specific to each TLS survey and tends to cause systematic measurement errors. The interested reader is referred to Kersten *et al.* (2005), Pfeifer *et al.* (2007), and Borah and Voelz (2007), Pesci and Teza (2008), Lichti (2010), Soudarissanane *et al.* (2011), Roca-Pardiñas *et al.* (2014), where systematic error due to an object’s physical properties and the environment is considered.

This study focuses on uncertainties arising during the survey of engineering structures, where the general surveying requirements (instruments, methods, accuracy etc.) are rigorous. In particular, the influences of instrumental metrological characteristics and scanning geometry on ANU are investigated. In addition, a method is developed on the basis of CSU for calculating ANU in the general cases. The developed method allows a priori quality assessment of the expected scanning results, and thus help design better the TLS surveys.

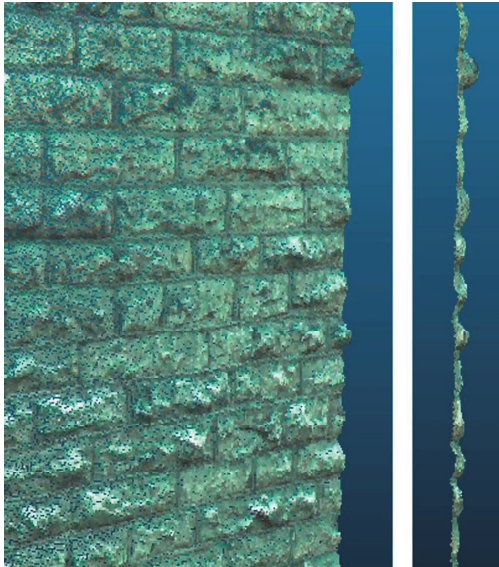
Uncertainties due to scanning geometry

As debated in the literature, e.g. Lichti (2007), Soudarissanane *et al.* (2009, 2011) and Soudarissanane (2016), TLS measurement noise is mostly influenced by scanning geometry, which is correlated to distance, beam divergence, angle of incidence (for its definition, see Fig. 2), and reflectance. Note that the aforementioned studies concluded that scanning should be conducted at angles of incidence of less than approximately 60°. If this threshold

is exceeded, a sharp increase in overall measurement noise occurs. It should be noted that the aforementioned studies used only phase-shift (PS) scanners. Kaasalainen *et al.* (2009) and Soudarissanane (2016) explain that the rescaling of measurements by the digital signal processing unit of PS scanners at the near-zero angle of incidence leads to better results. An empirical study by Kersten *et al.* (2009) investigated achievable accuracies using both PS and time-of-flight (TOF) scanners. In the case of PS scanners, surveying noise increased significantly as the angle of incidence increased. This is similar to results reported, for example, by Soudarissanane *et al.* (2011). In contrast, TOF scanners did not exhibit significant effects due to the change of angle of incidence. A study by Kersten *et al.* (2009) thus concluded that a large angle of incidence is not critical in the case of TOF scanners. Another study by Kersten *et al.* (2005) reported poorer point accuracy when a smooth surface is measured in a perpendicular direction (i.e. with a near-zero angle of incidence $\alpha = 0^\circ$) using TOF scanners.

The differences in the achieved results of TOF and PS scanners are presumably due to the differences in the distance measuring technology and digital signal processing methods (Reshetyuk 2009). Indeed, the angle of incidence may be critical in TLS surveys of rather smooth surfaces (e.g. plywood, polystyrene), as shown by previous studies, e.g. Soudarissanane *et al.* (2011) and Kersten *et al.* (2005).

Uneven and coarse-grained surfaces are generally associated with historical buildings (Fig. 1) and also many pre-manufactured contemporary structural elements. Thus, a laser signal at a near perpendicular angle of incidence (i.e. 90° with respect to the surface normal) may easily backscatter from such coarse-grained surfaces. Nevertheless, further derivations aim to include the possible influence of the angle of incidence on ANU.



1 A sample of a point cloud of a building's limestone façade, front view (left-hand side) and side view (right-hand side). The limestone joints are at intervals of approx. 15 cm

The instrument's axial orientation, the measured (or predicted) quantities (θ , φ and ρ) and the scanning geometry with respect to the surface to be surveyed, let it be a plane, are illustrated in Fig. 2. The scanning geometry can be described via distance (ρ) and angle of incidence (α) between the vector of emitted laser beam (\vec{SP}) and the surface normal (\vec{n}), see Fig. 2. The shortest distance (d) can also be obtained via angle of incidence and the measured distance as follows (cf. Fig. 2):

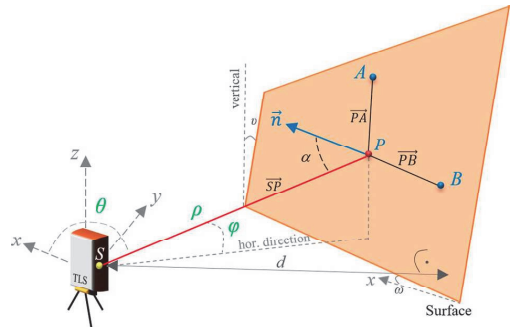
$$d = \rho \sin(90^\circ - \alpha) = \rho \cos \alpha \quad (3)$$

The interrelations between spherical polar (θ , φ and ρ) and the x , y and z -coordinate sets of an individual survey point yield (cf. also Fig. 2):

$$\begin{bmatrix} x \\ y \\ z \end{bmatrix} = \begin{bmatrix} \rho \cos \theta \cos \varphi \\ \rho \sin \theta \cos \varphi \\ \rho \sin \varphi \end{bmatrix} \quad (4)$$

The z -axis of scanners equipped with a dual-axis compensator coincides with the zenith direction.

To calculate CSU values, the partial derivatives of TLS observations (equation (4)) with respect to each variable are taken (i.e. for x , $dx/d\rho$; $dx/d\varphi$; $dx/d\theta$; analogously, also for the y - and z -components), and then inserted into equation (2), using also the uncertainty parameters for the TLS provided by the manufacturer, the following



2 TLS measurables with respect to surface (a plane). \vec{SP} is a vector (with a length ρ) of the transmitted laser beam from TLS centre to the survey point (P) on the surface. Horizontal angle (θ , where $0^\circ \leq \theta \leq 360^\circ$ arc degrees) to P is accounted from an arbitrary initial direction (here accounted from the TLS-device x -axis), whereas vertical angle (φ , where $-90^\circ \leq \varphi \leq +90^\circ$ arc degrees) is accounted from the horizontal plane (embedding the origin of the TLS coordinate axes, S). α is the angle of incidence between the falling laser beam and the surface normal (\vec{n}). Vectors \vec{PA} and \vec{PB} are residing on the plane between arbitrary surface points A , P and B , these two vectors can be used for determining the plane coefficients. d is the shortest distance in the direction of the surface normal from the scanner centre (i.e. d is strictly parallel to \vec{n}). In general, the surface is horizontally rotated by an angle (ω , where $0^\circ \leq \omega \leq 180^\circ$ arc degrees) with respect to TLS x -axis, the surface is also vertically inclined at an angle (u , where $0^\circ \leq u \leq 180^\circ$ arc degrees) from the vertical (zenith), plumb line, which is parallel to TLS' z -axis)

equations are arrived at

$$u_{\hat{x}} = [(\cos \theta \cos \varphi)^2 u_{\text{dist}}^2 + \rho^2 (\cos \varphi \sin \theta)^2 u_{h,\text{angle}}^2 + \rho^2 (\cos \theta \sin \varphi)^2 u_{v,\text{angle}}^2] \frac{1}{2} \quad (5)$$

$$u_{\hat{y}} = [(\sin \theta \cos \varphi)^2 u_{\text{dist}}^2 + \rho^2 (\cos \varphi \cos \theta)^2 u_{h,\text{angle}}^2 + \rho^2 (\sin \theta \sin \varphi)^2 u_{v,\text{angle}}^2] \frac{1}{2} \quad (6)$$

$$u_z = [(\sin \varphi)^2 u_{\text{dist}}^2 + \rho^2 (\cos \varphi)^2 u_{v,\text{angle}}^2] \frac{1}{2} \quad (7)$$

where $u_{\hat{x}}$, $u_{\hat{y}}$ and u_z are CSU with respect to the corresponding TLS coordinate axis, u_{dist} is the scanner's standard distance uncertainty, $u_{h,\text{angle}}$ is the scanner's standard horizontal angle and $u_{v,\text{angle}}$ vertical angle uncertainty. The scanner's standard uncertainty values can be obtained from the manufacturer's specifications or from the individual calibration results.

These expressions are to be used to derive ANU, taking into account scanning geometry for general cases.

ANU of TLS-surveyed surface

A special case

In general, TLS data cloud is geometrically modelled to determine, for example, the object's conformance with design parameters and the deformations. It is essential that survey points lie directly on the surveyed surface, or at least, in its closest vicinity, i.e. within the range of expected measurement noise. Ideally, the resulting layer of data would be infinitesimally thin. Therefore, in TLS surveys, it is important to be able to estimate the magnitude of ANU relative to the surface, while point location uncertainties along the surface are less relevant, as these have an insignificant effect on geometric modelling results. Uncertainties in the along-normal direction play a significant role especially in construction surveys, e.g. as-built surveys and deformation monitoring.

Some modelling methods, in particular, statistical gridding methods, e.g. Mao *et al.* (2015), and other iterative modelling methods, e.g. Gruen and Akca (2005) and Holst *et al.* (2014a), use uncertainty estimates to properly weigh the data to be modelled. For this reason, it is also important to provide uncertainty estimates for each data point after the field surveys have been carried out, i.e. not only during the design stage of the surveys.

Expressions 5, 6 and 7 allow the estimation of each uncertainty component relative to the TLS axes. In general cases, the surface normal (\vec{n}) can be described using all three coordinate components ($\vec{n} = (a, b, c)$), cf. further sections). This is not convenient when estimating ANU. The following sections tackle the relation between the TLS coordinate system (denoted by x, y, z) and the object's coordinate system (denoted by X, Y, Z). For instance, the object's X -axis can be directed horizontally along the plane-like surface to be surveyed, the Z -axis, vertically along the surface (thus not necessarily in the 'up' direction, e.g. in the case of tilted surfaces), and the Y -axis, perpendicular to the surface. Note that the horizontal angle (θ , cf. Fig. 2) is entirely

dependent on the direction of the scanner's x -axis. Today, the directions of coordinate axes of many modern TLS instruments (e.g. Leica C10 and P20) can be set at the survey site just before measurements are taken. In addition, the orientation of the coordinate system and the location of the scanner relative to the object can be predetermined on the basis of existing sources, e.g. plans, digital surface models, airborne laser scanning data and web maps. It is then possible to estimate values for the measured quantities (θ , φ and ρ) beforehand (provided that TLS locations can be pre-defined) and thus, estimate the approximate coordinates (x, y, z) of the surface of interest already at the survey design stage.

The maximum ANU estimates occur in special cases where the TLS axes and the object's axes are parallel (considered the worst-case scenario). For example, the TLS x -axis is set parallel to the object's X -axis. Thus, $u_{\hat{y}}$ is parallel to the surface normal, and ANU can be calculated using only equation (6). The measured quantities θ and φ are 90° and 0° , respectively. In this case, equation (6) reduces to u_{dist} only:

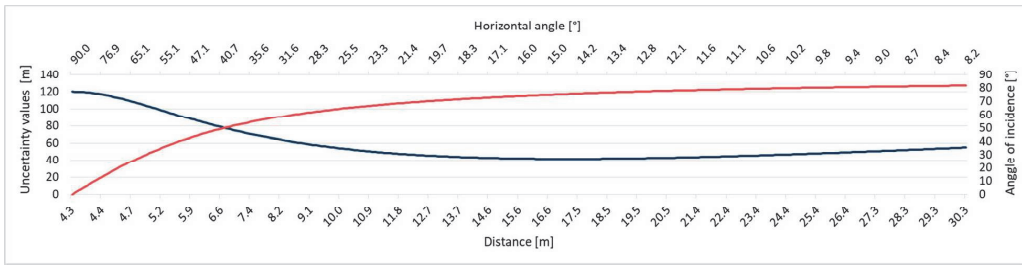
$$u_{\hat{y}} = [(\sin \theta \cos \varphi)^2 u_{\text{dist}}^2 + \rho^2 (\cos \varphi \cos \theta)^2 u_{h,\text{angle}}^2 + \rho^2 (\sin \theta \sin \varphi)^2 u_{v,\text{angle}}^2] \frac{1}{2} \\ \xrightarrow{\text{with } \theta = 90^\circ \text{ and } \varphi = 0^\circ} [(\sin \theta \cos \varphi)^2 u_{\text{dist}}^2] \frac{1}{2} = u_{\text{dist}}^2 \quad (8)$$

The result in equation (8) indicates that ANU is highly correlated with the values of the angles θ and φ (cf. equation (6)).

A numerical example of the worst-case scenario is provided based on simulated data points that form a horizontal line on a vertical wall. The scanner is located at an arbitrary distance from the object, in this case 4.3 m, a realistic surveying distance from an object. Metrological characteristics for an instrument are generally provided by manufacturers at a 68.3% (one sigma) confidence level. To have a more practical accuracy estimate, the characteristic must be multiplied by the factor 3, increasing the confidence level to 99.7% (three sigma), the generally accepted uncertainty tolerance in surveying. Therefore, rather than using the typical metrological parameter values of $u_{\text{dist}} = 0.004$ m and $u_{h,\text{angle}} = 12''$ (which are, for example, provided by manufacturers of widely used TOF scanners, e.g. Leica C10 and Leica P20), values which are three times larger are used: $u_{\text{dist}} = 0.012$ m and both $u_{h,\text{angle}}$ and $u_{v,\text{angle}} = 36''$ in numerical verifications.

The results of the numerical example of the worst-case scenario are illustrated in Fig. 3. A maximum ANU value of $u_{\hat{y}} = 0.012$ m is obtained, as expected (cf. equation (8)), when θ is equal to 90° , at the closest distance to the scanner (i.e. 4.3 m). In the example (Fig. 3), as the distance (ρ) increases, the angle of incidence (α) also increases, whereas the horizontal angle (θ) decreases. The relationship between α and θ is in this case simply $90^\circ - \theta = \alpha$.

In general, ANU values decrease (i.e. accuracy of measurements increases) from the point where θ is equal to 90° (the angle of incidence is 0°) until reaching their minimum (i.e. the most accurate point) at approx. 17 m from the scanner θ of 14° , i.e. $\alpha = 76^\circ$ (Fig. 3). This is



3 Calculated uncertainties of a horizontal line on a vertical wall. The decreasing line indicates ANU (values on the left-hand vertical scale); the increasing line indicates the angle of incidence (values on the right-hand vertical scale). The horizontal angle θ (top horizontal scale) at the closest point of 4.3 m equals 90° (i.e. $\alpha = 0^\circ$) and at the longest distance (30.3 m) approx. 8° (corresponding thus to the angle of incidence 82°)

because the influence of u_{dist} (0.012 m) decreases as the value of $\sin(\theta)$ decreases, cf. equation (8). Then ANU gradually begins to increase due to the increasing influence of the distance (ρ). Also the value of $\cos(\theta)$ increases as θ decreases from 90° to zero. Apparently, increasing thus the angle of incidence affects ANU only insignificantly, cf. Fig. 3.

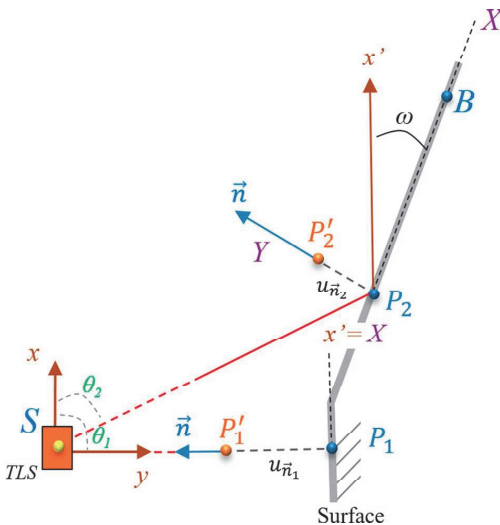
The foregoing described the special case ANU where the TLS axes are strictly parallel to the object's axes. Since such cases are not very typical for TLS projects, the following sections elaborate on a method for calculating ANU for the general case, where the TLS axes and object's axes are not parallel.

General expressions

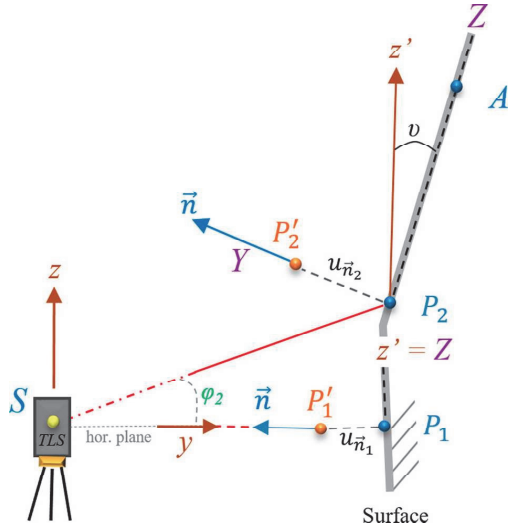
Although in the special case (cf. previous section), the TLS axes (x, y, z) can be parallel to some of the object's axes (X, Y, Z), in the general case, the object's coordinate system is not parallel to the TLS coordinate system.

Point location uncertainty in the surface normal direction can be calculated stepwise: (i) calculating the horizontal angle (ω) between the x -axis and X -axis, (ii) calculating the inclination angle (ν) between the z -axis and Z -axis (iii) projecting the uncertainties onto the surface normal. These steps will be reviewed below.

The necessary horizontal rotation angle (ω) in the 2D plane can be calculated using an arbitrary point B on



4 Top view of the vertical sub-surfaces, the furthestmost one being horizontally rotated to an angle ω (around z -axis) between the TLS coordinate system's x -axis and the object's X -axis. The uncertainties $u_{\bar{n}_1}$ and $u_{\bar{n}_2}$ are parallel to the object's Y -axis and coinciding thus with the surface normal. Points P'_1 and P'_2 are shifted along the surface normal from their actual locations P_1 and P_2 due to the uncertainty in the surface normal direction ($u_{\bar{n}}$). θ_1 and θ_2 are the horizontal angles with respect to the TLS coordinate system's x -axis. Note that x and x' are parallel to each other



5 Side view of sub-surfaces, the top one being vertically inclined at an angle ν (around the x -axis) between the surveying coordinate system's z -axis (z) and the object's coordinate system z -axis (Z). The uncertainties $u_{\bar{n}_1}$ and $u_{\bar{n}_2}$ are parallel to the surface's Y -axis. Points P'_1 and P'_2 are shifted along the surface normal from their actual locations P_1 and P_2 due to the uncertainty in the surface normal direction ($u_{\bar{n}}$), and φ_2 is a vertical angle measured from the horizontal direction. Note, that z and z' are parallel to each other

Downloaded by [85.29.230.26] at 00:48 11 August 2017

the xy -plane on the surface (cf. Fig. 4):

$$\omega = \tan^{-1} \frac{y_B - y_{P_2}}{x_B - x_{P_2}} \quad (9)$$

Note that the point B should preferably be located at the same height (along the z -component) as the survey point P_2 (Fig. 4, cf. also Fig. 2). For typical fabricated objects, only a single angle ω is needed to describe the plane-like orientation of the surface of the object, and thus it is sufficient to choose only one arbitrary point B on a particular surface (see Fig. 4). For more complex situations, the surface can be segmented into several sub-surfaces (e.g. Nuttens *et al.* 2014, Lahamy *et al.* 2016, Yang *et al.* 2016), and the direction with respect to the TLS coordinate system can be found for each sub-surface.

Surfaces can also be vertically inclined to an angle (ν) (Fig. 5). Hence, the inclination angle can be calculated, provided that the coordinates of two points P_2 and A (located either above or below the surface point) on a surface are known (cf. Figs. 4 and 5):

$$\nu = \tan^{-1} \frac{y_A - y_{P_2}}{z_A - z_{P_2}} \quad (10)$$

The surface normal vector \vec{n} is obtained from the cross product of two arbitrary vectors on the plane surface (e.g. vectors \vec{PA} and \vec{PB} in Fig. 2). The resulting normal vector (with components a, b, c) is orthogonal to the plane:

$$\vec{n} = (\vec{PA} \times \vec{PB}) = (a, b, c) \quad (11)$$

From this, the angle of incidence (α) can be calculated using well-known relations in linear algebra (cf. Fig. 2):

$$\alpha = \cos^{-1} \left(\frac{\vec{SP} \cdot \vec{n}}{|\vec{SP}| |\vec{n}|} \right) \quad (12)$$

where the vector \vec{SP} is calculated from the centre point (S) coordinates of the scanner and the coordinates of the survey point (P) of interest (see Fig. 2), $\vec{SP} \cdot \vec{n}$ is the

dot product of two vectors:

$$\vec{SP} \cdot \vec{n} = (x_P - x_S)a + (y_P - y_S)b + (z_P - z_S)c \quad (13)$$

The ANU for the general cases can be calculated by projecting CSU values onto the surface normal, cf. Fig. 6. For the projection, right triangles (see Fig. 6) can be formed using calculated CSU values (u_x, u_y and u_z) and the object's rotation angles ω and ν with respect to the TLS coordinate system (Fig. 6). The ANU component (either u_x, u_y, u_z cf. Fig. 6) is the hypotenuse of the right triangle formed. After all the CSU components have been projected (using trigonometric relations in the formed triangles) onto the surface normal, the total ANU is determined using the error propagation law of random variables (e.g. Bjerhammar 1973) as follows:

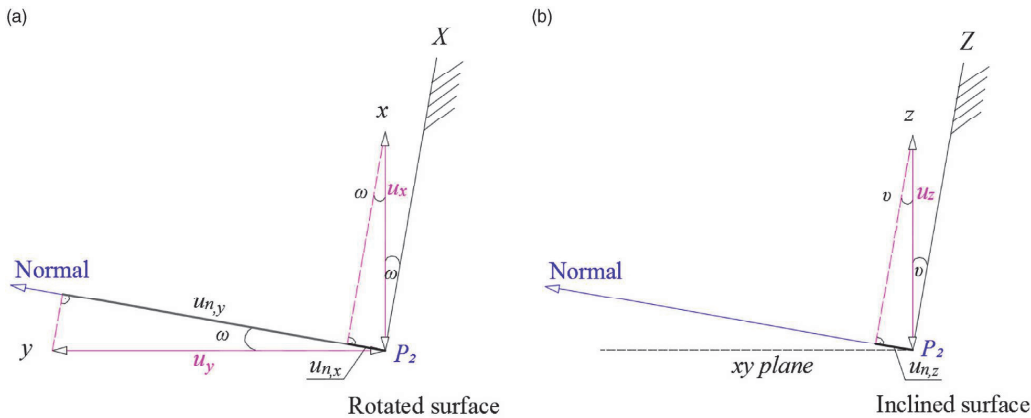
$$u_{\vec{n}} = [(\sin \omega u_x)^2 + (\cos \omega u_y)^2 + (\sin \nu u_z)^2]^{\frac{1}{2}} \quad (14)$$

Numerical verifications of ANU

This section verifies numerically the above-derived along-normal component of CSU. The results are also compared with those of previous empirical studies.

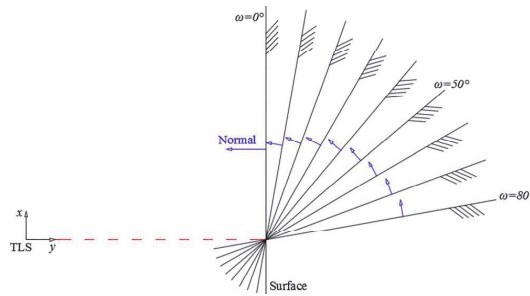
First, a vertical surface that is horizontally rotated from its initial direction (i.e. $\omega = 0^\circ$) is tested, as in empirical studies by Soudarissanane *et al.* (2009, 2011) and Soudarissanane (2016). In these studies, a PS type of TLS was located at a distance (20 m) from a surface which was rotated to different angles in increments of 10° within the interval $[0^\circ \leq \omega \leq 80^\circ]$, cf. Fig. 7.

Note that as the surface is rotated horizontally (in other words \vec{n} is dependent only on the components a and b , herewith $c = 0$ cf. equation (11)), both u_x and u_y have an effect on ANU (cf. equation (14)). The third component u_z , in this case, can be neglected since it describes uncertainty in the vertical direction. To follow the worst-case uncertainty scenario (cf. equation (8)), the TLS measurables θ and φ are taken to be 90° and 0° , respectively. Initially, at $\omega = 0^\circ$, the surface normal is parallel to u_x (cf. Fig. 7), and CSU values are calculated (by equations (5) and (6)) to be $u_x = 0.003$ m and $u_y = 0.012$ m, respectively. Note that



6 Geometric relations between CSU and the surface normal. a top view of relations between CSU and a surface that is horizontally rotated to an angle (ω). b Side view of the case when the surface is vertically inclined to an angle (ν). $u_{n,x}$, $u_{n,y}$ and $u_{n,z}$ are axial uncertainties projected onto the surface normal

Downloaded by [85.29.230.26] at 00:48 11 August 2017



7 Top view of a vertical surface which is horizontally rotated $[0^\circ \leq \omega \leq 80^\circ]$ by an angle ω in increments of 10° . The coordinate axis location coincides with the centre location of the TLS. The dashed line illustrates the laser beam from the scanner to the surface contact point (remains at a constant distance). The direction of the surface normal at different angles ω is shown by the arrows

the effect of $u_{\hat{x}}$ on the surface normal can be completely neglected at $\omega = 0^\circ$, as is uncertainty along the surface. In the contrasting case of $\omega = 90^\circ$, the ANU becomes equal to $u_{\hat{x}}$ only, as $\lim_{\omega \rightarrow 90^\circ} f(u_{\hat{n}}) \rightarrow u_{\hat{x}}$. For a gradually rotated (with respect to the initial direction, $\omega = 0^\circ$) surface, the numerical values of the ANU are calculated by equation (14) using the $u_{\hat{x}}$ and $u_{\hat{y}}$ components. The results are depicted in Fig. 8.

The results reveal that the ANU decrease gradually, as the angle ω increases. Notably, the numerical results at $\theta = 90^\circ$ and $\omega = 0^\circ$ (the y -axis is parallel to the surface normal) are influenced by u_{dist} only (Fig. 8, cf. equation (8)). The results can then be considered the worst-case scenario, since the ANU reaches maxima (cf. equation (8)). The u_{dist} influence dominates in the immediate neighbourhood of $\theta = 90^\circ$.

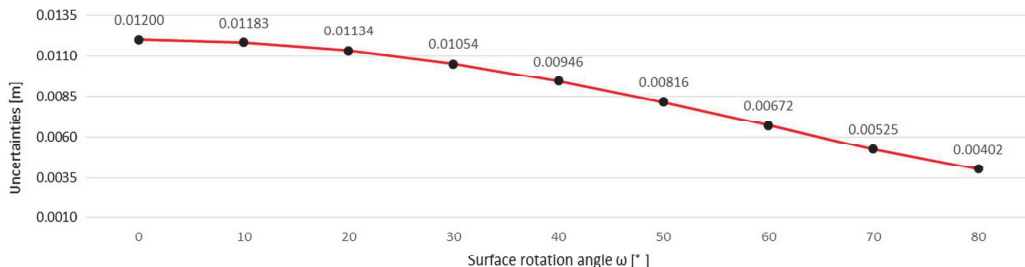
The achieved ANU values are compared to geometrical uncertainties, which are alternatively derived from the geometrical relations using the law of sines in conjunction with the measuring uncertainties u_{dist} and $u_{n,\text{angle}}$. The main aim of the exercise is to relate the angle of incidence to ANU. Derivation of the related quantities is omitted here; only the main numerical results are presented and compared with the results of previous empirical studies by Soudarissanane *et al.* (2009, 2011) and Soudarissanane (2016). It appears that the ANU is dependent on the cosine of the angle of incidence. This relation is also confirmed by the aforementioned studies. They scanned (using a PS scanner) a vertical surface, which was gradually rotated around the z -axis between 0° and 80° . For each 10° turn, the surface

was modelled from the TLS point cloud, and modelling residuals (i.e. deviations from the actual surface) were estimated. The residuals obtained describe the noise in the direction of the laser beam (results shown in Fig. 9). The goal of these empirical studies was to isolate the effect of the angle of incidence (α) from the surveying results.

The values estimated by Soudarissanane *et al.* (2011) are compared to the results in the present study in Fig. 9. The results indicate that uncertainties in the direction of the laser beam (uppermost line) have a steep increase at larger surface rotation angles (ω). The projected ANU ($u_{\hat{n}}$, second line) are identical to the results obtained by the theoretical equation (14) and depicted in Fig. 8. Thus, the ANU by equation (14) are verified also by the geometrical relations.

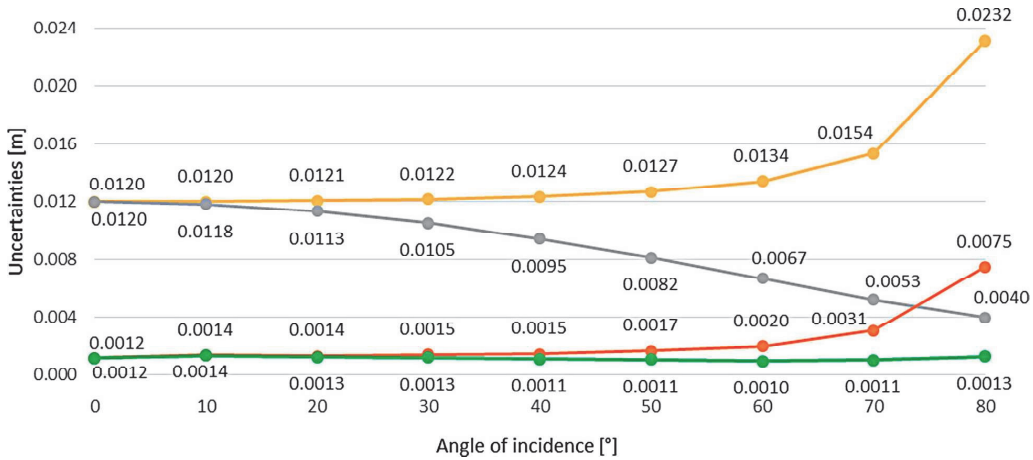
The differences between the Soudarissanane *et al.* (2011) empirically estimated ANU (Fig. 9 fourth line) and the theoretical ones derived in this study (equation (14), cf. Fig. 9 second line) increase with the increasing angle of incidence. This is due to the difference in the magnitudes of the empirically obtained and the theoretically determined value of uncertainty in the direction of the laser beam. Obviously, only a scaling factor (u_{dist} e.g. 0.012 m) is needed to make the two studies comparable to each other. This also supports that the manufacturers' specifications used in the present study could be somewhat too pessimistic.

Similarly to empirical studies (Soudarissanane *et al.* 2009, 2011, Soudarissanane 2016), the uncertainties obtained in the direction of the laser beam increase more sharply at larger angles of incidence. More accurate theoretical estimates can be obtained using individual



8 Results of the ANU of TLS survey points on a vertical surface, which is horizontally rotated by the angle ω ; the rotation interval is $[0^\circ, 80^\circ]$ with the increments of 10° . The distance from the TLS to the surface is 20 m. Units in metres

Downloaded by [85.29.230.26] at 00:48 11 August 2017



9 A comparison of ANU estimated by the present study and that of the Soudarissanane *et al.* (2011) empirical study. The uppermost line indicates uncertainties in the direction of the laser beam derived from the geometric relations; the second line indicates the ANU (u_n) derived using equation (14), also equal to the computed geometrical uncertainties; the third line indicates the (reconstructed) uncertainties in the direction of the laser beam estimated by Soudarissanane *et al.* (2011); and the fourth line indicates the (reconstructed) ANU estimated by Soudarissanane *et al.* (2011). The distance to the surface in all cases is 20 m

calibration results, and using these values, the ANU estimated using the proposed method (equation (14)) should be also more accurate.

To conclude, the proposed theoretical method for calculating ANU has been verified by comparing calculated uncertainties with the reported results of previous empirical studies and studying geometrical relations. Results show that the derived method can be used to obtain a realistic assessment of ANU and makes it possible to estimate uncertainties at the survey design stage before the actual survey. Results also suggest that the uncertainties provided by instrument manufacturers should be looked at more critically. Nevertheless, the metrological parameters provided by instrument manufactures are used in further computations to ensure consistency with earlier estimates. The following sections deal with examples of uncertainty estimations for engineering structures.

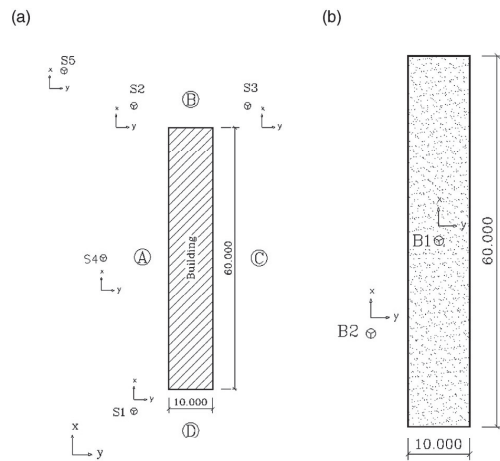
ANU at TLS surveys of engineering structures

The façades of a building and the lower side of a bridge deck were computer-simulated to investigate the behaviour the ANU at TLS surveys of engineering structures. Noise is then introduced in the data to simulate realistic survey data. These noise-contaminated data are then used for geometrical modelling to determine the influence of along-normal noise to the modelling outcome.

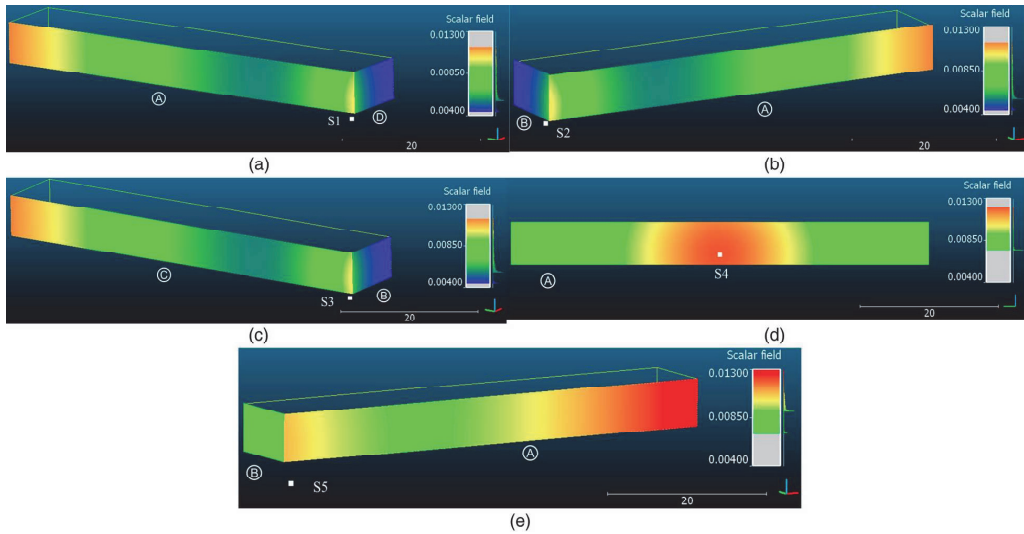
The simulated building has dimensions of $60 \times 10 \times 6$ m, representing thus a simple two-storey building (Fig. 10). The structure is covered with 85,400 points ($601 \times 61 + 100 \times 61 + 600 \times 61 + 99 \times 61$, the corner points and edges included) with a resolution of 0.10 m. The length and width of the bridge deck are 60 and 10 m, respectively, see Fig. 10b. The simulated bridge surface thus consists of 60,701 survey points. In both cases, a point density of 0.10 m (i.e. less dense than in realistic

TLS surveys) was chosen for demonstrative purposes and is considered to be sufficient for a description and further analysis of the spatial distribution of expected uncertainties. The object's axes are parallel to the TLS coordinate axes, allowing us to deal with the influences of maximum ANU values for the surveyed surfaces (cf. section 'A special case').

For the building survey, the scanning stations were chosen at the corners of the building so that two sides would be covered by one station (Fig. 10a), a realistic surveying scenario. Two additional scanning stations (S4 and S5, cf. Fig 10) were added to obtain data from a potentially the



10 Top view of the locations of the scanning stations (S1, S2, S3, S4 and S5) for the building survey a and the bridge deck (B1 and B2) survey b. Ⓐ, Ⓑ, Ⓒ and Ⓓ in a denote the sides of the building. Units in metres



11 Side views of spatial distributions of ANU along the building façades for scanning stations S1, S2, S3, S4 and S5. The height of the vertical wall corresponds to 6 m. The ANU scales are at right-hand side. Note that lower- and uppermost parts in the fixed-value scale of each sub-plot denote the non-occurring ANU values at particular surveying cases. Units in metres

most suitable scanning location (S4) and a likely unsuitable location (S5) with respect to the side \odot .

The simulated bridge deck data consist of two sets of point clouds acquired from two different scanner locations. The scanning stations were located: (i) under the bridge at the centre of the bridge deck (station B1); (ii) alongside the bridge deck at a horizontal distance of 6.0 m away from the deck (station B2, in practice, it would be riverbank), cf. Fig. 10b. These locations were selected according to common surveying practices, e.g. Zogg and Ingensand (2008), Riveiro *et al.* (2011), de Asís López *et al.* (2014) and Mill *et al.* (2015). Figure 10b illustrates the case when it is not possible to place a scanner under the bridge, e.g. when there is water or risk of collapse (e.g. during the bridge load tests). In this case, the scanner is shifted away from the deck, as in, e.g. Mill *et al.* (2015). In no obstacles case, the scanner can be located directly under the bridge deck (Fig. 10b). In both cases, the vertical distance as of 4.3 m from the scanner centre to the bridge’s lower surface was adopted.

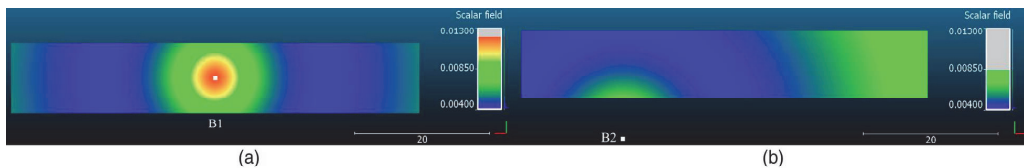
Spatial distribution and range of ANU

The results in Figs. 11 and 12 illustrate the ANU $u_{\hat{x}}$, $u_{\hat{y}}$ and $u_{\hat{z}}$ obtained using equations (5), (6) and (7). Recall

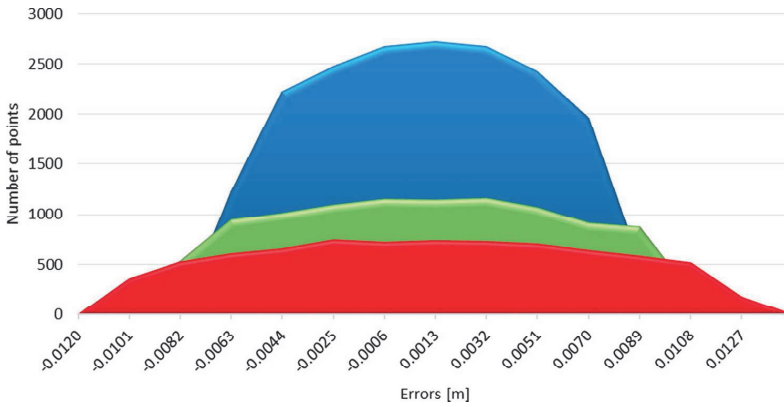
that in this particular case, the TLS axes are strictly parallel to the object’s axes (cf. Fig. 10), which justifies the usage of equations (5), (6) and (7) for calculating the ANU. The calculated ANU values have a confidence level of 99.7% derived from the uncertainties provided by the instrument manufacturer (cf. section ‘A special case’).

In general, as shown in the previous sections, the worst ANU are obtained when the horizontal scanning angle θ is either 0° or 90° (cf. equation (8)) and scanning is carried out in a direction perpendicular to the surface (the region closest to station S4 in Fig. 11d). Recall that this is due to the behaviour of $\sin(\theta)$ and $\cos(\theta)$, as the value of θ decreases from 90° to 0° in equation (8) (cf. the subsection ‘A special case’).

The largest ANU values of the \odot side are associated with station S5 (Fig. 11e), due to its remoteness from the object. The influence of both vertical and horizontal angular uncertainty on ANU increases, as the distances increase (the max. distance reaches approx. 75 m at the right-hand end of the A side; cf. also Fig. 3). The spatial distribution and range of calculated ANU values for the building façades at symmetrically located (with respect to the object) stations S1, S2 and S3 (Fig. 11a–c) are almost identical, with only some marginal differences. Note that the uniform fixed-value



12 Top view of spatial distribution of ANU estimates along the bridge deck surface for scanning stations B1 and B2. Note that the images are rotated 90° . The location of the stations is denoted by white dots. Note that uppermost part in the fixed-value scale of each sub-plot denotes the non-occurring ANU values at particular surveying cases. Units in metres



13 Distribution of the measurement noise obtained from scanning station S1 for side ③. The top segment indicates the noise interval for group I, which contains the majority of points (18,873 points from a total of 36,661 points, yielding RMS = 0.00409 m); the middle slab indicates the noise interval for the group II (RMS = 0.00516 m); and the bottom slab indicates the noise interval for the group III, which contained the minority of points (7708 points, RMS = 0.00619 m). Note that the RMS values are correlated with results in Fig. 11a.

scale is applied, for Figs. 11 and 12, to make the sub-plots comparable to each other.

In Fig. 11, the regions of the surfaces closest to the stations S1, S2, S3 and S4 (in *a*, *b*, *c* and *d*) illustrate the dominant influence of u_{dist} . Similar region in the case of station S5 occurs at the right-hand ending of side ③ due to the increasing influence of the errors in measured distance (cf. Fig. 11e). However, the ANU magnitudes are distributed more uniformly across the entire surface. In general, for remote stations, the less variation in ANU values is expected.

The shorter sides (④ and ⑤) of the building show very little variation in ANU, cf. Fig. 12a–c and e. This is due to the θ variation less than $\pm 20^\circ$ (whereas an average α is 68°) and thus ANU does not vary significantly. Note that θ does not reach 90° at S1, S2, S3 and S5. Thus, with such a measurement set-up, the uncertainties obtained for the shorter sides are more accurate than those for the long sides.

For the bridge surfaces, there is a clear distinction between the uncertainties obtained from different locations (Fig. 12a and b). The largest ANU, due to dominating u_{dist} , as expected, are obtained for the centre of the bridge deck from station B1 (i.e. φ is 90° , thus $\alpha = 0^\circ$). Smaller ANU estimates were obtained from station B2 at the side of the bridge (Fig. 12b).

Calculated ANU values are relatively large (Figs. 11 and 12), likely due to the apparently pessimistic metrological values provided, u_{dist} in particular, for the instruments. Nevertheless, they provide a general insight into the nature of the predictable outcome.

Note that the positive ANU values determined by equation (14) do not fully represent actual measuring uncertainties, which, in general, are random, thus having both negative and positive values. For determining the influence of ANU for geometric modelling of surfaces, the data points were contaminated with the random measurement noise.

Random measurement noise

The ANU intervals for each surface were defined by dividing the difference between the maximum and the

minimum ANU value by three (equation (15)).

$$(ANU_{\text{max}} - ANU_{\text{min}})/3 = ANU_{ca} \quad (15)$$

Then the ANU intervals were defined as follows:

$$[-(ANU_{\text{min}} + ANU_{ca}), (ANU_{\text{min}} + ANU_{ca})]_{\text{I}} \quad (16)$$

$$[-(ANU_{\text{min}} + 2ANU_{ca}), (ANU_{\text{min}} + 2ANU_{ca})]_{\text{II}} \quad (17)$$

$$[-(ANU_{\text{min}} + 3ANU_{ca}), (ANU_{\text{min}} + 3ANU_{ca})]_{\text{III}} \quad (18)$$

where sub-indexes I, II and III denote different noise groups with corresponding upper- and lowermost (a positive and negative value) limits for each group. Three intervals are sufficient for generalising influences of along-normal noise to surface modelling. Note that these major groups were determined to comply the range and spatial distribution of the ANU, and are also associated with the prevailing three ANU regions in Figs. 11 and 12.

Thereafter, the normal inverse cumulative distribution function was used for generating random measurement noise for each noise group (I, II and III). An individual noise value was generated for each individual data point.

The noise introduced follows a normal distribution ($\varepsilon \sim N(0,1)$) (cf. Fig. 13) with the near-zero mean noise value (see Table 1):

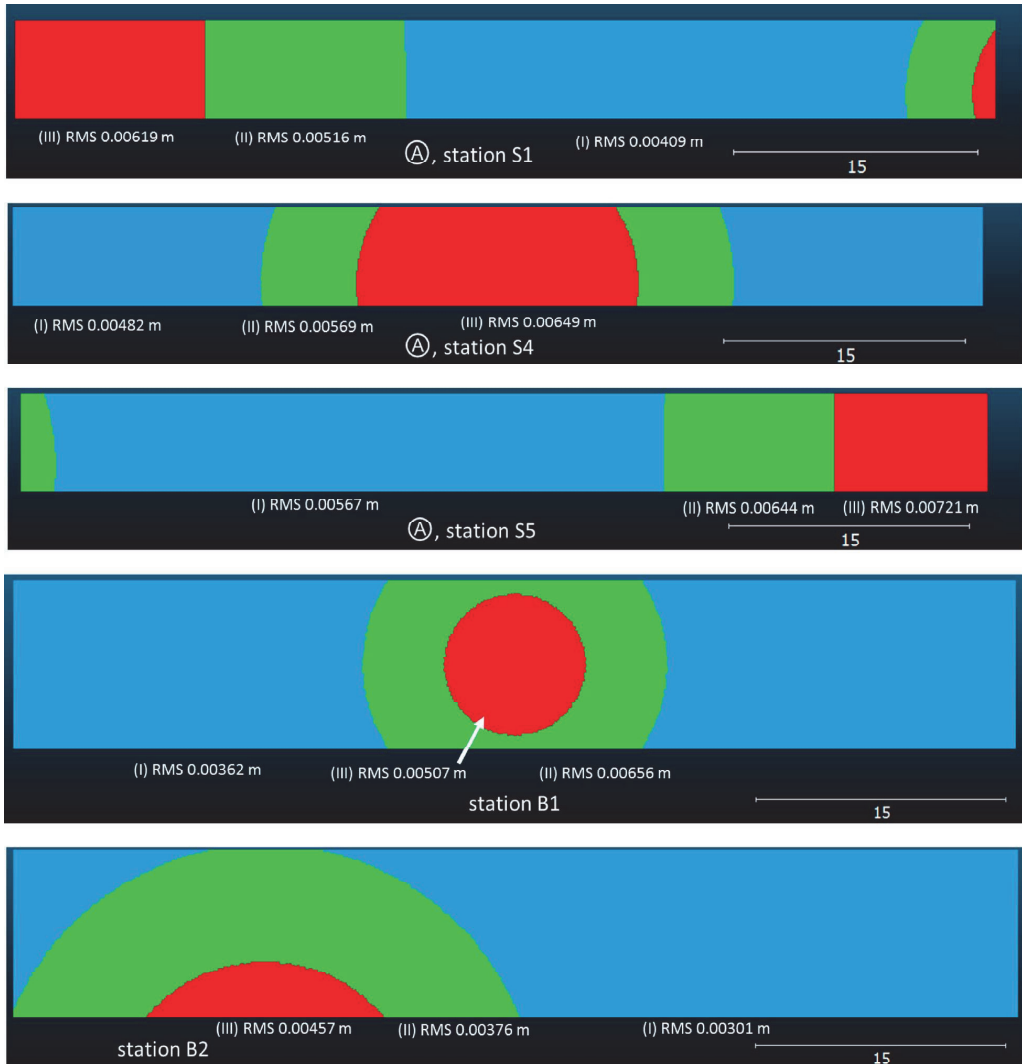
$$\bar{\varepsilon} = \frac{\sum_{i=1}^n \varepsilon_i}{n} \quad (19)$$

where ε is the generated noise value at an *i*-th data point and $i = 1, \dots, n$, where *n* is the total number of data points.

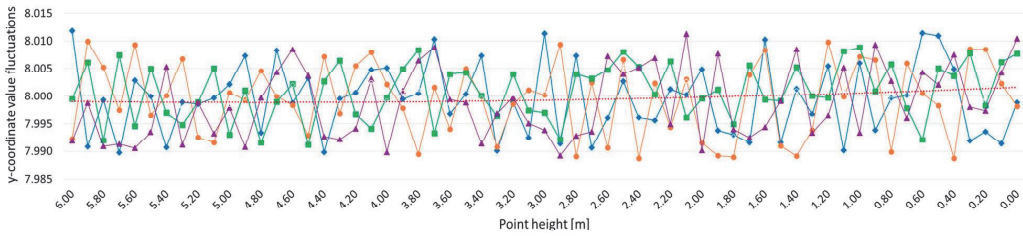
Table 1 Comparison statistics for the façade side ④ and the bridge deck

Statistics	Station S1	Station S2	Station S1 and S2 with overlap	Station S4	Station S5	Bridge deck, Station B1	Bridge deck, Station B2
Number of points	36,661	36,661	44,079	36,661	36,661	60,701	60,701
$\bar{\epsilon}$	0.02	0.04	0.04	0.00	0.02	0.01	0.00
$\bar{\Delta}$	0.02	0.04	0.04	0.00	0.02	0.01	0.00
$ \Delta_{\max} $	0.2	0.2	0.2	0.2	0.4	0.1	0.1
STDEV	0.08	0.05	0.08	0.06	0.09	0.02	0.03

Units are in millimetres.



14 Spatial distribution of noise groups (I, II and III) across side ④ of the building façade and the bridge deck surface, from stations S1, S4, S5, B1 and B2. Note correlation with Figs. 11 and 12 as well



15 Distribution of noise-contaminated survey points from stations S1 (dot markers), S2 (triangle markers), S4 (square markers) and S5 (rhombus markers) for the north-west corner of the façade; the dashed line is the trendline obtained from averaging the y-coordinate values obtained from the four stations with a mean discrepancy of 0.4 mm. The maximum deviation from the actual coordinates is 12 mm for data from station S2. The left- and right-hand sides of the figure denote the top and the bottom corner of the building, respectively

The root mean square (RMS) of noise in each group is estimated as

$$RMS = \sqrt{\frac{\sum_{i=1}^n \varepsilon_i^2}{n}} \quad (20)$$

The spatial distribution across side @ of the building façade of the three noise groups is illustrated for scanning stations S1, S4, S5, B1 and B2 in Fig. 14. Note that the distribution of noise groups for stations S2 and S3 for sides @ and © is mirroring the distribution of noise groups for station S1. The distribution of noise groups is similar to the distribution of uncertainties in Figs. 11 and 12, where generally the data with the largest noise are at both the closest and remotest parts of the surface. The same observation applies to noise distribution from other scanning stations as well.

Figure 15 illustrates the distribution of the noise-contaminated survey points (i.e. along-normal in the y-direction, cf. Fig 10) obtained for the north-west juncture of sides @ and © of the building. The figure shows the balanced distribution of points around the true y-coordinate value of exactly 8 m. In spite of a few large deviations from the true value, the general trendline determined by averaging the y-coordinate values obtained from stations S1, S2, S4 and S5 practically coincides with the correct location of the object’s corner (Fig. 15). This is the expected outcome for the geometrical modelling.

These noisy data need to be geometrically modelled to investigate the influence of along-normal noise on surface modelling.

Geometrical modelling of erroneous data

In general, surface modelling can be carried out using both non-iterative and iterative methods. Non-iterative fitting is a method whereby the surfaces are described using only a few parameters, allowing the fitting of simple geometrical shapes using robust non-iterative methods that detect clusters in parameter space (e.g. Lindenbergh *et al.* 2009, Erdélyi *et al.* 2014). Iterative fitting uses an iterative algorithm to find the best-fit surface with constrained least squares using the discrepancies of the scanned points from the surface (e.g. Holst *et al.* 2014c, Wang *et al.* 2015).

Considering the nature of TLS measurements, the selection of appropriate data processing methods is

crucial, since different methods provide somewhat different results.

For the purposes of investigating the influence of along-normal noise on the modelling, an iterative method can be expected to provide the most adequate results and is used in practice. Since the maximum of the introduced noise across different parts of a surface differ, geometric modelling is expected to result in a slightly curvilinear surface (cf. Fig. 14). Therefore, instead of using a simple plane model for investigating the influence of ANU to modelling, the geometric modelling is carried out using an iterative method that implements a quadratic polynomial function (equation (21)). This method is widely used for geometrically modelling of TLS data, e.g. Park *et al.* (2007), Holst *et al.* (2014b), Yang *et al.* (2016):

$$z = A + Bx + Cy + Dx^2 + Exy + Fy^2 \quad (21)$$

where A, B, C, E and F are coefficients.

For geometric modelling, an open-source software CloudCompare (Lague *et al.* 2013) was used. The result of fitting a point cloud data to the quadratic polynomial function is represented as a standard triangular mesh. As an indication of the quality of fitting of the erroneous data to the quadratic polynomial function, the *RMS* (cf. equation (20)) of the fitting is compared to the *RMS* of the introduced noise.

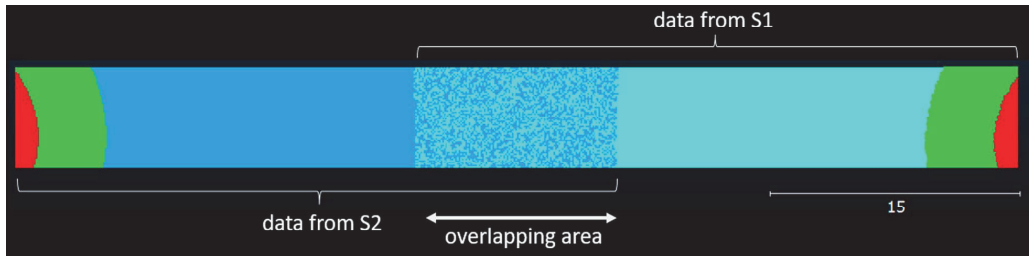
The position of each true data point with respect to the modelled (i.e. erroneous) surface is identified and the cloud to surface distance is estimated. The results of the comparisons are evaluated using the mean discrepancy (equation (19)) and the standard deviation (STDEV) between the modelled surface and the true data:

$$STDEV = \sqrt{\frac{\sum_{i=1}^n (\Delta_i - \bar{\Delta})^2}{n}} \quad (22)$$

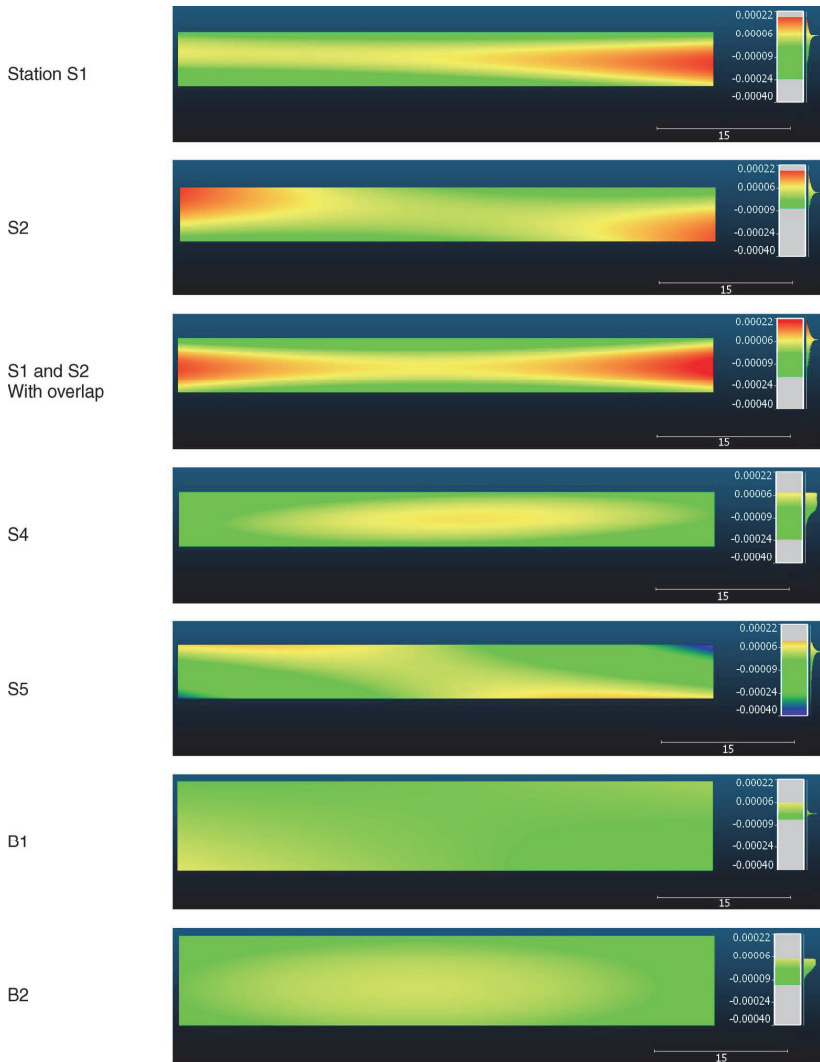
where Δ_i is the discrepancy value at an i -th data point and $i = 1, \dots, n$.

Modelling results

Since the simulated data for side @ of the building façade were acquired from four different scanning locations (S1, S2, S4 and S5), then this side is considered most suitable for detecting the influence of simulated along-normal noise on the modelling. The data for sides @, © and © due to analogous distribution (thus yielding similar



16 Noise-contaminated data from stations S2 (left) and S1 (right). The noise groups are denoted as follows: group III (second from the edges), group II (edges) and group I (central part). The overlapping data (S1 + S2) area in the centre spans approx. 12 m



17 The range and spatial distribution of discrepancies between the modelled surface and the true point clouds. The coloured discrepancy scales and obliquely oriented histograms of discrepancies are on right-hand side. Note that lower- and upper-most parts in the fixed-value scale of each sub-plot denotes the non-occurring discrepancy values at particular surveying cases. Units in metres

results) are not considered. Data selected from stations S1 and S2, including an approx. 12 m overlap (in the middle) are also considered separately (Fig. 16).

In addition to the façade data, data from stations B1 and B2, representing a bridge deck, are also modelled.

The results of the comparison of the geometrically modelled erroneous data and the true point clouds are shown in Table 1.

Regardless of the small magnitudes in the reported modelling results in Table 1, some noise-induced distortions in the shape of the actual surface occur (see Fig. 17). Note that the values of the mean discrepancies ($\bar{\Delta}$) coincide with the mean values of the introduced noise ($\bar{\epsilon}$, cf. Table 1). Owing to non-zero mean of the noise at some locations, systematic effects in the modelling results occur.

Figure 17 illustrates the distribution of the obtained discrepancies between the modelled surface and the true data. The obtained discrepancies are at a submillimetre level for all cases, indicating a good surface fit.

In the case of the façade surface modelling, the largest mean discrepancy, the maximum absolute value of discrepancy ($|\Delta_{\max}|$) and the standard deviation (Table 1, cf. Fig. 17) were obtained using the overlapped data from stations S1 and S2. Such results occur likely because the uncertainties along the surface \otimes vary considerably between the middle part and the two ends of the surface (cf. Fig. 16). Better results were, however, expected using these data since the larger portion of the surface (approx. 83%) was covered by the most accurate noise group (Fig. 16).

Also somewhat worse results, compared to results for other façade scanning stations, were obtained for station S5 (see Table 1). Recall that station S5 is positioned at the most remote location from the north-west corner of the façade of the building (cf. Fig. 10). Thus, measurement noise is larger than it is for the other stations (cf. Fig. 14), yielding also the largest residuals of the geometrical modelling (Table 1).

Despite the symmetrical relations in-between the locations of the scanning stations S1 and S2, the modelling results are not identical and differ somewhat (Fig. 17). The probable cause for this lies in the difference between the mean values of the introduced noise (Table 1). Note that the magnitude of the difference is only marginal.

The modelling results for station S4 show the smallest mean discrepancy (Table 1, cf. Fig. 17) in spite of somewhat larger ANU values compared to other stations (cf. Fig. 11).

In the case of horizontal surfaces, there are only marginal differences between the mean discrepancies and the standard deviations for data from stations B1 and B2 (Table 1, cf. Fig. 17). However, larger differences are expected due to the differences in the calculated ANU for the two stations (cf. Fig. 12) and thus differences in the introduced noise (cf. Fig. 14). Recall that noise values for data from station B2 were smaller than those for data from B1.

In conclusion, the obtained mean discrepancies, the maximum absolute value of discrepancy and the standard deviations (cf. Table 1) indicate good surface fitting results. This is likely because noise in the survey data does not include significant systematic error and has a normal distribution with a mean value of close to zero

(Table 1.). In spite of the larger ANU values for scanning stations S4 and B1 (cf. Figs. 11 and 12), they yielded the best modelling results (cf. Table 1). The simulated along-normal noise did not produce significant effects on geometric modelling of surfaces. However, if the data in the present study were complemented with systematic noise (not within the scope of the present study), the results may have possibly been different in terms of noise, and thus the modelling results would have been different.

Optimal scanning locations

One goal of the study was to identify optimal scanning locations, considering the simulated realistic surveying scenarios (cf. Fig. 10). The optimality was defined according to two criteria: the magnitude and the distribution of the calculated ANU values (cf. Figs. 11 and 12).

For the building façades, the ANU from stations S4 and S5 is clearly larger than that for data from stations S1, S2, and S3, while ANU for data from stations S1, S2, and S3 are almost identical. Note that data from station S4 cover only one side of the building façade, while other stations cover two sides. For this study, the station S5 is deliberately located relatively far from the north-west corner of the building façade (approx. 27 m), and as expected, it produced the largest ANU values. Larger distances are also generally more likely to yield systematic error, e.g. due to an increase in the backscatter signal-to-noise ratio (Kersten *et al.* 2009). However, station S5 also provided a more even distribution of ANU values over a larger part of the façade surface (cf. Fig. 11e).

In the case of the bridge deck surface, ANU from station B1 (located under the deck surface) is larger than that for data from B2 (cf. Fig. 12).

In general, maximum ANU values are expected when surveying is carried out in a direction perpendicular to the surface (cf. the worst-case scenario in the subsection 'A special case'). In this case, distance measuring accuracy has the largest influence on uncertainty.

To conclude, based on the analysis of different simulated scenarios (and the given metrological parameters), optimal scanning locations were determined for (i) the vertical surfaces of a building façade, and (ii) the horizontal surfaces of a bridge deck. In the first case, they were found to be locations closest (less than 10 m) to the corners of the buildings (stations S1, S2 and S3), while approx. 85% of the ANU values for data for the longer sides \otimes and \odot obtained from these stations were on a magnitude of less than 1 cm, whereas this ratio was only 67 and 50% for stations S4 and S5, respectively (cf. Fig. 11). For the short sides of the building, the ANU values for stations S1, S2 and S3 were all on a magnitude of less than 0.7 cm. In the second case, the optimal location was found to be at the side of the bridge deck (station B2), since all the ANU values obtained for data from this station were on a magnitude of less than 1 cm (cf. Fig. 12). Thus, in the case of bridge surveys, it is recommended to place the TLS station to the side of the bridge.

The results of the present study indicate that scanning in the perpendicular direction to the surface (α being close to 0°) should be avoided. As the surveying distance also has a significant impact on the magnitude of the

ANU, the optimal scanning distance at which ANU can be reduced is between 10 and 25 m (cf. results in Fig. 3, which demonstrates that the smallest uncertainties occur within this interval, note that beyond 25 m the uncertainties start to increase). The influence of ANU on geometric modelling is further reduced when there are no systematic errors present. The results of the present study indicate that the presence of even a small amount of systematic error has an influence on the geometric modelling.

Conclusions

As TLS is often used for various construction surveys, this study aims at serving a reference when designing a TLS survey. The study provides theoretical insights into the magnitude of the effect of ANU arising when surveying different types of engineering structures. It is shown that by judiciously selecting the location of a scanner in a survey site, it is possible to reduce noise in the surface normal direction. This is mainly because different scanning geometry yields different scanning parameters (distance, horizontal and vertical angle) and therefore can generate less or more noise.

In the present study, a method for estimating ANU is introduced and verified numerically. Expected uncertainties in different scenarios are investigated. The proposed method is verified using the results of previous empirical TLS case studies and geometric relations.

The simulated survey data were contaminated with the random noise. Thereafter, the data were geometrically modelled using an iterative modelling method. Owing to the normally distributed random noise, the modelling results indicated good surface fittings. Such results were obtained most likely because that noise in the survey data did not include significant systematic error and had a normal distribution with a mean value of close to zero (max. 0.04 mm). If systematic error had also been considered in the present study, results may have possibly been different.

The optimal scanning locations were determined to be locations closest (less than 10 m) to the corners of the simulated building (stations S1, S2 and S3) and the location at the side of the bridge deck (station B2). It is shown that maximum ANU values are expected when surveying is carried out in a direction perpendicular to the surface. It is also shown that optimal scanning distance is in the range of 10–25 m.

Future studies should more closely investigate the dependence of results of different TLS signal processing methods and also applicability of CSU equations considering also systematic error in TLS surveys.

Acknowledgements

The authors thank the two anonymous reviewers for their valuable comments.

Funding

The study was supported by the Estonian Environmental Technology R&D Program KESTA, research project ERMAS, AR12052.

ORCID

Tarvo Mill  <http://orcid.org/0000-0002-7098-088X>

References

- Alkhatib, H., Neumann, I., and Kutterer, H., 2009. Evaluating uncertainties of laser scanner measurements by using a joint Monte Carlo and Fuzzy approach. *In: XIX IMEKO world congress fundamental and applied metrology*, 06–11 September 2009. Lisbon, Portugal: IMEKO, 2394–2399.
- Argüelles-Fraga, R., et al., 2013. Measurement planning for circular cross-section tunnels using terrestrial laser scanning. *Automation in construction*, 31, 1–9.
- Bjerrhammar, A., 1973. *Theory of errors and generalized matrix inverses*. Amsterdam: Elsevier Science Ltd.
- Borah, D. K. and Voelz, D. G., 2007. Estimation of laser beam pointing parameters in the presence of atmospheric turbulence. *Applied optics*, 46 (23), 6010–6018.
- Chen, X., et al., 2016. An average error-ellipsoid model for evaluating TLS point-cloud accuracy. *The photogrammetric record*, 31, 71–87.
- Chow, J., Lichti, D., and Teskey, W., 2012. Accuracy assessment of the FARO Focus3D and Leica HDS6100 panoramic type terrestrial laser scanners through point-based and plane-based user self-calibration. *In: FIG working week 2012*, 6–10 May 2012. Rome, Italy: FIG, 1–15.
- Cuartero, A., et al., 2010. Error analysis of terrestrial laser scanning data by means of spherical statistics and 3D graphs. *Sensors*, 10, 10128–10145.
- Erdélyi, J., et al., 2014. Deformation monitoring of a parabolic roof structure using TLS. *In: INGEO 2014*, 3–4 April 2014. Prague, Czech Republic: Slovak University of Technology, 75–80.
- González-Aguilera, D., Gómez-Lahoz, J., and Sánchez, J., 2008. A new approach for structural monitoring of large dams with a three-dimensional laser scanner. *Sensors*, 8 (9), 5866–5883.
- Gottwald, R., 2008. Field procedures for testing terrestrial laser scanners (TLS) – a contribution to a future ISO Standard. *In: FIG working week 2008*, 14–19 June 2008. Stockholm, Sweden: FIG, 1–14.
- Gruen, A. and Akca, D., 2005. Least squares 3D surface and curve matching. *Journal of photogrammetry and remote sensing*, 59, 151–174.
- Holst, C. and Kuhlmann, H., 2014. Aiming at self-calibration of terrestrial laser scanners using only one single object and one single scan. *Journal of applied geodesy*, 8 (4), 295–310.
- Holst, C. and Kuhlmann, H., 2016. Challenges and present fields of action at laser scanner based deformation analyses. *In: 3rd joint international symposium on deformation monitoring*, 03 March–04 April 2016. Vienna, Austria: FIG, 1–9.
- Holst, C., Artz, T., and Kuhlmann, H., 2014a. Biased and unbiased estimates based on laser scans of surfaces with unknown deformations. *Journal of applied geodesy*, 8 (3), 169–184.
- Holst, C., Burghof, M., and Kuhlmann, H., 2014b. Modeling the beam deflection of a Gantry Crane under load. *Journal of surveying engineering*, 140 (1), 52–59.
- Holst, C., et al., 2014c. Improved area-based deformation analysis of a radio telescope's main reflector based on terrestrial laser scanning. *Journal of applied geodesy*, 9 (1), 1–14.
- JCGM 100:2008. *Evaluation of measurement data – guide to the expression of uncertainty in measurement (GUM)*. Sèvres: Bureau International des Poids et Mesures.
- Kaasalainen, S., et al., 2009. Radiometric calibration of terrestrial laser scanners with external reference targets. *Remote sensing*, 1, 144–158.
- Kersten, T. P., Sternberg, H., and Mechelke, K., 2005. Investigations into the accuracy behaviour of the terrestrial laser scanning system Mensi GS100. *In: Optical 3-D measurement techniques VII*, 3–5 October. Vienna, Austria: FIG, 122–131.
- Kersten, T. P., et al., 2009. Methods for geometric accuracy investigations of terrestrial laser scanning systems. *Photogrammetrie – Fernerkundung – geoinformation*, 9 (4), 301–315.
- Koch, K.-R., 2008. Determining uncertainties of correlated measurements by Monte Carlo simulations applied to laser scanning. *Journal of applied geodesy* 2 (3), 139–147.
- Lague, D., Brodu, N., and Leroux, L., 2013. Accurate 3D comparison of complex topography with terrestrial laser scanner: application to the Rangitikei canyon (N-Z). *ISPRS journal of photogrammetry and remote sensing*, 82, 10–26.
- Lahamy, H., et al., 2016. Measurement of deflection in concrete beams during fatigue loading test using the Microsoft Kinect 2.0. *In: 3rd joint international symposium on deformation monitoring*, 03 March–04 April 2016. Vienna, Austria: FIG, 1–7.

- Lichti, D. D., 2007. Error modelling, calibration and analysis of an AM-CW terrestrial laser scanner system. *ISPRS journal of photogrammetry and remote sensing*, 61 (5), 307–324.
- Lichti, D. D., 2010. Terrestrial laser scanner self-calibration: correlation sources and their mitigation. *ISPRS journal of photogrammetry and remote sensing*, 65 (1), 93–102.
- Lindenbergh, R., et al., 2009. Structural monitoring of tunnels using terrestrial laser scanning. *Reports on geodesy*, 2 (87), 231–239.
- de Asis López, F., et al., 2014. Point cloud comparison under uncertainty. Application to beam bridge measurement with terrestrial laser scanning. *Measurement*, 51, 259–264.
- Mao, Q., et al., 2015. A least squares collocation method for accuracy improvement of mobile LiDAR systems. *Remote sensing*, 7 (6), 7402–7424.
- Mill, T., et al., 2014. Determining ranges and spatial distribution of road frost heave by terrestrial laser scanning. *The baltic journal of road and bridge engineering*, 9 (3), 227–236.
- Mill, T., et al., 2015. Geodetic monitoring of bridge deformations occurring during static load testing. *The baltic journal of road and bridge engineering*, 10 (1), 17–27.
- Niemeier, W. and Tengen, D., 2016. Uncertainty assessment in geodetic network adjustment by combining GUM and MC. In: *3rd joint international symposium on deformation monitoring*, 03 March–04 April 2016. Vienna, Austria: FIG, 1–11.
- Nuttens, T., et al., 2014. Methodology for the ovalization monitoring of newly built circular train tunnels based on laser scanning: Liefkenshoek Rail Link (Belgium). *Automation in construction*, 43, 1–9.
- Park, H. S., et al., 2007. A new approach for health monitoring of structures: terrestrial laser scanning. *Computer-aided civil and infrastructure engineering*, 22 (1), 19–30.
- Pejić, M., 2013. Design and optimisation of laser scanning for tunnels geometry inspection. *Tunnelling and underground space technology*, 37, 199–206.
- Pesci, A. and Teza, G., 2008. Terrestrial laser scanner and retro-reflective targets: an experiment for anomalous effects investigation. *International journal of remote sensing*, 29 (19), 5749–5765.
- Pesci, A., et al., 2013. A laser scanning-based method for fast estimation of seismic-induced building deformations. *ISPRS journal of photogrammetry and remote sensing*, 79, 185–198.
- Pfeifer, N., et al., 2007. Investigating terrestrial laser scanning intensity data quality and functional relations. In: *Optical 3-D measurement techniques VIII*, 9–13 July. Zurich, Switzerland: ISPRS, 328–337.
- Reshetyuk, Y., 2009. Self-calibration and direct georeferencing in terrestrial. (PhD). KTH Royal Institute of Technology.
- Riveiro, B., et al., 2011. Terrestrial laser scanning and limit analysis of masonry arch bridges. *Construction and building materials*, 25 (4), 1726–1735.
- Roca-Pardiñas, J., et al., 2014. Analysis of the influence of range and angle of incidence of terrestrial laser scanning measurements on tunnel inspection. *Tunnelling and underground space technology*, 43, 133–139.
- Soudarissanane, S., 2016. The geometry of terrestrial laser scanning: identification of errors, modeling and mitigation of scanning geometry. (PhD). Delft University of Technology.
- Soudarissanane, S., et al., 2009. Incidence angle influence on the quality of terrestrial laser scanning points. In: *ISPRS workshop "laser scanning 2009"*, 1–2 September 2009. Paris, France: ISPRS 183–188.
- Soudarissanane, S., et al., 2011. Scanning geometry: influencing factor on the quality of terrestrial laser scanning points. *ISPRS journal of photogrammetry and remote sensing*, 66 (4), 389–399.
- Tsakiri, M., Pagounis, V., and Arabatzi, O., 2015. Evaluation of a pulsed terrestrial laser scanner based on ISO standards. *Surface topography: metrology and properties*, 3 (1), 1–9.
- Wang, J., Kutterer, H., and Fang, X., 2015. External error modelling with combined model in terrestrial laser scanning. *Survey review*, 47 (346), 40–50.
- Xuan, W., et al., 2016. Determining the deformation monitorable indicator. *Journal of the indian society of remote sensing*, 45 (1), 1–9.
- Yang, H., et al., 2016. *Terrestrial laser scanning technology for deformation monitoring and surface modeling of arch structures* [Online]. Composite Structures, in press, corrected proof, 21 October 2016. Available from: <http://sciencedirect.com> [Accessed 30 January 2017].
- Zhengchun, D., Zhaoyong, W., and Jianguo, Y., 2016. Point cloud uncertainty analysis for laser radar measurement system based on error ellipsoid model. *Optics and lasers in engineering*, 79, 78–84.
- Zogg, H.-M., Ingensand, H. 2008. Terrestrial laser scanning for deformation monitoring – load tests on the Felsenau viaduct (CH). In: *XXI ISPRS congress*, 3–11 July 2008. Beijing, China: ISPRS, 555–562.

Mill, T., Ellmann, A., Kiisa, M., Idnurm, J., Idnurm, S., Horemuz, M. and Aavik, A. (2015). Geodetic monitoring of bridge deformations occurring during static load testing. *The Baltic Journal of Road and Bridge Engineering*, 10(1), 17–27.



GEODETIC MONITORING OF BRIDGE DEFORMATIONS OCCURRING DURING STATIC LOAD TESTING

Tarvo Mill¹✉, Artu Ellmann², Martti Kiisa³, Juhan Idnurm⁴, Siim Idnurm⁵,
Milan Horemuz⁶, Andrus Aavik⁷

^{1, 2, 4, 5, 7}Dept of Road Engineering, Tallinn University of Technology, Ehitajate tee 5, 19086 Tallinn, Estonia

³Faculty of Construction, Tallinn University of Applied Sciences, Pärnu mnt 62, 10135 Tallinn, Estonia

⁶Dept of Geodesy and Geoinformatics, Royal Institute of Technology, Drottning Kristinas väg 30,
10044 Stockholm, Sweden

E-mails: ¹tarvo@tktk.ee; ²artu.ellmann@ttu.ee; ³martti.kiisa@tktk.ee; ⁴juhan.idnurm@ttu.ee;
⁵siim.idnurm@ttu.ee; ⁶milan.horemuz@abe.kth.se; ⁷andrus.aavik@ttu.ee

Abstract. Terrestrial laser scanning technology has developed rapidly in recent years and has been used in various applications but mainly in the surveying of different buildings and historical monuments. The use for terrestrial laser scanning data for deformation monitoring has earlier been tested although conventional surveying technologies are still more preferred. Since terrestrial laser scanners are capable of acquiring a large amount of highly detailed geometrical data from a surface it is of interest to study the metrological advantages of the terrestrial laser scanning technology for deformation monitoring of structures. The main intention of this study is to test the applicability of terrestrial laser scanning technology for determining range and spatial distribution of deformations during bridge load tests. The study presents results of deformation monitoring proceeded during a unique bridge load test. A special monitoring methodology was developed and applied at a static load test of a reinforced concrete cantilever bridge built in 1953. Static loads with the max force of up to 1961 kN (200 t) were applied onto an area of 12 m² in the central part of one of the main beams; the collapse of the bridge was expected due to such an extreme load. Although the study identified occurrence of many cracks in the main beams and significant vertical deformations, both deflection (–4.2 cm) and rising (+2.5 cm), the bridge did not collapse. The terrestrial laser scanning monitoring results were verified by high-precision levelling. The study results confirmed that the TLS accuracy can reach ±2.8 mm at 95% confidence level.

Keywords: Terrestrial Laser Scanning, precise levelling, load testing, monitoring deformations, cantilever beam.

1. Introduction

In recent years Terrestrial Laser Scanning (TLS) has become more widely used in surveying of different structures. The main advantage of using TLS technology in such projects lies in its capability of acquiring a complete set of data of the whole surface of interest within a short period of time. TLS also enables surveying of inaccessible parts of structures with a high level of detail. Advantageously the technology does not rely on specific reference points as are needed for conventional technologies such as levelling and tacheometry. A thorough overview of the TLS technology can be found in Staiger (2003), Quintero *et al.* (2008), Reshetyuk (2009) and Vosselman and Maas (2009). The quality analysis of TLS can be found in Reshetyuk (2010) and Lichti (2010).

Geodetic deformation monitoring of different structures is conducted commonly by using either total station

observations, precise levelling, terrestrial photogrammetry or GPS (Global Positioning System) surveys. Fairly seldom TLS has been used in deformation monitoring due to the novelty of the technology. Nevertheless, deformation monitoring using TLS technology is reported by Tsakiri and Pfeifer (2006), who gave an assessment of the quality of results and also reviewed aspects that are recommended to be considered for such research. Monserrat and Crosetto (2008) applied the least squares 3D surface matching (a method proposed originally by Gruen and Akca (2005)) to identify deformations based on repeated TLS scans. Riveiroa *et al.* (2013) validates TLS technology and photogrammetric techniques for deformation monitoring, the resulting TLS accuracy was estimated to reach 10 mm.

The main purpose of conducting a load test of an existing bridge is to acquire information on the carrying capacity of the structure, which condition has been influenced by

age and traffic. The need for load testing arises from doubts about the quality of construction or design or when some visible damage has occurred. The load testing is particularly valuable where public confidence is involved. Also a load test may be intended to establish the behaviour of a structure, analysis of which might otherwise be impossible for a variety of reasons (Bungey, Millard 1996). During bridge load tests elements of the beams are stretched allowing the beam to bend. Thus there is a need to determine deformations of inaccessible parts of the structure of the bridge, such as the bottom surface of the beams.

This study focuses on geodetic monitoring of bridge deformations occurring during static load test. Two surveying technologies: TLS and precise levelling were used for this. A similar work is reported by Zogg and Ingensand (2008) who described deformation monitoring at a load test of a viaduct using a TLS and precise levelling simultaneously at the deck of a viaduct itself. The main objective of the present study is to explore the behaviour of the bridge structures during the load test with extreme static loads – according to the pre-calculations the bridge was expected to collapse. This prevented placing the TLS monitoring station either on or under the bridge deck. An accuracy assessment of using TLS technology in unfavourable and hazardous survey conditions is investigated. Precise levelling results are used for verifying TLS data accuracy. A brief summary concludes the paper.

2. Bridge load tests

Bridge load tests provide researchers and bridge engineers with valuable information about the actual behaviour of structure. There are always some discrepancies between pre-calculations and the actual test results, since different calculation methods involve several variables and usually adopt some simplifications. Sometimes the structure is too damaged for adequate evaluations of the load-bearing capacity.

Bridges are tested either using static or dynamic loads. For static load tests (depending also on expected outcome) heavy vehicles (dumper trucks, army tanks, etc.) or heavy items (metal blocks, sand bags, etc.) are usually placed on bridge deck. Displacements, deformations and the incipency of cracks in the structure are investigated during the test, Fig. 1.

Static load tests can be divided into three groups: appending, proving and destructive load test (Ryall 2001).

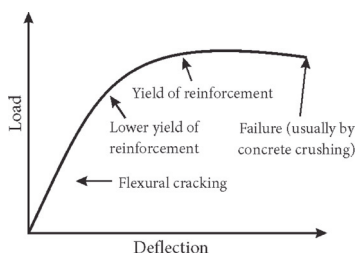


Fig. 1. Typical load deflection curve for under-reinforced beam (Bungey, Millard 1996)

The appending load test is the most common testing method, and it is usually carried out by bringing a load to bearing support that is up to 70% of the designed load value without causing any permanent damage to the structure. The actual test results are usually compared with pre-calculated values to determine whether the selected calculation method was correct or not. The results also show the technical condition of the structure. In proving load tests the load is selected to be equal to the load that is theoretically destructive to particular bridge. This method provides direct proof of the actual carrying capacity of the bridge, but there is a significant risk of damage to the bridge structure. The third option is to load the bridge up to the point of destruction. This load test is rarely used – mostly on old bridges which will be demolished during or after the testing anyways, the main aim being to provide information on the current physical condition of similar type bridges elsewhere. The destructive method was used in this case study.

Dynamic load testing provides data on the dynamic behaviour of the structure such as displacements, deformations, natural frequencies, mode shapes and damping. Dynamic load tests are considered more hazardous, due to the vibrations caused in the structure, as they generally lead to extensive damage. In the case of dynamic load tests, a vehicle with several axles and a specific weight travelling on the bridge at various speeds is generally used. For short bridges the dynamic load test is rarely carried out.

There are many procedures to be carried out before and after the bridge load test. Just before the test, a detailed inspection of the structure must be conducted. It is vital to record the initial state of the structure, since after the load testing it would not be possible. Pre-calculations are needed for estimating expected magnitude of deformations occurring during the load test. Theoretical pre-calculations describe the behaviour of the structure during the test and evaluate the critical moment and mode of the structure's failure. There are usually two types of pre-calculations – one based on the original design (technical documentation, drawings etc) and the other, on the actual parameters (e.g. in situ measured dimensions, material properties). Prior the test, a test plan is usually formulated where all actions involved in the testing are described in detail. The testing ends with a thorough final report which contains, in addition to the analysis of the test results, a description of the procedures carried out before and after the test.

Load testing of bridges is not required by law in Estonia, but in practice there is a need for about 2–5 tests every year. *Estonian Road Administration* acknowledges that even though several international standards related to load testing (*ISO 2394:1998 General Principles on Reliability for Structures*, *ISO 13822:2010 Bases for Design of Structures – Assessment of Existing Structures*, *ISO 14963:2003 Mechanical Vibration and Shock – Guidelines for Dynamic Tests and Investigations on Bridges and Viaducts*, *ISO 18649:2004 Mechanical Vibration – Evaluation of Measurement Results from Dynamic Tests and Investigations on Bridges* etc.)

exist, but there is a need for developing comprehensive national guidelines for this complicated procedure. The present case study is meant to be a step towards development of bridge load testing guidelines for Estonia.

There are around 950 state highway bridges in Estonia, 82% of which are made from reinforced concrete, 69% of which have a total length of 3–25 m, and 64% of which were built between 1950 and 1990. The structures of these bridges were mostly standardised, e.g. the case study bridge had a structure typical of the 1950-ies. The *Estonian Road Administration* is interested in investigating these bridges more thoroughly, since heavy vehicles, salting of the roads, complicated climate conditions (the amount of rainfall exceeding evaporation and temperatures fluctuating substantially around 0 °C, resulting in the corrosion of reinforcement steel bars and the cracking of concrete), inappropriate technical solutions, and insufficient maintenance over the decades have degraded the load carrying capacity of these bridges.

3. Review on geodetic monitoring technologies

In overall, there are different devices that are used to determine characteristics of deformations such as strain gauges, inclinometers, crack microscopes, rulers and callipers. Geodetic instruments include precise levelling instruments, total stations, terrestrial laser scanners and terrestrial photogrammetric instruments.

However no static devices were used in the case study due the risk of structural failure thus the possibility of shattering the assembled devices. Since the case study used two geodetic monitoring techniques – precise levelling and TLS, their principles are briefly reviewed below.

3.1. Precise levelling

Precise levelling measurement is considered the most accurate way of determining heights and is expected to provide the best quality of results in deformation monitoring process. Precise levelling uses highly accurate levelling instruments and levelling staff(s). The data processing is simple and very straightforward. The observing procedures applied in precise levelling are more rigorous than in general engineering levelling. Sub-millimetre accuracy is only achieved by using modern levelling instruments in conjunction with calibrated invar levelling staff(s).

3.2. Terrestrial laser scanning

Based on scanning technology, TLS's are divided into triangulation, Time of Flight (TOF) and Phase-Shift (PS) scanners.

Triangulation laser scanners are mainly used in applications generally requiring an operating range that is less than 25 m; nonetheless triangulation scanners have very high accuracies in the order of tenth of millimetres. In principle triangulation scanners are considered also as terrestrial laser scanners, but due to the limited working range, they may not be categorized in the same group of terrestrial laser scanners (Schulz 2007).

TOF laser scanners make use of short laser pulses by which they scan their entire field of view one point at a time by changing the range finder's direction. The view direction of the laser range finder is changed by a deflection unit (Quintero *et al.* 2008). Since the laser pulse travels with a constant speed, the speed of light, the distance between the scanner and the object is determined with the following expression (Vosselman, Maas 2009):

$$\rho_i = \frac{ct}{2r}, \quad (1)$$

where ρ_i – the range of the i^{th} point with respect to scanner location; c – the speed of light in vacuum (i.e. 299 792 458 m/s).

If the light waves travel in the air-filled environment then a correction factor equal to the refractive index, which depends on the air temperature, pressure and humidity, must be applied to c , e.g. according to Vosselman and Maas (2009) $r \approx 1.00025$. Typical pulsed TOF laser scanners measure up to 50 000 points per second. The distance accuracy of TOF scanners depends mostly on timing accuracy resulting normally an accuracy of 4 to 10 mm.

In PS laser scanners the emitted (incoherent) light is modulated in amplitude and fired onto a surface. The scattered reflection is collected and a circuit device measures the phase difference between the sent and received wave-forms, hence a time delay. According to the distance measuring equation of the TOF scanners, the distance to the target can be found by the demodulation of the back-scattered signal by means of four sampling points that are triggered to the emitted wave (Quintero *et al.* 2008):

$$\rho_i = \frac{c\Delta\Phi}{4\pi f_{mod}}, \quad (2)$$

where $\Delta\Phi$ – phase difference; f_{mod} – modulation frequency.

This method allows faster measuring, up to 1 000 000 points per second, typically within ranges under 100 m. The accuracy of PS scanners depends on the modulated wavelength and the signal to noise (SNR) ratio resulting normally in an accuracy of 2 to 5 mm (Quintero *et al.* 2008).

Thus, a TLS is able to acquire a large number of points within seconds; the acquired data forms a point cloud:

$$\{(x_i, y_i, z_i, I(x_i, y_i, z_i)), i = 1, \dots, n\}, \quad (3)$$

where x_i, y_i, z_i denote the coordinates of the i^{th} survey point in the scanner's intrinsic coordinate system; $I(x_i, y_i, z_i)$ – the intensity related to the i^{th} point; n – the number of acquired survey points. Intensity is a value of the returned signal strength, which is usually stored as a unitless number in the range of 0 to 2⁸. If the scanner is equipped with a digital photo camera, the colour values from the photos are also added to each survey point. The coordinates (x_i, y_i, z_i) of the i^{th} survey point with respect to the scanner's intrinsic coordinates are determined using the point's

spherical polar coordinates: range, horizontal direction, and vertical angle.

In order to transform the coordinates from the intrinsic coordinate system to some extrinsic coordinate system (e.g. national) a rigid-body transformation is used (cf. also Mill et al. 2014).

$$\begin{bmatrix} x_i^E \\ y_i^E \\ z_i^E \end{bmatrix} = \begin{bmatrix} x_s^E \\ y_s^E \\ z_s^E \end{bmatrix} + \mathbf{R}_3(\kappa)\mathbf{R}_2(\varphi)\mathbf{R}_1(\omega) \begin{bmatrix} x_i \\ y_i \\ z_i \end{bmatrix}, \quad (4)$$

where (x_i^E, y_i^E, z_i^E) , $i=1, \dots, n$ denote the coordinates of a scanned point i in the extrinsic coordinate system. (x_s^E, y_s^E, z_s^E) are the coordinates of the centre of the laser scanner expressed in the extrinsic system and (x_i, y_i, z_i) , $i=1, \dots, n$ are the coordinates of the i^{th} scanned point expressed in the intrinsic coordinate system. $\mathbf{R}_1, \mathbf{R}_2, \mathbf{R}_3$ – the matrices for rotation around the x -, y - and z -axes respectively; $(\omega, \varphi, \kappa)$ – the rotation angles from the extrinsic coordinates to the scanner intrinsic coordinates about the x -, y - and z -axes. The process is also known as georeferencing.

If the scanner is equipped with a dual-axis compensator, then the instrument's z -axis is parallel with the extrinsic system's z -axis and thus the rotation angles ω, φ become to zero, i.e. $\mathbf{R}_1, \mathbf{R}_2$ in Eq (4) are identical (unit) matrixes.

4. The case study

4.1. Description of the bridge

The European route E20 is a West-East United Nations (UNECE) across-sea route covering some 1880 km spanning Northern Europe from the United Kingdom, Ireland, Denmark, Sweden, Estonia and finally to Russia's second largest city Saint Petersburg. In Estonia the European route E20 connects the capital Tallinn and the third largest city Narva, located the eastern point of Estonia, by the Russian Federation border.

The load test presented in this study was performed on a bridge No. 156 located at kilometre 66 from Tallinn. The bridge crosses the Loobu River. The bridge was built in 1953 from reinforced concrete using a typical project from the year 1947 (*Sbornik tipovykh projektov zhelezobetonnykh i kamennykh iskustvennykh sooruzheniy. Vypusk 6. Zhelezobetonnye balochno-konsol'nye proletnye stroeniya. Prolety L0 – 12, 16, 20, 25 i 30 m. Gabarit G-7. Nagruzka N-10 i N-60. 1947*). The total length of the two-lane bridge was 31.2 m and width 8.5 m. The bridge was made of concrete mark M140 which by calculation had compression strength of $f_{ck} = 15$ MPa. The main reinforcement steel was mark St.3 (yield stress $f_y = 210$ MPa) with a diameter of 38 mm. The cover of the main reinforcement was 30 mm (Fig. 2). The form of the bridge structure was beam-type with two cantilevers 6.9 + 17.4 + 6.9 m. The bridge was originally designed to correspond load models N-10 and NG-60. According to former Soviet Union bridge norms the load model N-10 consists of several consecutive two-axle trucks where one of them weights 13 t (127.5 kN) and others 10 t (98 kN). The load model NG-60 consists of one caterpillar vehicle with a total load of 60 t (589 kN). The daily traffic frequency of the bridge was around 2700 cars – the carrying capacity and width appeared to be insufficient for contemporary needs. The general condition of the bridge was unsatisfactory before the testing – the index of condition was 63% out of 100% calculated by the Pontis Bridge Management System. That meant the bridge needed an overhaul or replacement during the next five years. An extensive corrosion of the reinforcement steel bars of the main beams had caused cracking of the concrete covers for reinforcement. Due to long-term self-weight and increased traffic load the main beams had also vertical cracks (their widths reached up to 0.1 mm).

After the load test the bridge was demolished.

4.2. Preliminary calculations and expected results

For pre-calculations of internal forces to occur during the bridge test load, all safety factors were taken from the former Soviet Union bridge norms (SNiP 2.05.03-84 *Mosty i truby*):

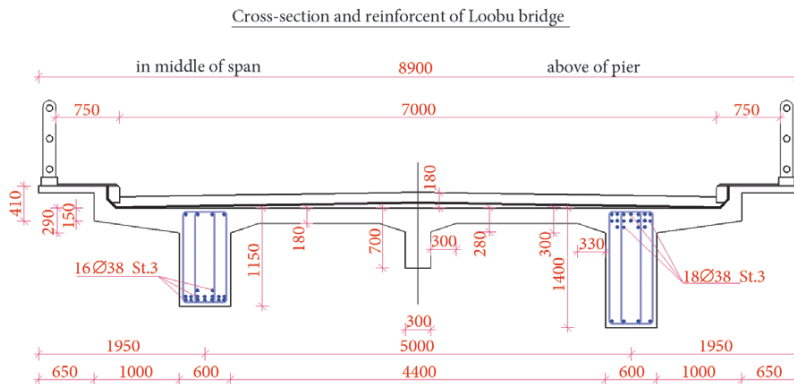


Fig. 2. A cross-section and reinforcement (depicted as blue dots and blue line in the beams) of the tested bridge

- for self-weight coefficient $\gamma_f = 1.1$;
- for N-10 $\gamma_f = 1.4$ and dynamic factor for 32.1 bridge length $1 + \mu = 1.1$;
- for NG-60 $\gamma_f = 1.1$.

Calculations were carried out using the 3D finite element program Bentley STAAD.Pro with different loading schemes (trucks, caterpillar vehicles, and other types of loads) Fig. 3.

The max bending moment (M_{Ed}) for the southern beam due to its own weight and the 60 t caterpillar vehicle was calculated to be 1916.5 kNm, yielding a predicted deflection of up to -13.6 mm. The calculated bending resistance (M_{Rd}) at the centre of the southern beam based on the material's strength properties given in the design project was 3387.0 kNm. The calculated bending resistance was almost twice the bending moment from the weight of the normative 589 kN (60 t) load. The max bending moment (M_{Ed}) from the designed test load of 1961 kN was calculated to be 5125.0 kNm, which is approx 1.5 times larger than the design bending resistance based on the bridge design project. The bending resistance (M_{Rd}), calculated by using material characteristic from the laboratory test was 5439 kNm, which was ~1.1 times larger than the bending moment from test load.

Based on preliminary calculations (Table 1) the designed test load is predicted to cause smaller bending moment (M_{Ed}) than the load capacity of the bridge.

The expected deflection from the max testing load was -50.3 mm (EN 1992-1-1:2004 Eurocode 2: Design of Concrete Structures – Part 1-1). However, using a linear-elastic calculation without cracking and Young's modulus obtained from laboratory testing of the concrete, the deflection was calculated to be -31.6 mm.

4.3. Design of the load test and visual deformation monitoring results

For the load test a hundred pieces of special two-ton metal blocks 2.00×0.40×0.35 m were used. The load test and the monitoring process were divided into four stages:

- (i) documenting the situation before the loading,
- (ii) placement of the 785 kN load,
- (iii) placement of the 823 kN load,
- (iv) placement of the remaining 353 kN load.

The bridge was loaded in total with a total force of a load of 1961 kN (200 t), which clearly exceeds the designed load-bearing capacity of 589 kN (60 t), see section 4.1. The load (altogether 1961 kN) was piled up in the centre of the bridge on its southern side within 2×6 m rectangular area, Fig. 4. After the first two loading the bridge was set to sag for at least 30 min; after the loading of the remaining weights, the bridge was set to sag for at least 60 min. Monitoring begun after the deformations were stabilized.

In spite of fact that the total load exceeded the nominal carrying value more than three times, the bridge did not collapse. The main reasons to explain this was that the actual building materials used for the bridge components were much stronger than described in the original 1947 engineering project. The principles of calculation method for

reinforced concrete structures more than 60 ears ago were different compared to nowadays.

The laboratory tests results on the concrete specimen from the Loobu bridge proved that the compression strength of concrete ($f_{ck} = 40$ MPa) was approximately 2.7 times larger than in the design project ($f_{ck} = 15$ MPa). The high compression strength of concrete is partially explainable by the fact that compression strength increases in time. The average yield stress of the reinforcement ($f_y = 295$ MPa) was ~1.4 times higher than in the design yield stress $f_y = 210$ MPa. According to the former Soviet Union standard GOST 380-57, the steel mark St.3 has minimal characteristic yield strength of $f_{yk} = 240$ MPa and ultimate limit stress $f_{uk} = 400$ -500 MPa. The laboratory test result of the tensile strength of reinforcement f_u was 426 MPa. The strength characteristics of the reinforcement steel used in the bridge construction meets the material class St.3.

Crack widths caused by the test loads at the bottom side of main beams reached up to 0.5 mm (in the middle of the span after every 15...20 cm), exceeding thus the allowed values of the serviceability limit state. The max admissible width of crack is 0.3 mm (EN 1992-1-1:2004).

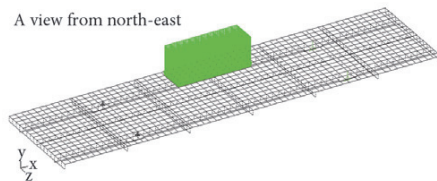


Fig. 3. Example of 3D model of the superstructure of the bridge with testing load



Fig. 4. Full load (1961 kN) placed on the bridge, image view from the scanners position from the Southern side of the bridge

Table 1. Bending moments and resistance's

	Bending resistance (M_{Rd})	Bending moment (M_{Ed})
Based on the bridge design project	3387 kNm	1916 kNm
Based on the load test design	5439 kNm	5125 kNm
Differences	62%	37%

4.4. Geodetic monitoring

The deformation monitoring of the load test was carried out using precise levelling and a novel terrestrial laser scanning technology. Precise levelling results were used to verify the accuracy of the TLS results in this study. Verifications of the TLS accuracy at bridge-works by modern electronic tacheometry is found, e.g. Mill *et al.* (2011). The monitoring process was carried out simultaneously but from different locations of the bridge; precise levelling on the deck of the bridge, whereas TLS observations were preceded from one side of the bridge aiming to observe the bottom surfaces of the cantilever beams.

4.4.1. Deformation monitoring using a precise levelling

A precise digital level Trimble DiNi03 with two calibrated invar bar code levelling staffs was used for determining bridge deformations. According to specifications the instrument's standard deviation is 0.3 mm on 1 km of double run levelling with invar precision bar code staffs. The precise levelling instrument Trimble DiNi03 and used invar bar code levelling staffs were calibrated and certified at the *Metrological Laboratory of the Finnish Geodetic Institute* in December 2010.

For deformation monitoring 20 reference points were embedded into the deck of the bridge (Fig. 5) at its northern and southern sides. A 0.60 m long steel rod as a temporary reference mark was embedded away from the bridge deck on a stable soil. The levelling was accomplished from two stations placed away from the bridge deck.

The precise levelling was conducted before the loading and after each loading session.

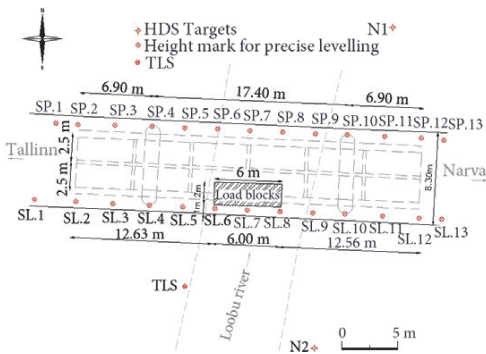


Fig. 5. Locations of the levelling height marks, TLS station, HDS targets and the load blocks. The bridge columns and cantilever beams with beam supports are exhibited by dashed lines

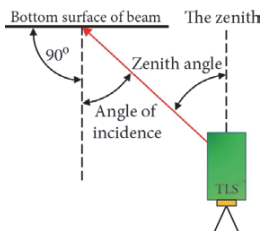


Fig. 6. Angle of incidence at scanning, the red line indicates the laser beam

4.4.2. Deformation monitoring using a TLS

A TOF Leica ScanStation C10 was used for monitoring of bridge deformations. The max range of the device is 300 m with a $360 \times 270^\circ$ field of view and max scanning rate of up to 50 000 points/sec. The manufacturer's accuracy specifications for the range and angle are ± 4 mm and ± 12 arc-sec, respectively. Several studies e.g. Abbas *et al.* (2013) and Antanavičiūtė *et al.* (2013) have investigated the calibration parameters of laser scanners Leica ScanStation C10. The results of the studies revealed only minor systematic errors in range measurement and in both horizontal and vertical angle measurement. The residuals corresponded with the manufacturer's accuracy specifications. Concerning the laser scanner Leica ScanStation C10 used in our study, it was calibrated before and after the bridge load test. In both occasions the same conclusion was reached and certified.

The TLS was erected at the best possible location at the distance of 6 m from the southern edge of the bridge (Fig. 5). It remained in the same location during the entire course of measuring. As the load test took place in early spring, when the ground had not yet thawed, the level compensator of the scanner was continuously monitored to detect and compensate any movements by the subsidence of the tripod.

Nevertheless, to ensure the scanning accuracy the scanner was reoriented before each TLS session using the 3"×3" HDS (High-Definition Surveying) targets mounted near the bridge (Fig. 5). A detailed overview of TLS orientation methods therewith a registration method is given by Becerik-Gerber *et al.* (2011). Also Alba and Scaioni (2007) give a thorough overview of common registration processes and georeferencing techniques. The used TLS is equipped with a dual-axis compensator.

The scanner was set at the lowest location at the river bank to minimize incidence angles (Fig. 6) of laser beams. Recall, that placing the scanner under the bridge would have been hazardous due to the risk of the bridge collapsing. Lichti (2007) and Soudarissanane *et al.* (2007) suggest scanning at incidence angles below 65° , and moreover, Soudarissanane *et al.* (2011) states that increased incidence angles cause signal deterioration by approximately 20%. The actual incidence angle values at survey were between 80° and 87° at the southern and northern beams of the bridge, respectively. Although the incidence angle values were larger than the aforementioned threshold values, no remarkable unfavourable behaviour was detected from the achieved results.

Due to large incidence angles (80 – 87°), the angular precision determines the precision of the height of the scanned points. The law of error propagation is used to compute the precision of the height of the scanned point:

$$\sigma^2(\Delta \hat{h}) = \sum_{i=1}^n \left(\frac{\partial f}{\partial w_i} \right)^2 \sigma^2(w_i), \quad (5)$$

where $\sigma^2(\Delta \hat{h})$ denotes the combined variance of height increment with respect to the scanner origin. Note that $\Delta \hat{h}$ – an estimate (derived from the TLS range and angle

measurements, Eq (6) of the actual height increment Δh ; f – the function $\Delta h = f(w_i)$, $i = 1, \dots, n$, relating the observations (w_i , $i = 1, \dots, n$, and the height increment; $\sigma^2_{(w_i)}$ – the variance of the i^{th} observable. The observation equation, i.e. function f , for the i^{th} scanned point is written as:

$$\Delta \hat{h}_i = \rho_i \cos \varphi_i, \quad (6)$$

where ρ_i – slope distance from the scanner to a contact point in the reflective surface; φ_i – zenith angle (Fig. 6); $\Delta \hat{h}$ – the resulting height increment.

Inserting Eq (6) into Eq (5) and calculating the derivatives, the combined standard uncertainty $\sigma(\Delta \hat{h})$ of the height increment of a survey point is found as:

$$\sigma(\Delta \hat{h}) = \pm \sqrt{\cos^2 \varphi_i \sigma_{dist}^2 + \rho_i^2 (-\sin \varphi_i)^2 \sigma_{angle}^2}, \quad (7)$$

where σ_{dist} – the scanner’s standard distance uncertainty; σ_{angle} – the scanner’s standard angular uncertainty. Since $\sigma(\Delta \hat{h})$ depends on the angle φ_i , i.e. it is individual for each point i .

The combined standard uncertainties $\sigma(\Delta \hat{h})$ for the height increments at four points, two points on the southern beam and two points on the northern beam were calculated. The two points on the southern beam were located at distances (ρ) of 8.44 m and 19.66 m from the scanner at zenith angles (φ) of $81^\circ 02'$ and $86^\circ 24'$, respectively. The two points on the northern beam were located at distances of 13.43 m and 21.48 m from the scanner at zenith angles of $84^\circ 23'$ and $86^\circ 53'$, respectively. Numerical values for σ_{dist} and σ_{angle} were taken from the manufacturer’s specifications.

Inserting these values into Eq (7) the mean value of four combined standard uncertainties of height increments $\sigma(\Delta \hat{h})$ of the survey points equals ± 1.0 mm (one σ), which by adopting the 95% confidence interval (two σ) yields an uncertainty of ± 2.0 mm. Thus the uncertainty of sequential TLS data sets (obtained from different monitoring epochs) equals to $2.0\sqrt{2} = \pm 2.8$ mm. Hence, the height differences exceeding ± 2.8 mm between two TLS epochs at a location is considered as actual deformations.

5. Deformation analysis between different epochs

5.1. Results from TLS data

The processing of TLS data was conducted using a commercial 3D Point Cloud Processing Software Leica Cyclone developed by Leica Geosystems AG. The processing included removing noise from point clouds, creating surface meshes and deformation analysis between a surface created from the TLS data before the load test and surfaces created from TLS data from sequential load test epochs.

Under a load of 785 kN at its centre, the southern cantilever beam deflected by up to -1.8 cm (Fig. 7). Note that the western end of the beam rose by up to $+0.6$ cm; at the same time, the eastern end of the beam showed in some parts a deflection of up to -0.3 cm but no detectable rise.

A max deflection of -0.9 cm occurred at the centre of the northern cantilever beam (Fig. 7). The western end of the beam rose by up to $+0.4$ cm; at the same time, the eastern end of the beam showed in some places a deflection of up to -0.7 cm and in some cases a rise of up to $+0.3$ cm.

Deformation measurement values derived from TLS data indicate that the centre southern cantilever beam,

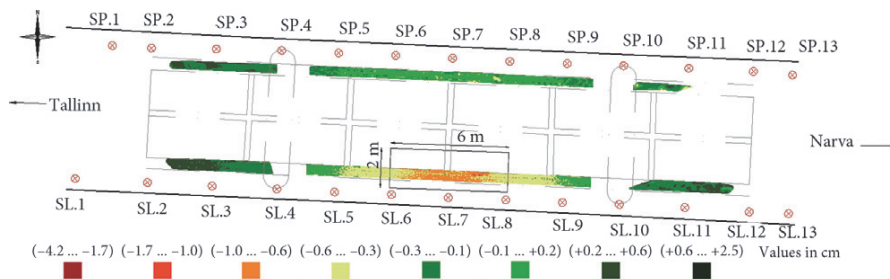


Fig. 7. Results from the loading of 785 kN force

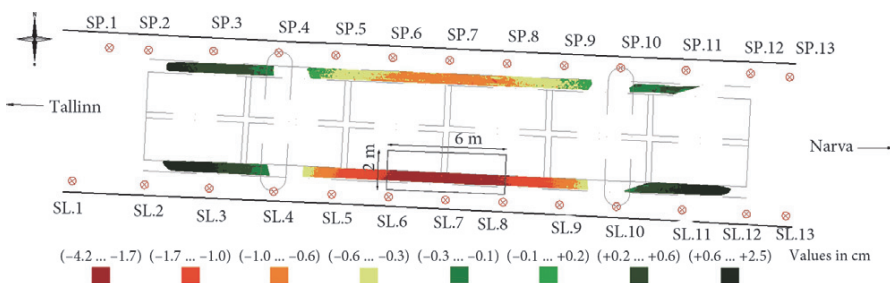


Fig. 8. Results from the loading of 1608 kN force

under a load of 1608 kN, deflected by a max of -3.0 cm (Fig. 8). Both the western and the eastern ends of the beam show a rise of up to $+1.4$ cm.

The centre northern cantilever beam deflected by up to -1.8 cm (Fig. 8). The western end of the beam shows a rise of up to $+1.0$ cm; the eastern end of the beam, a rise of up to $+0.6$ cm.

Deformation measurement values derived from TLS data when a max load of 1961 kN was applied indicate that the centre southern cantilever beam deflected by up to -4.2 cm (Fig. 9). The western end of the beam shows a rise of up to $+2.2$ cm; the eastern end of the beam, a rise up to $+2.5$ cm.

The centre northern cantilever beam showed a deflection of up to -2.4 cm (Fig. 9). The western end of the

beam showed a rise of up to $+1.7$ cm; the eastern end of the beam, a rise of up to $+1.2$ cm.

The deformation magnitudes agree roughly with the predictions (Section 4.2).

5.2. Comparison of precise levelling and TLS results

Precise levelling is based on difference of readings from a static invar bar code levelling staff positioned on a benchmark located some distance away from the bridge deck and readings from a second invar bar code levelling staff placed on embedded bolts to the bridge deck.

The bolts for levelling had to be placed a bit off from the exact location of the beams (Fig. 5). Therefore, in order to compare precise levelling results with TLS results, the longitudinal locations of the bolts were used as reference

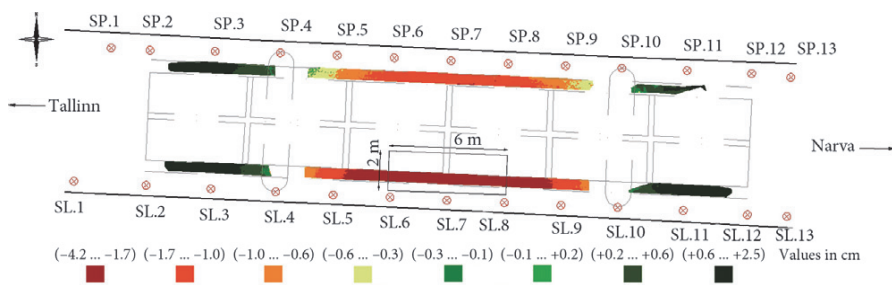


Fig. 9. Results from the loading of 1961 kN force

Table 2. Deformations determined by precise levelling and TLS

Load, kN	Deformations detected by TLS, cm						Deformations detected by precise levelling, cm					
	Southern beam			Northern beam			Southern beam			Northern beam		
	Deflection	Rising West end	Rising East end	Deflection	Rising West end	Rising East end	Deflection	Rising West end	Rising East end	Deflection	Rising West end	Rising East end
758	-0.7	+0.3	+0.1	-0.3	+0.5	+0.2	-0.808	+0.428	+0.323	-0.123	+0.172	+0.051
1608	-2.1	+0.7	+0.6	-0.8	+1.0	+0.5	-2.269	+1.437	+1.282	-0.560	+0.784	+0.668
1961	-3.2	+1.2	+1.1	-1.4	+1.7	+1.0	-3.542	+2.394	+2.597	-1.111	+1.530	+1.686

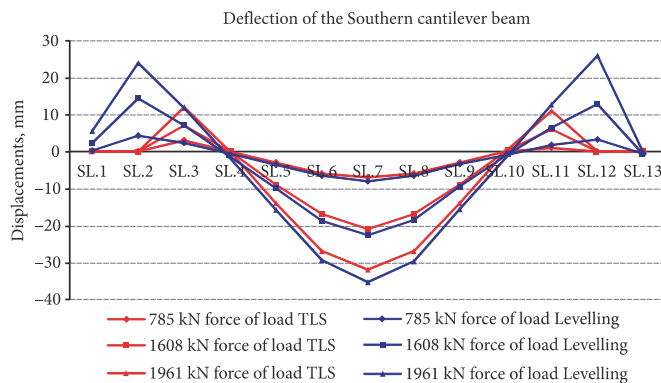


Fig. 10. Comparison of TLS and levelling results of the Southern beam. Note: at the centre of the beam (SL.7) deflection difference between TLS and levelling is under 785 kN + 0.108 cm; under 1608 kN + 0.169 cm; under 1961 kN + 0.342 cm

points when determining the heights in the middle of the bottom surface of the beam, making the compared points equal in the longitudinal direction.

The TLS and levelling detected deformation values are presented and in Table 2.

Comparison of corresponding deformation values (Table 2) reveal a reasonable agreement between the TLS and precise levelling results. Note however, that TLS data is missing for the very beginning of the beams at SL 1–2 and SP 1–2; also TLS data is missing at the very end of the bridge deck at SL 12–13 and SP 12–13 (Figs 10 and 11) due to the limited bridge opening. From the comparison (Figs 10 and 11), a certain pattern for discrepancies emerges. The comparison results of the southern beam indicate that precise levelling results show slightly higher deflection values than TLS results; in the case of the northern beam, precise levelling results show slightly lower deflection values. Although the differences are noticeable, the differences are just within millimetres (detailed values are in Table 3).

The detected differences have occurred most likely due to the following. First, the accuracy of the TLS, since the TLS data uncertainty in this case was considered ± 2.8 mm. Second, the TLS and precise levelling data were acquired from different surfaces – the TLS data addresses the bottom surface of beams, whereas the levelling was proceeded on the bridge deck. In addition, the differences were also due to the eccentric position of the load. When recalculating the precise levelling results by considering

the inclination of the bridge due to the eccentric loading, the max displacement for the southern beam becomes -3.1 cm (TLS yielded -3.2 cm) and for the northern beam -1.5 cm (TLS -1.4), thus, the actual accuracy is estimated to be ± 1 mm.

6. Conclusions

1. In this study a unique static load tests of a 60 year old cantilever beam bridge was presented. The loading test was divided into three loading and deformation monitoring stages. The stages consisted of forces of loads 785 kN, 1608 kN and with a max load of 1961 kN. The loading was carried out mainly on the southern cantilever beam but deformations were determined on the northern beam as well. For deformation monitoring terrestrial laser scanning technology simultaneously with precise levelling was applied. The pre-calculated max deflection of the bridge was -50.3 mm; according to precise levelling the actual deflection of the bridge deck at the max load of 1961 kN was -35.4 mm which is then 1.4 times smaller than pre-calculations predicted.

2. In spite of fact that the total load exceeded design value more than three times, the bridge did not collapse. The main reasons to explain this was that the actual materials were much stronger than described in engineering project and the principles of calculation method for reinforced concrete structures more than 60 years ago were different compared to nowadays. There were no significant

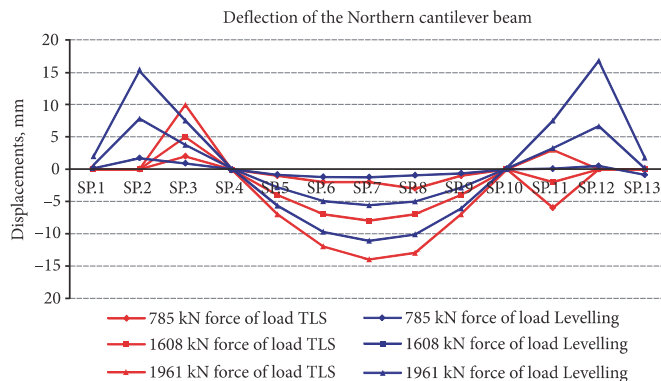


Fig. 11. Comparison of TLS and levelling results of the Northern beam. *Note:* at the centre of the beam (SP.7) deflection difference between TLS and levelling is under 785 kN -0.177 cm; under 1608 kN -0.24 cm; under 1961 kN -0.289 cm

Table 3. Comparison of deformation results

Load, kN	Differences, cm					
	Southern beam			Northern beam		
	Centre	West end	East end	Centre	West end	East end
758	+0.108	-0.128	-0.223	-0.177	+0.328	+0.149
1608	+0.169	-0.737	-0.682	-0.240	+0.216	-0.168
1961	+0.342	-1.397	-1.497	-0.289	+0.17	-0.686

Note: results are derived via TLS – Precise levelling, cf. Table 2.

damages of the bridge structure, only crack width exceeded the allowed values of the serviceability limit state almost two times. The study results are useful at further bridge load tests, since the novel technology provides unprecedented possibilities (as opposed to conventional surveying technologies) and excessive datasets for more extensive data analysis.

3. Results from this study confirm the assumed accuracy of terrestrial laser scanning on 95% confidence level of ± 2.8 mm. The differences between terrestrial laser scanning and precise levelling vary within few millimetres. Therefore, in general TLS is suitable for detecting deformations within millimetre accuracy but it cannot be used for works demanding sub millimetre accuracy. However, terrestrial laser scanning allows acquiring high-resolution (almost continuous) data over the entire surface, in contrast to low-resolution point-wise levelling data. TLS technology allows remote monitoring of hazardous processes, thus, ensuring better safety of surveyors in such load tests. Note also that the terrestrial laser scanning data processing algorithms are currently still in the development phase. Within foreseeable future it will be possible to solve such complex data management tasks even more efficiently.

Acknowledgements

The Estonian Road Administration is thanked for allowing using the geodetic monitoring data. The used TLS Leica ScanStation C-10 and the licensed 3D Point Cloud Processing Software Leica Cyclone is purchased within frames of the Estonian Research Infrastructures Roadmap object Estonian Environmental Observatory (funding source 3.2.0304.11-0395, project No. AR12019). Part of this research is supported by the Estonian Environmental Technology R&D Programme KESTA research project ERMAS AR12052. The authors thank the two anonymous reviewers for their valuable comments.

References

- Abbas, M. A.; Setan, H.; Majid, Z.; Lichti, D. D.; Chong, K. A. 2013. A Self-Calibration of the Leica Scanstation C10 Scanner, in *Proc. of the IEEE Business Engineering and Industrial Applications Colloquium (BELAC)*. 7–9 April 2013, Langkawi, Malaysia, 262–266.
<http://dx.doi.org/10.1109/BELAC.2013.6560128>
- Alba, M.; Scaioni, M. 2007. Comparison of Techniques for Terrestrial Laser Scanner Data Georeferencing Applied to 3-D Modeling of Cultural Heritage, in *Proc. of the 3D-ARCH 2007 "Virtual Reconstruction and Visualization of Complex Architectures"*, XXXVI-5/W47. 12–13 July 2007, Zurich, Switzerland.
- Antanavičūtė, U.; Obuchovski, R.; Paršeliūnas, E. K.; Popovas, M. G. D.; Šlikas, D. 2013. Some Issues Regarding the Calibration of the Terrestrial Laser Scanner Leica Scanstation C10, *Geodesy and Cartography* 39(3): 138–143.
<http://dx.doi.org/10.3846/20296991.2013.840356>
- Becerik-Gerber, B.; Jazizadeh, F.; Kavulya, G.; Calis, G. 2011. Assessment of Target Types and Layouts in 3D Laserscanning for Registration Accuracy, *Automation in Construction* 20(5): 649–658. <http://dx.doi.org/10.1016/j.autcon.2010.12.008>
- Bungey, J. H.; Millard, S. G. 1996. *Testing of Concrete in Structures*. Glasgow, United Kingdom: Chapman & Hall. 286 p. ISBN 0-203-48783-4.
- Gruen, A.; Akca, D. 2005. Least Squares 3D Surface and Curve Matching, *ISPRS Journal of Photogrammetry and Remote Sensing* 59(3): 151–174.
<http://dx.doi.org/10.1016/j.isprsjprs.2005.02.006>
- Lichti, D. D. 2007. Error Modelling, Calibration and Analysis of an AM–CW Terrestrial Laser Scanner System, *ISPRS Journal of Photogrammetry and Remote Sensing* 61(5): 307–324.
<http://dx.doi.org/10.1016/j.isprsjprs.2006.10.004>
- Lichti, D. D. 2010. Terrestrial Laser Scanner Self-Calibration: Correlation Sources and Their Mitigation, *ISPRS Journal of Photogrammetry and Remote Sensing* 65(1): 93–102.
<http://dx.doi.org/10.1016/j.isprsjprs.2009.09.002>
- Mill, T.; Ellmann, A.; Aavik, A.; Horemuz, M.; Sillamäe, S. 2014. Determining Ranges and Spatial Distribution of Road Frost Heave by Terrestrial Laser Scanning, *The Baltic Journal of Road and Bridge Engineering* 9(3): 227–236.
<http://dx.doi.org/10.3846/bjrbe.2014.28>
- Mill, T.; Ellmann, A.; Uueküla, K.; Joala, V. 2011. Road Surface Surveying Using Terrestrial Laser Scanner and Total Station Technologies, in *Proc. of 8th International Conference Environmental Engineering*. Ed. by Čygas, D.; Froehner, K. D., 19–20 May 2011, Vilnius, Lithuania. Vilnius: Technika, 1142–1147.
- Monserrat, O.; Crosetto, M. 2008. Deformation Measurement Using Terrestrial Laser Scanning Data and Least Squares 3D Surface Matching, *ISPRS Journal of Photogrammetry and Remote Sensing* 63(1): 142–158.
<http://dx.doi.org/10.1016/j.isprsjprs.2007.07.008>
- Quintero, M. S.; Genechten, B. V.; de Bruyne, M.; Poelman, R.; Hankar, M.; Barnes, S.; Caner, H.; Budei, L.; Heine, E.; Reiner, H.; García, J. L. L.; Taronger, J. M. B. 2008. *Theory and practice on Terrestrial Laser Scanning*. Training material based on practical applications. 241 p.
- Reshetyuk, Y. 2009. *Self-Calibration and Direct Georeferencing in Terrestrial*. PhD thesis 978-91-85539-34-5. Stockholm: Kungliga Tekniska högskolan [Royal Institute of Technology]. Universitetsservice US AB.
- Reshetyuk, Y. 2010. A Unified Approach to Self-Calibration of Terrestrial Laser Scanners, *ISPRS Journal of Photogrammetry and Remote Sensing* 65(5): 445–456.
<http://dx.doi.org/10.1016/j.isprsjprs.2010.05.005>
- Riveiroa, B.; González-Jorgeb, H.; Varelab, M.; Jaureguic, D. 2013. Validation of Terrestrial Laser Scanning and Photogrammetry Techniques for the Measurement of Vertical Underclearance and Beam Geometry in Structural Inspection of Bridges, *Measurement* 46(1): 784–794.
<http://dx.doi.org/10.1016/j.measurement.2012.09.018>
- Ryall, M. J. 2001. *Bridge Management*. Butterworth-Heinemann. 464 p. ISBN 978-0750650779.
- Schulz, T. 2007. *Calibration of a Terrestrial Laser Scanner for Engineering Geodesy*. PhD thesis 17036. Berlin: Technical University of Berlin.
- Soudarissanane, S.; Lindenbergh, R.; Menenti, M.; Teunissen, P. 2011. Scanning Geometry: Influencing Factor on the Quality

- of Terrestrial Laser Scanning Points, *ISPRS Journal of Photogrammetry and Remote Sensing* 66(4): 389–399.
<http://dx.doi.org/10.1016/j.isprsjprs.2011.01.005>
- Soudarissanane, S.; van Ree, J.; Bucksch, A.; Lindenbergh, R. 2007. Error Budget of Terrestrial Laser Scanning: Influence of the Incidence Angle on the Scan Quality, in *Proc. of the 3D-NordOst 2007*. 6–7 September 2007. Berlin, Germany.
- Staiger, R. 2003. Terrestrial Laser Scanning, Technology, Systems and Applications, in *Proc. of the 2nd FIG Regional Conference*. 2–5 December 2003, Marrakech, Morocco.
- Tsakiri, M. L.; Pfeifer, N. 2006. Terrestrial Laser Scanning for Deformation Monitoring, in *Proc. of the 12th FIG symposium on Deformation Measurement and 3rd IAG Symposium on Geodesy for Geotechnical and Structural Engineering*. 22–24 May 2006, Baden, Austria.
- Vosselman, G.; Maas, H.-G. 2009. *Airborne and Terrestrial Laser Scanning*. Dunbeath: Whittles Publisher. 320 p. ISBN 978-1439827987.
- Zogg, H.-M.; Ingensand, H. 2008. Terrestrial Laser Scanning for Deformation Monitoring – Load Tests on the Felsenau Viaduct (CH), in *Proc. of the XXth ISPRS Congress*. 3–11 July 2008, Beijing, China.

Received 24 March 2014; accepted 1 December 2014

Mill, T., Ellmann, A., Aavik, A., Horemuz, M. and Sillamäe, S. (2014). Determining ranges and spatial distribution of road frost heave by terrestrial laser scanning. *The Baltic Journal of Road and Bridge Engineering*, 9(3), 227–23



DETERMINING RANGES AND SPATIAL DISTRIBUTION OF ROAD FROST HEAVE BY TERRESTRIAL LASER SCANNING

Tarvo Mill¹✉, Artu Ellmann², Andrus Aavik³, Milan Horemuz⁴, Sven Sillamäe⁵

^{1,2,3}Dept of Road Engineering, Tallinn University of Technology, Ehitajate tee 5, 19086 Tallinn, Estonia

⁴Dept of Geodesy and Geoinformatics, Royal Institute of Technology, Drottning Kristinas väg 30, 10044 Stockholm, Sweden

⁵Faculty of Construction, Tallinn University of Applied Sciences, Pärnu mnt 62, 10135 Tallinn, Estonia

E-mails: ¹tarvo@tktk.ee; ²artu.ellmann@ttu.ee; ³andrus.aavik@ttu.ee; ⁴milan.horemuz@abe.kth.se;

⁵sven@tktk.ee

Abstract. The technology of terrestrial laser scanning has evolved rapidly in recent years and it has been used in various applications, including monitoring vertical and horizontal displacements of constructions but significantly less in road frost heave assessment. Frost heave is categorised as one of the main causes of pavement surface damage in seasonal frost regions. Frost heave occurs in wintertime and in early spring at the freezing process of the ground supported structures such as roads. The major change in the structure is the increase of soil volume due to freezing of its water content. This contribution assesses vertical displacements caused by frost heave on a road using novel terrestrial laser scanning technology. The study emphasises on benefits using the technology in determining accurate magnitudes and spatial distribution of frost heave of roads. The results of case study revealed uneven spatial distribution of frost heave, which may also be an evidence of relatively poor road design quality. Therefore it is also advisable using terrestrial laser scanning in applications such as quality assessment of existing roads and in the pre-reconstruction design stage for detecting any frost heave sensitive areas in existing embankments.

Keywords: terrestrial laser scanning, levelling, frost heave, road condition measurement, pavement surface, embankment.

1. Introduction

Since the beginning of the rapid development of terrestrial laser scanning (TLS) technology in the late 1990-ies it has been used in various projects including deformation monitoring. Deformation monitoring by TLS has been reported by different authors, e.g. Tsakiri and Pfeifer (2006), Zogg and Ingensand (2008), Riveiroa *et al.* (2013). While conventional geodetic technologies focus on collecting sample data of an object with spatial resolution of some meters (depending on the object) the TLS technology captures the complete field of view with a cm range spatial resolution (e.g. Paeglitis *et al.* 2013). A thorough overview of TLS technology is presented in Reshetyuk (2009) and Vosselman and Maas (2009). The quality analysis of TLS is studied by e.g. Reshetyuk (2010) and Lichti (2010).

Occurrence of frost heave has always been a crucial indicator of the quality of the road embankment in seasonal frost regions. It is acceptable for the pavement surface of the road to rise evenly during a sustained cold period (when temperatures are mostly below freezing point)

and settle during a sustained warm period. For instance, according to *Elastsete teekatendite projekteerimise juhend (Guide for the Design of Elastic Pavements)* issued by the Estonian Road Administration in 2001, the allowed maximum range of the vertical raise of the pavement surface for asphalt concrete pavements is 40 mm, for light pavements and gravel roads with surface dressing 60 mm and for gravel pavements 100 mm. In such seasonal frost regions where temperatures fluctuate much around 0 °C in late autumn/early winter and the yearly average temperature is around +5 °C the amount of rainfall usually exceeds evaporation. That leads to higher moisture content in the soil and also in the road embankment, resulting in a weakening of the load bearing capacity during the period when the road structure is not yet frozen and the subsequent promotion of frost heave during the freezing period. The reduced load bearing capacity and deformations due to frost heave usually lead to traffic restrictions in spring as well as the risk of road pavement surface damage. The effects of uneven frost heave and road pavement

surface damages affect considerably traffic safety and driving comfort which also has an economical effect both to the road users and road maintenance.

Frost heave assessment of roads can be conducted by using geometric levelling (e.g. Aavik et al. 2013). The work usually includes profile-wise embedding permanent benchmarks with pre-defined intervals in the longitudinal direction of the pavement surface of the road and then conducting surveys at certain time-epochs (Mroczkowski 2009). The levelling results illustrate the vertical displacements of the road surface but the data have relatively poor spatial resolution (several tens of meters). Alternatively, the effects of frost heave can be assessed by using mobile terrestrial laser scanning (MTLS) and ground penetrating radar (GPR) see e.g. Peltoniemi-Taivalkoski and Saarenketo (2012). MTLS and GPR are cost effective and better suited for analyzing longer road sections (e.g. Thodesen et al. 2012). The MTLS accuracy however, is normally no better than 10 mm due to complexity of height determination by combining Global Navigation Satellite System (GNSS) and Inertial Measurement Unit (IMU) data. To overcome the problems of data generalization in levelling and aiming at observing shorter sections of roads with accuracies better than 10 mm this study tests novel TLS technology for assessing the frost heave induced vertical displacements. To our present knowledge no other studies on the usage of TLS for determining the occurrence and the extent of road frost heave have been published, yet. In addition, also the TLS economic viability and accuracy for this task is discussed. The used methods and results with key features are described as follows. The introduction is followed by explanation of causes of road deformations. The third section gives an overview of geodetic monitoring technology. The fourth section describes the case study, design of the deformation monitoring, establishing the reference network, TLS data acquisition. The data post processing procedures are described briefly in the fifth section. The frost heave results in a test road are presented in the sixth section. Conclusions and discussions conclude the paper.

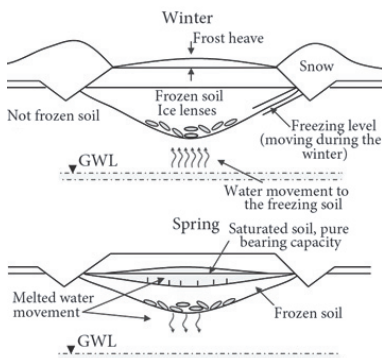


Fig. 1. Frost heave formation in winter (upper figure) and thawing process in spring (lower figure) (Rahiala et al. 1988). GWL denotes ground water level

2. Causes of deformations of roads

Road surfaces are subjected to continuous stress of unbalanced loads caused by vehicles moving on it. The main role of the road pavement is to bear the loads originating directly from the wheels of vehicles and distribute them to the embankment, which withstands the stresses caused by the traffic load. Pavement distortions may in part be attributed to human-made mistakes at road construction, such as the use of inappropriate materials, making a layer too thin or leaving out a layer, insufficient compaction, etc. (Mroczkowski 2009).

However, it is the unbalanced deformation of the embankment that has the most adverse influence on the pavement surface shape. According to Mroczkowski (2009) the most common causes of such a deformation include:

- geological diversity of the embankment;
- embankment movements caused by soil loss due to a faulty drainage system, incorrect support of slopes;
- an existing road failing to provide adequate support of the earthwork;
- ground movement connected with desiccation by trees;
- contractions or expansions of an argillaceous bed connected with the embankment's moisture content;
- a change of the ground water level caused by floods, draining or irrigation works.

The main factors underlying the seasonal climatic influence on the road structure are temperature fluctuations, moisture and freezing conditions. Three factors lead to the formation of frost heave: (i) soil that is frost-susceptible, (ii) a freezing depth that reaches the soil, (iii) the presence of moisture (water) in the soil (high ground water level). If one of the factors is missing, the frost heave will not appear or will be limited.

The freezing of the road structure is divided into two phases: first, simple freezing, when the pavement is beginning to freeze and the freezing depth is gradually increasing; second, frost heave formation, when the soil is beginning to freeze, leading to the increase of its volume due to the expansion of frozen water and formation of ice lenses, leading finally to the rising of the pavement surface (Fig. 1).

During the spring the thawing process starts from the top of the pavement. At the same time the lower parts of the pavement and sub-base soil are still frozen. As a result, melted water does not have the possibility to flow out of the pavement structure, and the load-bearing capacity of the saturated structure decreases causing pavement deterioration (cracking, crazing, and rutting) under the traffic load (Fig. 1). Frost heave will disappear after the soil embedded ice has melted.

Frost heave may yield longitudinal cracks in the middle of the roadway (Fig. 2). However, frost heave induced cracks can appear also in other areas of the pavement. Those cracks can occur due to irregularities in the road structure. Road structures are traditionally constructed in layers and each soil/material used in corresponding layer has to have homogenous properties across the whole transverse and longitudinal profile of the road. In the case

of inhomogeneous properties of the layer (e.g. due to different soil/material types are used in the same layer), those layers due to their different clay and silt content can behave differently during freezing and thus can cause variable magnitude of the frost heave on the pavement surface, which will lead to the appearance of cracks on the transitional area of soil/material properties.

Some of these conditions, which result in the occurrence of frost heave can be determined and eliminated during the reconstruction design of an existing road using geodetic methods described below.

3. Review of geodetic monitoring technology

This section gives an overview of two different techniques to acquire height information of a road pavement surface. Traditionally for road deformation monitoring solely geometric levelling has been used for determining the heights of pre-installed deformation benchmarks in the pavement. Using just levelling in such application is relatively time-consuming, especially in cases of large number of deformation survey points. Novel TLS technology, however, enables to acquire a large (up to millions) number of points within seconds. Though levelling is time-consuming it has yet no alternative for sub-mm accurate height determination. This case study uses geometric levelling for height reference and for verifying deformation monitoring results obtained by the TLS technology.

3.1. Geometric levelling

Geometric levelling is the most precise method for obtaining elevations of ground points. In geometric levelling the height difference between two points is determined by the differences of the levelling staff (placed on top of the involved points) readings.

In deformation monitoring an optical levelling instrument with a built-in compensator (with typical standard deviation of 2.0...3.0 mm/km for double run levelling route) can be used. To minimize the possibility of errors by incorrect staff readings, an electronic levelling instrument with a code staff could be used. For fulfilling more rigorous accuracy requirements an optical levelling instrument with a parallel plate micrometer or a precise electronic level with special invar bar staffs should be used in order to achieve accuracy up to 0.3 mm/km for double run levelling route.

For determination of road deformations permanent levelling benchmarks are usually installed in the form of profiles (minimum three points – two at the side of the road and one in the centre) in the longitudinal direction spacing up to a few dozens of meters, depending on resources available.

3.2. Terrestrial laser scanning

In principle TLS operate similarly as reflectorless total stations, which measure simultaneously horizontal and vertical angles and the range to objects of interest without the need of placing a reflector at those points. Nowadays many scanners are equipped with total station-like functions such as centring over a known geodetic reference point, determining the instrument orientation to the backsight target or

by calculating the position and the height of the instrument by resection. A detailed overview of TLS technology and orientation methods is given in Alba and Scaioni (2007).

Based on the scanning technology, TLS devices are divided into two types: triangulation scanners and time of flight (TOF) scanners. Whereas triangulation scanners are mainly short-range (< 25 m) devices, nonetheless triangulation scanners have very high accuracies in the order of tenth of millimetres. In terms of working principles TOF scanners apply either the pulse modulation method (also known as the direct time-of-flight method) or the amplitude modulation continuous wave method (AMCW, also known as the phase shift method). In the pulse modulation method the travelling time of a single pulse reflected from the target is measured. Typical pulse modulation laser scanners measure up to 50 000 points/s in ranges up to several hundred meters with the range accuracy of 4 mm to 10 mm. In the amplitude modulation method the phase difference between the sine modulated transmitted and reflected waves are measured. This method allows faster measuring, up to 1 000 000 points/s typically within ranges under 100 m with the range accuracy of 2 mm to 5 mm. Due to decreasing intensity of the amplitude modulated waves the phase shift cannot be reliably detected for longer ranges.

In general, the TLS instruments are optimized for a fast and automated data acquisition in ranges typically from one to few hundreds of meters. The acquired data forms a point cloud of n observations where each point holds 3D coordinates (x_i, y_i, z_i) , $i = 1, \dots, n$ in the scanner's intrinsic coordinate system, provided that the scanner's axes (vertical and horizontal axis) are perfectly aligned. The scanners intrinsic coordinates of the survey points are computed from the measured spherical polar coordinates as follows:

$$\begin{bmatrix} x_i \\ y_i \\ z_i \end{bmatrix} = \begin{bmatrix} \rho_i \sin \varphi_i \sin \theta_i \\ \rho_i \sin \varphi_i \cos \theta_i \\ \rho_i \cos \varphi_i \end{bmatrix}, \quad (1)$$

where θ_i – the horizontal angle with respect to initial direction; φ_i – is the zenith angle; ρ_i – the slope distance from the scanner to the object surface.

The scanned data points are tagged also with an uncalibrated intensity (I) value of the reflected signal. In addition, scanners equipped with a digital photo camera enable to assign the RGB values to survey points during the post-processing. Thus an i -th TLS survey point is characterized by the following data string:

$$\{(x_i, y_i, z_i, I(x_i, y_i, z_i), RGB(x_i, y_i, z_i)), i = 1, \dots, n\}, \quad (2)$$

where x_i, y_i, z_i – the coordinates, $I(x_i, y_i, z_i)$ is the intensity; $RGB(x_i, y_i, z_i)$ – the colour code.

The transformation of the intrinsic coordinates (x_i, y_i, z_i) , $i = 1, \dots, n$ of an individual i -th survey point into extrinsic (e.g. national) coordinate system (x_i^E, y_i^E, z_i^E) , $i = 1, \dots, n$ (also known as georeferencing) is described as follows:

$$\begin{bmatrix} x_i^E \\ y_i^E \\ z_i^E \end{bmatrix} = \begin{bmatrix} x_S^E \\ y_S^E \\ z_S^E \end{bmatrix} + \mathbf{R}_3(\kappa)\mathbf{R}_2(\phi)\mathbf{R}_1(\omega) \begin{bmatrix} x_i \\ y_i \\ z_i \end{bmatrix} \quad (3)$$

where (x_S^E, y_S^E, z_S^E) – the coordinates of the centre of the laser scanner expressed in the extrinsic system. $\mathbf{R}_1(\omega)$, $\mathbf{R}_2(\phi)$, $\mathbf{R}_3(\kappa)$ are the matrices for rotation around the x -, y - and z -axes respectively; (ω, ϕ, κ) are the rotation angles (from the scanners intrinsic coordinate system into extrinsic coordinate system) about the x -, y - and z -coordinate axes, respectively:

$$\mathbf{R}_1(\omega) = \begin{bmatrix} 1 & 0 & 0 \\ 0 & \cos \omega & \sin \omega \\ 0 & -\sin \omega & \cos \omega \end{bmatrix} \quad (4)$$

$$\mathbf{R}_2(\phi) = \begin{bmatrix} \cos \phi & 0 & -\sin \phi \\ 0 & 1 & 0 \\ \sin \phi & 0 & \cos \phi \end{bmatrix} \quad (5)$$

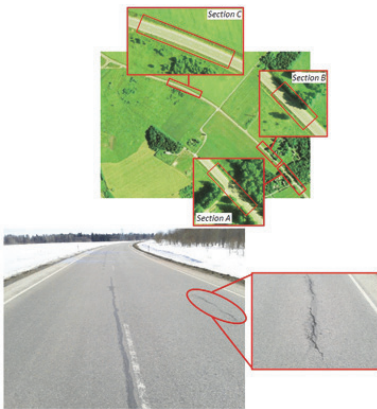


Fig. 2. Road sections A, B and C (left hand side); note longitudinal cracks in the centre and on a road side at the section C (right hand side)

Table 1. Description of the pavement design

Pavement layer (ordered from top to bottom)	Layer thickness
Top layer. Asphalt concrete (in two layers)	8 cm
Base layer of limestone rubble (fraction 16/32, wedged with fraction 8/12). Also the designer allowed using milled asphalt (not over 2 cm thick) for binding the upper layer of the base	20 cm
Drainage layer, filtration module > 2.0 m (in some cases 3.0 m) per 24 h	Average thickness 24 cm, minimal thickness 20 cm
Bottom layer. Fine sand, filtration module > 1.0 m per 24 h	Minimal 40 cm

$$\mathbf{R}_3(\kappa) = \begin{bmatrix} \cos \kappa & \sin \kappa & 0 \\ -\sin \kappa & \cos \kappa & 0 \\ 0 & 0 & 1 \end{bmatrix} \quad (6)$$

If the scanner is equipped with a dual-axis compensator, then the instrument's z -axis (coincides with the plumb-line) is parallel with the extrinsic system's z -axis. In this case the rotation angles ω and ϕ become to zero, i.e. \mathbf{R}_1 , \mathbf{R}_2 in Eq. (3) become equal to the unit matrix. Thus, a turn around the z -axis would be sufficient for georeferencing see section 5.

4. The case study

4.1. General description of the test road

The case study includes three road sections on the Vaida-Urge road T-11202, in northern part of Estonia. The road was fully reconstructed in 2008, but already in spring 2010 pavement damages were detected. The pavement had longitudinal cracks mainly in the centre of the road and in some places on the road sides (Fig. 2). Although the cracks were repaired by filling them with bitumen, they have occurred again. The cause of these cracks may be connected with the road's last reconstruction. The road had been widened without removing the existing embankment. The cracks emerged at the transition boundaries between the existing embankment layers and the new ones. The major negative influence to the road pavement is also the relatively high level of ground water level, primarily within the A and B sections. Obviously, this in conjunction with non-compatible materials contributes to the effects of frost heave. Frost heave is expected, since Estonia lies in the seasonal frost region, where the frost season begins in late November and ends in April. The average temperature in February, the coldest month, is usually around -5°C , in some periods within the winter season far below zero, about -20°C or even lower. According to the Estonian Environment Agency the average temperature for the entire 2012/2013 winter season was -5°C , which is somewhat colder than the seasonal average (-3°C). Due to the fact that roads are kept free of snow during the entire winter, according to *Elastsete teekatendite projekteerimise juhend (Guide for the Design of Elastic Pavements)* issued by the Estonian Road Administration in 2001 the depth of embankment freezing could reach to the depth of 1.25 m.

The road design followed the class IV road parameters, which are based on a 43 standard axle load (100 kN) frequency per 24 h as defined by the regulation *Tee projekteerimise normid ja nõuded (Standards and requirements for road design in Estonia)*, the class IV road parameters, which are based on a 43 standard axle load (100 kN) frequency per 24 h. The description of the designed pavement is reviewed in Table 1.

4.2. Overview of the road conditions

Presumably, the cracks in sections A and B are mainly caused by frost heave. The load bearing capacity of sections A and B were tested using a falling weight deflectometer

(FWD). The load test results were compared with the results of tests on other parts of the same road. The comparison showed that sections A and B had the lowest load bearing capacity values. According to a technical report by Sillamäe, S. 2013. *T-11202 Vaida-Urge tee defektide põhjuste kindlakstegemine (T-11202 Vaida-Urge Road the Identification of Causes of Defects in the Road)*, the elasticity modulus of the A and B sections was 220 MPa, while the average elasticity modulus for the other sections was in average 253 MPa. Recall that the load bearing capacity of a road is affected by various factors, such as the type of sub-soil, soil moisture content, embankment layer material used, etc. The road sections A and B had shallow ditches, whereas the area near the road was covered with hydrophytic plants. The conditions thus indicate a soil with high moisture content.

The C section of the road is superelevated due to its location at a curve. The cracks in the pavement may be the result of different factors, such as pavement creep deformation, slope creep or frost heave. The core samples taken from the C road section indicate the usage of gravelly clayey sands (fine particle content approx 30% only) instead of fine sand, as prescribed by the reconstruction design instructions. Gravelly clayey sand exhibits less adhesion than fine sand, thus allowing the occurrence of creep deformation. Therefore, the upper layer of the surface of the embankment may have deformed due to traffic load, thus leading to the formation of cracks. It is also likely that due to the poor filtration module of the sand, the moisture content in that layer has contributed to occurrence of frost heave.

4.3. Design of the deformation monitoring

This section reviews the applied geodetic monitoring procedures. First, height reference for the road deformation monitoring was established and measured before the road surface scannings. These were carried out in two epochs:

- at the above zero temperatures in November 2012 (fall);
- at the time of expected frost heave maximum during the snow thawing period in April 2013 (spring).

The aim of this work is to assess the range and spatial distribution of frost heave with sub-centimetre accuracy using TLS technology.

4.3.1. Establishment of the height reference

The height reference for the frost heave (ΔH_{heave}) assessment was established using geometric levelling.

The height reference consisted of five benchmarks embedded into the surface of the road pavement (Fig. 3). The height reference was connected to a single geodetic reference point no 324, the normal height of which is known. The centre of this geodetic point is a 0.77 m long steel rod with a cone-shaped anchor at the bottom. The top of the reference point is approx 0.25–0.30 m below the ground surface (Fig. 4).

The double-run geometric levelling was proceeded with an electronic level Leica Sprinter 100 (allowing for height determination standard deviation as of 2.0 mm/km) with two standard aluminium staffs. The forth and back

sights during the levelling were kept equal and two readings were taken at each staff.

The disclosures of the 1.15 km long closed (forth and back) levelling route were +0.0124 m and –0.0012 m, for fall and spring measurements, respectively. These disclosures were further adjusted. Thus, the heights of the reference points are sufficiently accurate for achieving the aim of the work.

The heights of the reference points indicate an overall rise of the pavement surface with respect to the initial geodetic point. The maximum rise is +0.0621 m (cf. Table 2).

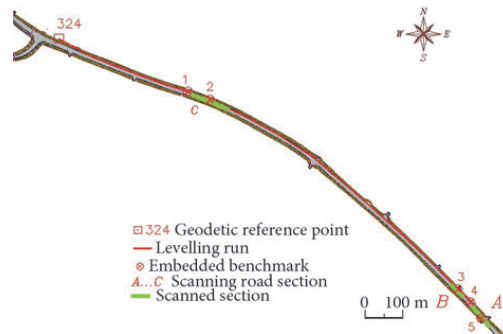


Fig. 3. Locations of the scanned areas (depicted in green) and the levelling benchmarks. Section A was scanned from benchmark 5; section B was scanned from benchmark 3; section C was scanned from benchmark 2; benchmarks 4 and 1 were used as targets for the orientation of the scans

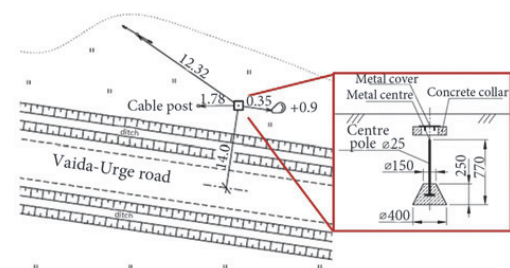


Fig. 4. Location and the design of the used initial geodetic point (Riigi Maa-amet 2013. *Geodeetiliste punktide andmekogu kaardirakendus* [Estonian Land Board. Geodetic Data Map Application])

Table 2. The levelled heights of embedded benchmarks with respect to the used initial geodetic point

Benchmark number	Results in fall 2012, m	Results in spring 2013, m	Differences (i.e. the frost heave): spring minus fall, m
1	48.1062	48.1402	+0.0340
2	48.4046	48.4150	+0.0104
3	50.9743	51.0200	+0.0457
4	50.9955	51.0354	+0.0399
5	50.9752	51.0373	+0.0621

The geometric levelling results will be used as references for TLS survey and to verify the accuracy of TLS results of this study. Verifications of the TLS accuracy at roadworks by total station surveying have earlier been studied, e.g. by Mill *et al.* (2011). The stability of the initial geodetic point (no. 324) was not specially verified. Therefore there is a mild risk of the geodetic point to rise due to frost heave as well since the point is at the depth of only in about one meter in the soil. Note however, that due to thick snow cover in the surroundings of the point during the winter it is unlikely that the frost would reach beneath the geodetic point's anchor. Therefore in further calculations it is assumed that used geodetic point is practically stable.

4.3.2. Terrestrial laser scanning of the road sections

The TLS survey was conducted immediately after levelling of the height reference points. A TOF terrestrial laser scanner Leica ScanStation C10 (equipped with dual-axis compensator) was used for the measurements. The maximum measuring range of the device is 300 m with a $360 \times 270^\circ$ field of view and maximum scanning rate of up to 50 000 points/s. The range and angle accuracy specifications are ± 4 mm and $\pm 12''$, respectively. The scanner was erected and centered above the benchmarks 2, 3 and 5. The height of the scanner z_{TLS} with respect to the initial geodetic point is determined as:

$$z_{TLS} = z_b + H_{TLS} \quad (7)$$

where z_b – the levelled height of the benchmark; H_{TLS} – the tape measured height of the instrument above the benchmark. The spatial resolution for scanning was set to 10 cm at 100 m which defines the vertical and horizontal point spacing on a vertical surface perpendicular to the line of sight. The resulting average point density on the



Fig. 5. Scanning the road section A in April 2013. Note thawing snow along road sides

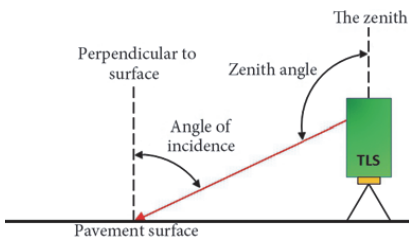


Fig. 6. Angle of incidence at scanning, the red line indicates the laser beam

(horizontal) road surface was in average approx 12 cm, being less dense at longer distances from scanner.

The first scanning epoch was proceeded in fall. The temperature was $+1^\circ\text{C}$, the humidity, 98%, and the wind speed, 3 m/s during the measurements. The pavement surface was wet, making the conditions for laser scanning unfavourable due to possible signal attenuation. The second scanning epoch was proceeded in spring. The temperature was $+4^\circ\text{C}$, the humidity, 33%, and the wind speed, 3 m/s during the measurements. The road was dry, and conditions for scanning were almost ideal, though snow piles still banked the sides of the road. However, the water from the thawing snow prevented data acquisition alongside of the A section, therefore the survey data from the near sides of the pavement (Fig. 5) were excluded from further comparisons.

Lichti (2007) and Soudarissanane *et al.* (2007) suggest that the scanning incidence angle (Fig. 6) should not exceed $65\text{--}80^\circ$. Soudarissanane *et al.* (2011) states that larger incidence angles result approximately 20% of the signal deterioration. The signal deterioration causes the increase of noise in the point cloud, and therefore yields substantially larger standard deviation values (Soudarissanane *et al.* 2011). Since the scanning object was the horizontal road surface the scanner was erected as high as possible (Table 3, column 2) to minimize incidence angle values. At longer scanning distances the incidence angles neared 90° , though.

At such larger incidence angles the angular precision determines primarily the precision of the height of the scanned points. The law of error propagation is used to compute the precision of the height of the scanned point:

$$\sigma^2(\hat{H}) = \sum_{i=1}^n \left(\frac{\partial f}{\partial w_i} \right)^2 \sigma^2(w_i) \quad (8)$$

where $\sigma^2(\hat{H})$ denotes the variance of the road surface height determined by TLS with respect to the initial geodetic point. Note that \hat{H} is an estimate of the actual height H stemming from the levelling, tape-measured scanner height, the TLS range and angle measurements (Eq (9)), f is the function $H = f(w_i)$, $i = 1, \dots, n$, relating the observations (w_i) , $i = 1, \dots, n$, and the height. The notation \hat{H} represents height in order to distinguish it from the scanner z -coordinate. $\sigma^2(w_i)$ is the error of an i -th observable. The observation equation, i.e. function f for an i -th scanned road point is written as (Fig. 7, Eqs (1) and (7)):

$$\hat{H}_i = z_b + H_{TLS} + \rho_i \cos \varphi_i \quad (9)$$

where ρ_i – slope distance from the scanning station to the reflective surface; φ_i – zenith angle; \hat{H}_i – the resulting road surface height. Inserting Eq (9) into Eq (8) and calculating the derivatives the standard uncertainty $\sigma(\hat{H})$ of a survey point height is found as:

$$\sigma(\hat{H}) = \pm \left[\sigma^2(\hat{z}_b) + \sigma^2(\hat{H}_{TLS}) + \frac{1}{(\cos \varphi_i)^2 \cdot \sigma_{dist}^2 + \rho_i^2 \sin^2 \varphi_i \cdot \sigma_{angle}^2} \right]^{1/2} \quad (10)$$

where $\sigma^2(\hat{z}_b)$ – the estimated uncertainty of the benchmark height determined by levelling (2.0 mm/km by specifications, recall, also, that disclosures of levellings in fall and in spring were + 0.0124 m and – 0.00120 m, respectively, thus, in the worst case scenario the benchmark error could contribute up to 3 mm only); $\sigma^2(H_{TLS})$ – the estimated variance of the tape measured height of the instrument (the corresponding error would not exceed 2 mm, at most); σ_{dist} – the scanner’s standard distance uncertainty; σ_{angle} – the scanner’s standard angular uncertainty. Numerical values for σ_{dist} and σ_{angle} were taken from the manufacturer’s specifications (see above). Since $\sigma(\hat{H})$ depends on the distance ρ_i and angle φ_i , then it is individual for each surface point.

The standard uncertainties $\sigma(\hat{H})$ for the road survey points were calculated at four standard locations at 5 m, 10 m, 25 m and 50 m from TLS station (Table 3).

The mean value of standard uncertainties of height $\sigma(\hat{H})$ of the survey points at different locations equals ± 4.0 mm (one sigma), which by adopting the 95% confidence interval level (two sigma) yields an uncertainty of ± 8.0 mm. Thus the uncertainty of two compared data sets (fall and spring) equals to $8.0\sqrt{2} = \pm 11.3$ mm. Hence, height differences exceeding ± 11.3 mm between two TLS epochs at a location is considered as actual deformation (Fig. 7).

4.4. Verification of the TLS survey heights

When scanning the road sections (both in fall and spring) a specially designed 7.62×7.62 cm HDS (High Definition Survey) target was placed onto one of the embedded benchmarks (Fig. 7). A target was scanned from each TLS station. Since the height of the target above the benchmarks was measured, then this allowed determining the benchmark height from the TLS data. The TLS results are then compared with levelled results and the corresponding discrepancies are presented in Table 4. Larger discrepancies (in road section A) are associated with the target on the benchmark number 4 (Table 4). The discrepancies are likely either due to non-verticality of the target or measuring the target height or scanning the targets or a combination of aforementioned errors. The RMS-error value as of ± 2.9 mm was calculated by using all discrepancies in the last column of Table 4.

The resulting RMS uncertainty value agrees reasonably with the theoretical TLS uncertainty (section 4.3.2.).

The actual discrepancies differ from the estimated one (8.0 mm, at 95% confidence interval level) by 5.1 mm. The latter indicates that the achieved uncertainty is substantially better than the theoretical uncertainty (section 4.3.2.).

5. Laser scanning data processing

TLS data processing was divided into two phases. At first, the 3D point cloud was processed by using commercial Leica Cyclone 8.0 software, where information outside the object of interest was removed and 3D TIN models of the road sections were created and compared. Second, the Autodesk AutoCAD Civil 3D 2013 software was used to analyse the results (see section 6).

The laser scanings were proceeded in an arbitrary coordinate system. For the fall and spring TLS surveys the origins of the x and y coordinates coincided exactly (recall, that in both occasions the scanner was centred above the same benchmark). However, the directions of coordinate (x, y) axis were shifted with respect to each other. The orientation

Table 3. Height uncertainties at four standard locations

Point number	Height of the TLS H_{TLS} , m	Slope distance ρ , m	Zenith angle φ , °	Standard uncertainties $\sigma(H)$, m
1	2.0	5	111°48'	0.0039
2	2.0	10	101°19'	0.0037
3	2.0	25	94°34'	0.0039
4	2.0	50	92°17'	0.0046

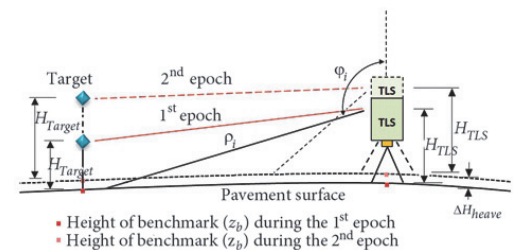


Fig. 7. Scanning of a road section in two epochs, the red and black lines indicate the laser beams reflecting back from targets and from the road surface, respectively. The used symbols are explained in the text

Table 4. Heights of the benchmarks obtained from TLS data and levelling

Road section	Epoch	Benchmark number	Height of target H_{Target} , m	Heights from TLS data in m, reduced from the target centre	Heights from levelling in m, source Table 2	Discrepancies, m
A	fall	4	1.900	50.989	50.995	-0.006
	spring	4	1.900	51.036	51.035	+0.001
B	fall	4	0.700	50.997	50.995	+0.002
	spring	4	1.900	51.032	51.035	-0.003
C	fall	1	0.700	48.106	48.106	+0.000
	spring	1	0.200	48.140	48.140	+0.000

of the coordinate axis of the point clouds were conducted at the post processing in Leica Cyclone. First, the point cloud's x -axis was defined by the scanner location and the target placed above one of the benchmark (Fig. 8). Thereafter the benchmark-target direction (denoted as x' in Fig. 8) of the fall measurements was rotated (around the z -axis) to coincide with the post processing x -axis. Then the benchmark-target direction (denoted as x'' axis in Fig. 8) of the spring measurements was rotated (around the z -axis) to coincide with the post processing x -axis as well. Such an orientation

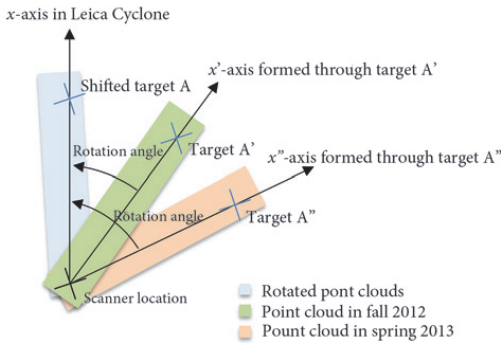


Fig. 8. Merging the fall and spring TLS data through the TLS-target direction. Point clouds of the fall and the spring TLS data are rotated around z -axis using benchmark-target direction. View from the top

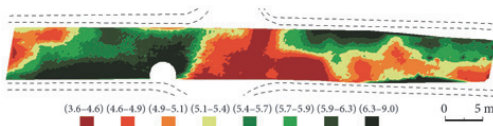


Fig. 9. Frost heave in the road section A in spring 2013. Length of the section 63 m, the non-coloured half-circle indicates the location of the scanner, dashed lines denote roughly the edges of tarmac and the widths of road shoulders, the colour ranges are in cm

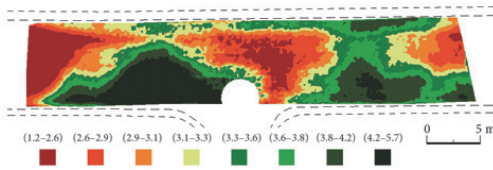


Fig. 10. Frost heave in the road section B in spring 2013. Length of the section 42 m, the circle indicates the location of the scanner, dashed lines denote roughly the edges of tarmac and the widths of road shoulders, colour ranges are in cm

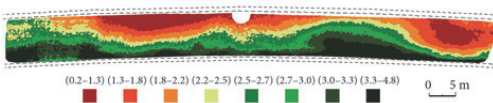


Fig. 11. Frost heave in the road section C in spring 2013. Length of the section 94 m, the non-coloured half-circle indicates the location of the scanner, dashed lines denote roughly the edges of tarmac and the widths of road shoulders, colour ranges are in cm

method was applied to all sections. The heights of point clouds were 1D corrected by the H_{TLS} differences (Fig. 7) in the fall and spring measurements.

The laser-point based centring accuracy of the scanner was estimated to be around ± 1.0 mm. Such centring error has no considerable effects on the results of the study, recall also an average data resolution of approximately 12 cm. Noise from passing cars and other commuters on the surface of the road was removed using an algorithm of smooth surface which segments the points representing the smooth surface from the point cloud. Followed by noise removal 3D TIN models of the road sections were created and compared. The results of the comparison were exported into .txt format and imported into Autodesk AutoCad Civil 3D.

6. Results of frost heave assessment

The surface comparison results were analysed in Autodesk AutoCad Civil 3D by creating comparison surfaces using the imported data-points. The comparison surfaces show height discrepancies from different epochs using eight ranges of colours from dark green to dark red.

Results for road section A indicate clearly the effects of uneven frost heave (Fig. 9) with a minimum surface rise of +3.6 cm in the centre of the road (dark red) and a maximum rise of +9.0 cm at the sides of the road (dark green). The total area investigated was 425.7 m². The greater part of the total area, that is 50%, had risen in the range of +5.1 cm to +6.3 cm; 37% of the area had risen in the range of +3.6 cm to +5.1 cm; and 12% of the area had risen in the range of +6.3 cm to +9.0 cm. The extreme rise of +9.0 cm is only within an area that is less than 1%. This might be caused possibly by an erratic point.

Results from road section B also indicate the effects of uneven frost heave (Fig. 10) with a minimum surface rise of +1.2 cm in the centre of the road and at the left end (dark red) and a maximum rise of +5.7 cm at the sides of the road (dark green). The total area investigated was 311.6 m². Results show that 50% of the total area had risen in the range of +3.1 cm to +4.2 cm; 37% of the area had risen in the range of +1.2 cm to +3.1 cm; and 13% of the area had risen in the range of +4.1 cm to +5.7 cm.

Results from road section C indicate frost heave (Fig. 11) with a minimal surface rise of +0.2 cm on the higher side of the slope (dark red) and a maximum rise of +4.8 cm at the centre of the curve on the lower side of the slope (dark green). The total area investigated was 720.0 m². The results show that 38% of the area had risen in the range of +2.2 cm to +3.0 cm; 37% of the area had risen in the range of +0.2 cm to +2.2 cm; and 25% of the area had risen in the range of +3.0 cm to +4.8 cm.

The results of the laser scanning show vertical deformations up to +9.0 cm on section A, up to +5.7 cm on section B, and up to +4.8 cm on section C. The results obtained clearly indicate frost heave. The study revealed that the frost heave was spread across the road surface in an uneven manner, which is considered an unacceptable behaviour.

Though the incidence angles at scanning were near 90°, they do not appear to affect significantly the

results, since the resulting surfaces were regular over all road sections.

7. Conclusions and discussions

This contribution presented the methodology for collecting and processing data for the purpose of determining magnitudes and spatial distribution of frost heave by terrestrial laser scanning. The data collecting methodology combines the geodetic methods of geometric levelling and terrestrial laser scanning. A complete description of the work carried out on the observed road sections is presented, including the establishment of the height reference, terrestrial laser scanning data acquisition, data processing and the creation of the analyse surfaces. The achieved root mean square error was by verification in fall ± 2.9 mm, where the assumed accuracy was ± 8.0 mm on 95% confidence interval level.

It is difficult and even impossible to provide such high-resolution results by conventional survey methods such as total station survey or geometric levelling thus the ability to detect spatial distribution of frost heave makes laser scanning an effective and attractive tool. The fact that the concerned areas are relatively limited makes the use of terrestrial laser scanning, which by nature is static, cost effective due to its ability to acquire a relatively large amount of data in a short period of time without disruption to traffic.

Problems with terrestrial laser scanning might occur when scanning at below 0 °C temperatures. Although in general such scanners are able operating in mild cold, the accuracy specifications provided by the manufacturers are determined in temperatures above 0 °C, therefore the accuracy of scanning in temperatures below zero is not guaranteed. Another problem with terrestrial laser scanning (and this applies to mobile terrestrial laser scanning as well) is the problem with rubble or debris, even snow on the road surface will distort the acquired data. Using conventional surveying technology such as total station survey or levelling it is possible to eliminate such potential distortions. However the conventional surveying technology has a lower productivity compared to terrestrial or mobile terrestrial laser scanning.

Nevertheless, for future projects it is advisable that terrestrial laser scanning surveys should be accompanied with verifying observations by other geodetic technologies.

A useful benefit of using terrestrial laser scanning surveying in road survey projects would also be the possibility to monitor the road during the guarantee period following construction to verify the quality and stability of the road pavement. In addition, it is also advisable to use terrestrial laser scanning to determine frost heave sensitive areas of the existing road embankment in the pre-reconstruction stage. Determining frost heave sensitive areas in the pre-reconstruction stage would help preclude possible reconstruction design flaws.

Acknowledgements

The Estonian Road Administration is thanked for allowing using the geodetic monitoring data. The used TLS

Leica ScanStation C-10 and the licensed 3D Point Cloud Processing Software Leica Cyclone is purchased within frames of the Estonian Research Infrastructures Roadmap object Estonian Environmental Observatory (funding source 3.2.0304.11-0395, project No. AR12019). Part of this research is supported by the Estonian Environmental Technology R&D Programme KESTA research project ERMAS AR12052.

References

- Aavik, A.; Ellmann, A.; Paabo, P. 2013. Use of Geosynthetics for Roadbase Strengthening – Case Study in Swampy Area, in *The XXVII International Baltic Road Conference*. August 26–28, 2013, Vilnius, Lithuania [cited 12 March 2014]. Available from Internet <http://www.balticroads.org/downloads/28BRC/009_T03.pdf>.
- Alba, M.; Scaioni, M. 2007. Comparison of Techniques for Terrestrial Laser Scanner Data Georeferencing Applied to 3-D Modeling of Cultural Heritage, in *Proc. of the 3D-ARCH 2007: "Virtual Reconstruction and Visualization of Complex Architectures"*, XXXVI-5/W47. July 12–13, 2007, Zurich, Switzerland [cited 20 June 2013]. Available from Internet <http://www.isprs.org/proceedings/XXXVI/5-W47/pdf/alba_scaioni.pdf>.
- Lichti, D. D. 2007. Error Modelling, Calibration and Analysis of an AM–CW Terrestrial Laser Scanner System, *ISPRS Journal of Photogrammetry and Remote Sensing* 61(5): 307–324. <http://dx.doi.org/10.1016/j.isprsjprs.2006.10.004>
- Lichti, D. D. 2010. Terrestrial Laser Scanner Self-Calibration: Correlation Sources and Their Mitigation, *ISPRS Journal of Photogrammetry and Remote Sensing* 65: 93–102. <http://dx.doi.org/10.1016/j.isprsjprs.2009.09.002>
- Mill, T.; Ellmann, A.; Uueküla, K.; Joala, V. 2011. Road Surface Surveying Using Terrestrial Laser Scanner and Total Station Technologies, in *Proc. of 8th International Conference Environmental Engineering*. Ed. by Čygas, D.; Froehner, K. D. May 19–20, 2011 Vilnius, Lithuania. Technika. 1142–1147.
- Mroczkowski, K. 2009. Determining Deformation on the Road Surface, in *Proc. of the IX Konferencja Naukowo-Techniczna „Aktualne problemy w geodezji inżynierskiej”*. March 30–31, 2009, Warsaw, Poland [cited 7 October 2013]. Available from Internet <http://yadda.icm.edu.pl/baztech/element/bwmeta1.element.baztech-article-PWAB-0005-0012/c/httpwww_rog_gik_pw_edu_plphocadownloadnr8732.pdf>.
- Paeglītis, A.; Paeglītis, A.; Vitiņa, I.; Igaune, S. 2013. Study and Renovation of Historical Masonry Arch Bridge, *The Baltic Journal of Road and Bridge Engineering* 8(1): 32–39. <http://dx.doi.org/10.3846/bjrbe.2013.05>
- Peltoniemi-Taivalkoski, A.; Saarenketo, T. 2012. *Drainage Maintenance Follow Up – Experiences from the Rouvaniemi and Kittilä Projects, Finland* [cited 15 September 2013]. Available from Internet <http://www.roadex.org/uploads/publications/drainage/ROADEX_IV_Drainage_Maintenance_Follow_Up_Finland.pdf>.
- Rahiala, J.; Rakennusaineteollisuusyhdistys; Tie- ja vesirakennushallitus; Betonitieprojekti. 1988. *Maabetoni ja betonipäällysteet: ... käytössä maailmalla, sopivatko Suomeen? ...* [Rahiala, J.; Building Materials Industry Association; the Board of Directors of Civil Engineering; Concrete Project.

- Land Concrete and Concrete Coating: ... Used in the World, Whether the Finland?]. (Vol. 275 p.). Turku: Tie- ja vesirakennushallitus. ISBN 951-47-1603-5.
- Reshetyuk, Y. 2009. *Self-Calibration and Direct Georeferencing in Terrestrial*: PhD Thesis 978-91-85539-34-5. Stockholm: Kungliga Tekniska högskolan [Royal Institute of Technology]. Universitetservice US AB [cited 15 January 2010]. Available from Internet <<http://kth.diva-portal.org/smash/record.jsf?pid=diva2:139761>>.
- Reshetyuk, Y. 2010. A Unified Approach to Self-Calibration of Terrestrial Laser Scanners, *ISPRS Journal of Photogrammetry and Remote Sensing* 65(5): 445–456. <http://dx.doi.org/10.1016/j.isprsjprs.2010.05.005>
- Riveiroa, B.; González-Jorgeb, H.; Varelab, M.; Jaureguic, D. 2013. Validation of Terrestrial Laser Scanning and Photogrammetry Techniques, *Measurement* 46(1): 784–794. <http://dx.doi.org/10.1016/j.measurement.2012.09.018>
- Soudarissanane, S.; Lindenbergh, R.; Menenti, M.; Teunissen, P. 2011. Scanning Geometry: Influencing Factor on the Quality of Terrestrial Laser Scanning Points, *ISPRS Journal of Photogrammetry and Remote Sensing* 66(4): 389–399. <http://dx.doi.org/10.1016/j.isprsjprs.2011.01.005>
- Soudarissanane, S.; van Ree, J.; Bucksch, A.; Lindenbergh, R. 2007. Error Budget of Terrestrial Laser Scanning: Influence of the Incidence Angle on the Scan Quality, in *Proc. of the 3D-NordOst 2007*. September 6–7, 2007, Berlin, Germany. [cited 1 June 2013]. Available from Internet <<http://citeseerx.ist.psu.edu/viewdoc/download?doi=10.1.1.149.5378&rep=rep1&type=pdf>>.
- Thodesen, C. C.; Lurfald, O.; Hoff, I. 2012. Review of Asphalt Pavement Evaluation Methods and Current Applications in Norway, *The Baltic Journal of Road and Bridge Engineering* 7(4): 246–252. <http://dx.doi.org/10.3846/bjrbe.2012.33>
- Tsakiri, M. L.; Pfeifer, N. 2006. Terrestrial Laser Scanning for Deformation Monitoring, in *Proc. of the 12th FIG Symposium on Deformation Measurement and 3rd IAG Symposium on Geodesy for Geotechnical and Structural Engineering*. May 22–24, 2006, Baden, Austria [cited 3 April 2013]. Available from Internet <http://www.ipf.tuwien.ac.at/np/Publications/tsakiriLichtiPfeifer_FIG.pdf> .
- Vosselman, G.; Maas, H.-G. 2009. *Airborne and Terrestrial Laser Scanning*. Dunbeath: Whittles publisher. 320 p. ISBN 978-1439827987.
- Zogg, H.-M.; Ingensand, H. 2008. Terrestrial Laser Scanning for Deformation Monitoring – Load Tests on the Felsenau Viaduct (CH), in *Proc. of the XXIVth ISPRS Congress*. July 3–11, 2008, Beijing, China. [cited 15 June 2013]. Available from Internet <<http://www.isprs.org/congresses/beijing2008>>.

Received 23 April 2014; accepted 10 June 2014

Mill, T., Alt, A. and Liias, R. (2013). Combined 3D building surveying techniques - terrestrial laser scanning (TLS) and total station surveying for BIM data management purposes. *Journal of Civil Engineering and Management*, 19, S23–S32.

COMBINED 3D BUILDING SURVEYING TECHNIQUES – TERRESTRIAL LASER SCANNING (TLS) AND TOTAL STATION SURVEYING FOR BIM DATA MANAGEMENT PURPOSES

Tarvo MILL^a, Aivars ALT^b, Roodė LIAS^a

^a*Department of Construction Geodesy, Tallinn University of Technology, Ehitajate tee 5, 19086 Tallinn, Estonia*

^b*Department of Civil Engineering, Tallinn University of Applied Sciences, Pärnu mnt 62, 10135 Tallinn, Estonia*

Received 23 Dec 2012; accepted 8 Apr 2013

Abstract. Building information modelling (BIM) represents the process of development and use of a computer generated model to simulate the planning, design, construction and operation of a building. The utilisation of building information models has increased in recent years due to their economic benefits in design and construction phases and in building management. BIM has been widely applied in the design and construction of new buildings but rarely in the management of existing ones. The point of creating a BIM model for an existing building is to produce accurate information related to the building, including its physical and functional characteristics, geometry and inner spatial relationships. The case study provides a critical appraisal of the process of both collecting accurate survey data using a terrestrial laser scanner combined with a total station and creating a BIM model as the basis of a digital management model. The case study shows that it is possible to detect and define facade damage by integration of the laser scanning point cloud and the creation of the BIM model. The paper will also give an overview of terrestrial laser scanning (TLS), total station surveying, geodetic survey networks and data processing to create a BIM model.

Keywords: terrestrial laser scanning, total station surveying, BIM, building managing.

Reference to this paper should be made as follows: Mill, T.; Alt, A.; Liias, R. 2013. Combined 3D building surveying techniques – terrestrial laser scanning (TLS) and total station surveying for BIM data management purposes, *Journal of Civil Engineering and Management* 19(Supplement 1): S23–S32.
<http://dx.doi.org/10.3846/13923730.2013.795187>

Introduction

Building renovation is a growing trend in the construction sector. The amount and granularity of information needed for renovation design is growing in tandem with the fields of architecture, construction, engineering and building management. We should not overlook the importance of cost efficiency. In order to design cost-efficient renovation works, it is important to have at hand accurate data reflecting the existing situation. This will ultimately be the basis of all design processes and can affect the allocation of costs.

Several studies on the creation of 3D models of existing buildings have been conducted over the last decades. These 3D models have been of great importance to architectural city planning. For example, Donath and Thurow (2007) have suggested an integrated building information system, combined with a digitally supported survey solution for architectural surveying. The study brings out a number of problem

areas mainly concerned with accuracies in presenting building geometry.

Laser scanning with its high level of accuracy and high level of detail is very versatile and has been utilised, for example in the assessment of buildings' condition (Tang, Akinci 2012) and computing accurate parametric models of complex objects (Bauer, Polthier 2009). For example, Haala and Kada (2010) have focused their study on the creation of 3D models of buildings' roofs and facades using 3D terrestrial laser scanning (TLS) data, although Rajala and Penttilä (2006) and Larsen *et al.* (2011) point out that digitalising a building using TLS data entails a high volume of work. In the last few years, point cloud software development has increased the efficiency of point cloud processing and made it more flexible when creating building information modelling (BIM) models. Bosché (2010) has pointed out how geometry created with accurate survey (information-rich) data is related to the

BIM model. Using BIM technology requires in addition to geometric information, other data, such as physical, structural and functional parameters.

The present case study went through the following stages: establishing the external and internal geodetic survey networks, planning and conducting laser scanning of the external part of the building, planning and conducting a total station survey of the internal part of the building. At the end of each stage, data processing was performed, and finally a BIM model was generated.

An unexpected and positive outcome of the case study was the possibility to detect and define facade damage by integration of the laser scanning point cloud and the BIM model created.

1. The case study object

The case study object was the main building of the Tallinna Tehnikakõrgkool/University of Applied Sciences (TTK/UAS) located in the capital city of Estonia. The building, built in the 1950s, was designed and built by the Leningrad architectural institute Giprošaht architect H. Serlin from 1946 to 1953. The building is in the stalinistic style, characterised by an abundance of ornaments.

Over the years, the building has been renovated and expanded numerous times. Since few of the original architectural drawings are extant, the daily administrative work has been carried out using hard-copy 2D inventory plans, some of which were made in 1975. The main problem with inventory plans is that often they do not coincide with reality. The situation is similar for existing buildings in Estonia.

In order to simplify the process of administration and planning, it is essential to have reliable and informative spatial data. In this case, the existing data was not sufficient enough to carry out any administrative activity. As a result, a building survey was necessary, either as an extension or validation of existing building documentation or to provide new documentation (Donath, Thurow 2007).

The current state-of-the-art approach to collecting, organising and integrating survey data of an existing building into a single data structure is to model it using BIM tools (Eastman 2008).

2. Concept of BIM

BIM represents the process of development and use of a computer generated model to simulate the planning, design, construction and operation of a building. The resulting model, a building information model, is a data-rich, object-oriented, intelligent and parametric digital representation of the building, from which views and data appropriate to various users' needs can be extracted and analysed to generate information that can be used to make decisions and to improve the

process of delivering the building (Azhar 2011). In order to simplify real-time tracking of projects and information management, the processes can be integrated with different applications like Radio Frequency Identification (RFID) and Geographic Information System (GIS) (Cheng *et al.* 2008). When combining RFID, GIS and BIM, we gain a novel and effective tool with wide application in the Architectural, Engineering and Construction (AEC) industry.

The basic parameters describing vector objects are shape and volume and can be simply expressed as coordinate points and their orientation as an angular value within a 3D space. Specifications for the materials and texture can accompany the numerical data. Parametric CAD differs from generic 3D CAD in that parameters are assigned to an object prior to its use. The 3D object as a parametric model can be edited to revise any or all of its parameters of construction, texture and orientation (CSA 2005).

Architectural CAD has been developed from 2D graphic computer representation to parametric modelling to 3D modelling (Tse *et al.* 2005), and on to feature extraction and finally to BIM.

The leading BIM software platforms are Autodesk Revit, GraphiSoft ArchiCAD and Bentley Architecture. ArchiCAD by Graphisoft (2012) is an architectural design application built around the BIM concept as a standalone application. In ArchiCAD the modelling of objects can be achieved using standard parametric construction elements. These elements are embedded in the software (such as walls, columns, beams, slabs, roofs, etc.) or created as new objects using the embedded scripting language Geometric Descriptive Language (GDL). The use of GDL allows the creation of any number of rich parametric BIM objects and for their storage in internal libraries or data bases for further reuse or modification (Tse *et al.* 2005). Revit (Autodesk Inc. 2012) is also a BIM platform, where the user constructs a mass model with a combination of solid forms and void forms. The faces of the mass volume can be turned into building elements, floors and other architectural elements can be generated inside the mass model. Bentley Architecture's interface is completely different from that of other types of BIM software, in the sense that it is not a standalone application but is a plug-in for Bentley MicroStation TriForma, which in turn is also a plug-in for the fundamental Bentley MicroStation (Tse *et al.* 2005).

3. Review of technology

This section gives an overview of the application of two different techniques to acquire accurate geometric information for a building. Traditionally, a total station is used to record single points. Using a total station, however, is relatively time-consuming since points are recorded one by one. Each survey point describes building edges or points of interest. This

method does not allow the possibility to acquire complex surface structures. In the case of TLS, one scan results in a large quantity of points in a systematic pattern, also called a point cloud. Many different TLS systems are on the market for a wide variety of object sizes, ranges and accuracies. In response to total station survey and TLS, close-range stereo photogrammetry is the predominant method for geometric documentation of a complex consisting of heritage objects. The close-range stereo photogrammetric measurement system consists mainly of a digital camera, a laser distance metre, and a special support for two devices (Ordóñez *et al.* 2010). A more detailed overview of close-range photogrammetry applications is given by Ordóñez *et al.* (2010) and Jiang *et al.* (2008). Boehler and Marbs (2004) give a comparison of TLS and close-range photogrammetry.

3.1. TLS technology

A terrestrial laser scanner scans its entire field of view one point at a time by changing the laser rangefinder's direction of view to scan different points (Mill *et al.* 2011). According to scanning technology, terrestrial laser scanners can be divided into three basic groups: triangulation, time of flight (TOF) and phase-shift (PS) or phase-based (PB).

Triangulation laser scanners shine a laser pattern onto the object and use a camera to look for the location of the laser's projection onto the object (Lerma *et al.* 2010). The pattern projector and the object being measured are configured in a triangle, hence the name triangulation scanner. Triangulation laser scanners are used in applications generally requiring an operating range that is less than 25 m (Mensi 2012). TOF laser scanners compute distances by measuring the time frame between sending a short laser pulse and receiving its reflection from an object. Since the laser pulse travels with a constant speed, the speed of light, the distance between the scanner and the object can be determined. TOF laser scanners can determine up to 50,000 points per second up to a distance of over 1 km from the scanner (Riegl Laser Measurement Systems GmbH 2011).

PB laser scanners avoid using high precision clocks by modulating the power of the laser beam. The emitted (incoherent) light is modulated in amplitude and fired onto a surface. The scattered reflection is collected and a circuit measures the phase difference between the sent and received wave-forms, hence a time delay. This method allows faster measuring, up to 1,000,000 points/s (Zoller + Fröhlich GmbH 2012). Because of the laser power required to modulate the beam to certain frequencies, the range of these scanners are limited to approximately between 25 and 80 m (3D Risk Mapping 2008).

Laser scanning technology possesses many capabilities for gathering data, but certain aspects should

be considered when planning recording tasks. Laser scanning does not provide unlimited geometric accuracy. Scanning accuracy is dependent on the surface material and reflecting capabilities of objects observed. A thorough analysis of laser scanning accuracy has been carried out by Boehler and Marbs (2003), Schulz and Ingesand (2004), Mechelke *et al.* (2007) and Alkan and Karsidag (2012).

3.2. Total station survey technology

Total stations combine electronic theodolites and EDM into a single unit. They digitally observe and record horizontal directions, vertical directions, and slope distances. These digital data observations can be adjusted and transformed to local x - y - z coordinates using an internal or external microprocessor. Various atmospheric corrections, grid and geodetic corrections, and elevation factors can also be entered and applied. The total station may internally perform and save the observations, or (more commonly) these data may be downloaded to an external data collector. With the addition of a data collector, the total station interfaces directly with onboard microprocessors, external PCs, and software (US Army Corps of Engineers 2007). Total stations can electronically encode angles to 1 arc-second with accuracy down to 0.5 arc-second. Distances can be measured with accuracy down to 0.5 mm (Leica Geosystems AG 2012a).

4. The case study

4.1. Workflow

The case study workflow chart is laid out in Figure 1. The workflow chart depicts in detail the stages of the case study. The workflow is divided into five parts.

4.2. Establishment of a geodetic network

The initial phase of the survey project involved establishing a geodetic survey network around the

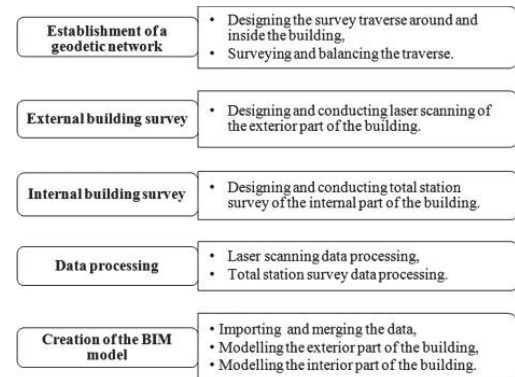


Fig. 1. Workflow of the stages of the case study



Fig. 3. The point cloud of the entire building in Leica Cyclone 7.1

windows, were sometimes measured using an electronic distance metre (Leica Disto A2) depending on the visibility inside the room. Since it was difficult to survey corners accurately, some of the corner positions were created during data processing using the extensions of the walls, where walls intersected.

4.5. Data processing

Data processing was divided into three different phases, the first, exterior point cloud processing, the second, internal total station survey data processing and the third, processing data using BIM software the BIM model of the building was created.

4.5.1. Laser scanning data processing

After the external perimeter of the building was laser scanned, information outside the object of interest was removed from the point cloud using Leica Cyclone 7.3

software. The data was saved in a *.pts format for further processing in Autodesk Revit Structure 2013.

4.5.2. Total station survey data processing

Total station survey data processing was done using Autodesk AutoCAD 2011. First, 2D floor plans at zero height were created. Using the heights of ceilings in rooms, walls were created and since the perimeter was now known, door and window openings were added. Rooms were now simple 3D blocks in the correct plane position. These blocks were then merged onto the correct height of the floor in the 3D building model, as illustrated in Figure 4.

4.6. Creation of the BIM model

4.6.1. Importing and merging the data

The BIM model was created in Revit Structure 2013. Revit Structure 2013 was chosen, because it allows direct import of a point cloud data in common

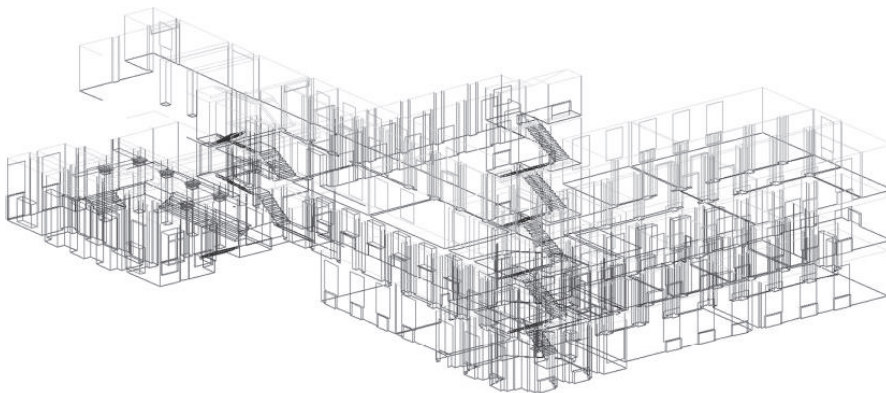


Fig. 4. A fragment of the 3D model of the building in AutoCAD 2011

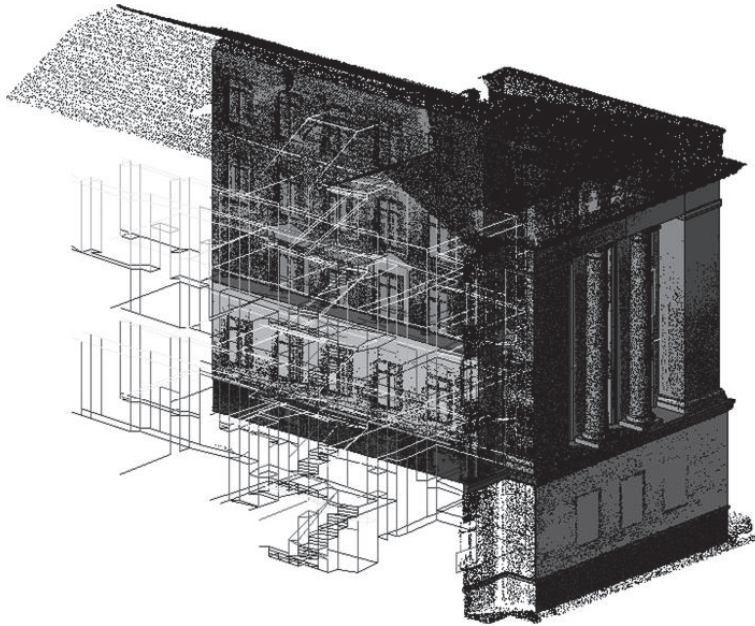


Fig. 5. A sample of the internal 3D model merged with the exterior point cloud

formats like *.pts. The software uses a native *.pcg format, and it is possible to convert the *.pts format to the *.pcg format.

Of equal importance is the possibility to export models in open formats like XML, IFC and DWF. The availability of open file formats can facilitate collaboration in data collecting, data processing and data application. It is worth noting that applications used for viewing, commenting and coordination are based on open file formats.

Since the building was surveyed using two different survey methods to create a model of the whole building, the internal AutoCAD 3D model based on the total station survey and the exterior laser scanning point cloud data (Fig. 5) had to be merged.

4.6.2. Modelling the exterior

The surface of the facade was modelled entirely using the laser scanning point cloud data. Since Revit Structure does not have an algorithm for determining the best fit for the location of the surface of the facade, the modeller chose the location manually. Choosing the right place for the surface manually may turn out to be very difficult, especially if the surface is rough and uneven (see Fig. 6).

The merged dataset is also used for marking the floor heights and axes of the building in Revit (Fig. 7).

Using Revit's commands like columns, walls, slabs, etc. different structural and architectural parts

of the building were created. The procedure described above was used to build up the rest of the model.

4.6.3. Modelling the interior

The taxonomy of the BIM is as follows: the model is divided into separate floors and each floor is divided into building sections according to its logical location.

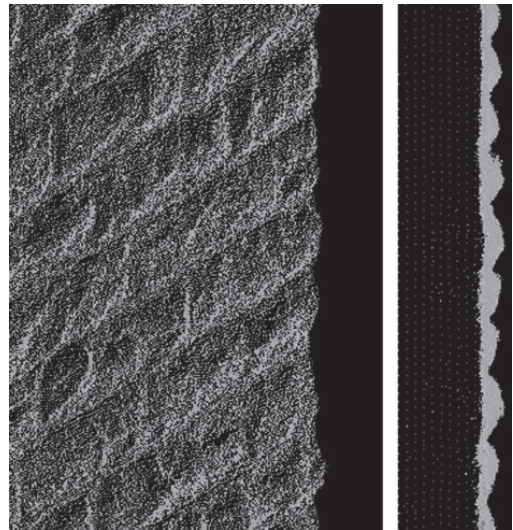


Fig. 6. A sample of the building's limestone facade, front view (left) side view (right)

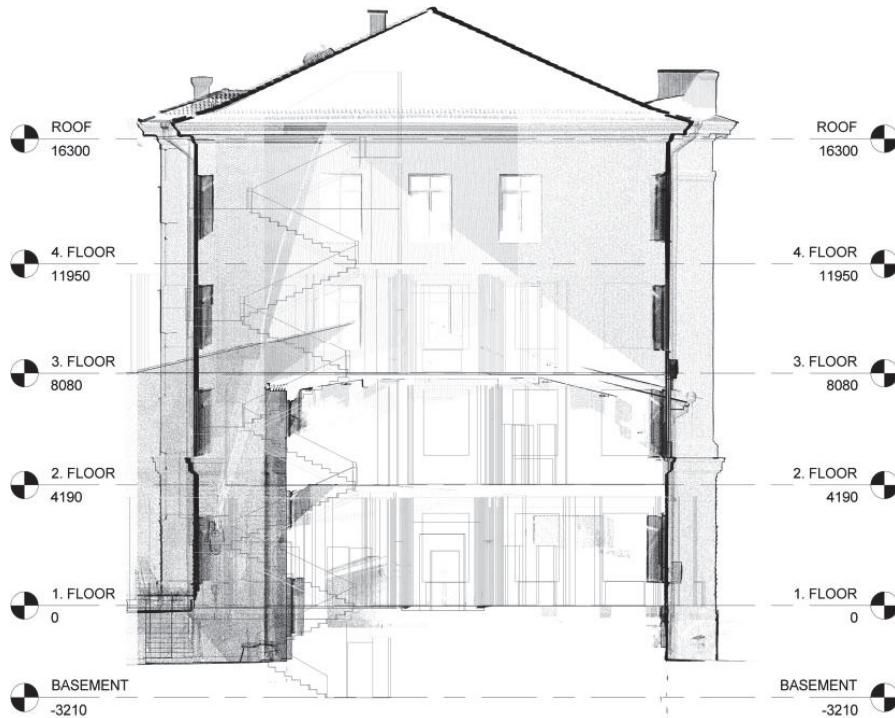


Fig. 7. Combined point cloud data with AutoCAD 3D to fit height marks

The taxonomy was designed according to the principle that it would be possible to display smaller parts of the whole BIM model separately, in turn making it more convenient for the user to work with a specific section or floor. Such an approach would also put less of a load on the computer hardware. Another reason for using smaller sections is that renovation is typically carried out on one room or floor at a time, since the building is in continuous use. For example, renovation of the ventilation system is planned at first only for section A on the first floor. The taxonomy created by the model simplifies the designing for only that part of the ventilation system.

According to the American Institute of Architects (AIA), the level of detail of the model is 300 (Weygant 2011), meaning that the model shows the quantity, shape, size, location and orientation of elements. The inserted elements carry sufficient information concerning the required performance criteria; therefore, a detailed analysis of the construction elements can be performed. For example, a wall structure is modelled in sufficient detail enough to carry out a dynamic energy analysis. As a result, it is possible to simulate different insulation options for outside walls. It can also be checked if the planned ventilation system matches the user profiles of different rooms.

5. The benefits of the creation of a BIM model

Displaying the model created in Revit and the point cloud data simultaneously is an effective way to define the extent of facade damage. Using traditional survey methods to achieve such an objective would have been challenging. An example of facade plaster damage is shown in Figure 8. It is possible to measure the damaged area in the direction needed.

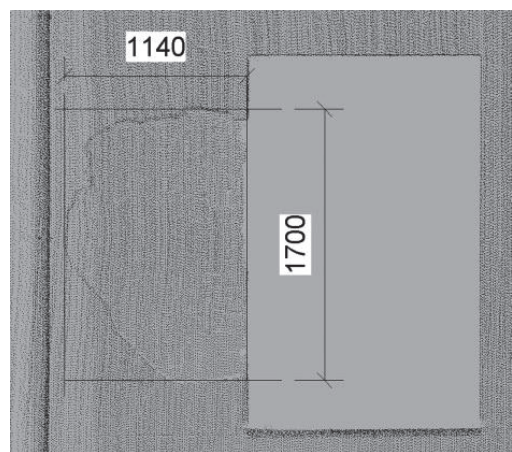


Fig. 8. The damaged facade area dimensions

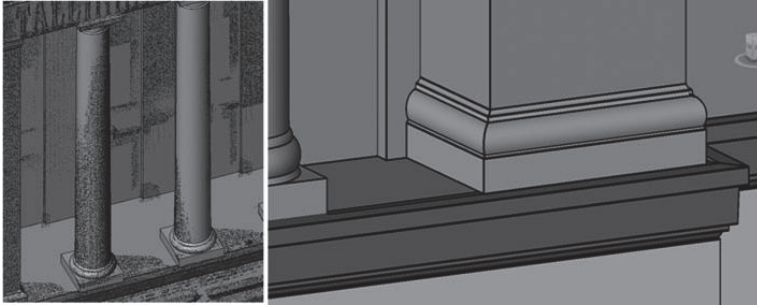


Fig. 9. Columns and ornaments

Tools developed to create models from a point cloud are effective and time saving when modelling complicated but geometrically proportional facade elements like columns or ornaments (Fig. 9). Such elements can be rendered with a high degree of accuracy.

An important benefit of a large amount of high accuracy data is the ability to detect discrepancies between the existing drawings and the real situation, in this case, in the point cloud. For example, in 2007, a new library was built in the courtyard. The library has a pyramid-shaped skylight. When the existing fire zone drawings were compared with the point cloud data, a major conflict was discovered concerning the skylight of the new library. The existing drawings and the point cloud data do not coincide, with differences up to 4000 mm. The shape and the size of skylight are remarkably different. This issue leads to another challenge: different drawings containing the same information might be remarkably different. Fire section drawings of the building contain radically wrong information about the skylight, though the HVAC drawings present information in harmony with reality. This problem highlights the shortcomings in the management of building documentation.

6. Problem areas

The case study uncovered a series of problematic areas for future research and development that need to be resolved. The problem areas are covered in the following sections.

6.1. Lack of flexibility when integrating different point cloud data

Problems arose when trying to merge different sets of point cloud data since the software used does not support working in survey coordinate systems. The merging should be done in point cloud processing software. As a consequence, additional data processing and data editing is limited. In a situation where an additional laser scanning campaign is carried out, it would be difficult to merge the additional data

with existing data and moreover to ensure the accuracy and quality of merged data. A simple solution would be to leave out the additional laser scanning campaign and design the process thoroughly. In practice, additional measurements are sometimes important and necessary.

6.2. Absence of a best-fit algorithm

A best-fit algorithm that could help the modeller create surfaces more easily is missing. At the moment a modeller has to choose the best-fit location of surfaces. This could result either in too much generalisation or too little generalisation in the produced model. Either way, modelling will take extra time, since the work has to be done manually.

6.3. Creating window openings

Creating window openings in cases where the opening is not shaped like a cuboid have to be done manually. Other difficulties arise if wall thicknesses differ significantly. Since there is no automatic reconditioning method for windows, this should be considered a significant shortcoming, especially when dealing with larger facilities. One solution to the problem would be to generalise the constructions and use a low level of detail.

6.4. Missing standards for management applications

Standards for building management applications determining requirements for data collection and the level of detail of object modelling are missing. At the moment a modeller can insert information into the model based on the direct needs of the manager rather than on the bases of standards. These direct needs usually reflect requirements of the specific situation and might not consider the information needed for the overall management system, which is connected with the building's lifecycle.

6.5. Organisational challenges

Organisational challenges are related to the classifications under which the items are classified either based on EVS, TALO 200, Omniclass or Masterformat.

When a model is created for managing purposes, it is important that the information is unambiguous and accurate. A fundamental shortcoming is the lack of ability to uniquely describe building information models. The graphical information is one of many elements of a description of the inserted information, but when the data is processed and different databases are used, there is a need for unambiguous definitions. In the case of cross-border cooperation, there is a problem when combining different classifiers.

The problems identified require further research.

Conclusions

The case study presented the workflow and methodology for collecting and processing data for the purpose of creating a BIM model for data management purposes. The data collecting methodology combines the use of TLS with total station surveying. A complete description of the work carried out on the main building of the TTK University of Applied Sciences (TTK/UAS) is presented, and it includes the collecting of interior and exterior data, the data merging process and the creation of the BIM model. The case study highlights several benefits resulting from creation of a BIM model using a point cloud, such as the ability to detect and define the extent of facade damage. Problem areas concerning the process of composing the BIM model using different survey data were also pointed out. The case study shows that the surveying time, data processing time and level of detail are essential in the process of creating a BIM model of an existing building.

References

- 3D Risk Mapping. 2008. *Theory and practice on terrestrial laser scanning* [online]. University of Natural Resources and Life Sciences, Vienna [cited 5 November 2009]. Available from Internet: https://lirias.kuleuven.be/bitstream/123456789/201130/2/Leonardo_Tutorial_Final_vers5_ENGLISH.pdf
- Alkan, R. M.; Karsidag, G. 2012. Analysis of the accuracy of terrestrial laser scanning measurements, in *Proc. of the FIG Working Week*, 6–10 May 2012, Rome, Italy, 16 p.
- Autodesk Inc. 2012. *Building information modeling* [online], [cited 13 August 2012]. Available from Internet: <http://usa.autodesk.com/building-information-modeling>
- Azhar, H. S. 2011. *Building information modeling (BIM): benefits, risks and challenges* [online], McWhorter School of Building Science, Auburn [cited 9 February 2012]. Available from Internet: <http://ascpro.ascweb.org/chair/paper/CPGT182002008.pdf>
- Bauer, U.; Polthier, K. 2009. Generating parametric models of tubes from laser scans, *Computer-Aided Design* 41(10): 719–729. <http://dx.doi.org/10.1016/j.cad.2009.01.002>
- Boehler, W.; Marbs, A. 2003. Investigating laserscanner accuracy, in *Proc. of the 19th CIPA Symposium*, 30 September–4 October, 2003, Antalya, Turkey 19 p.
- Boehler, W.; Marbs, A. 2004. 3D scanning and photogrammetry for heritage recording: a comparison, in *Proc. of the 12th International Conference on Geoinformatics*, 7–8 June, 2004, Gävle, Sweden, 291–298.
- Bosché, F. 2010. Automated recognition of 3D CAD model objects in laser scans and calculation of as-built dimensions for dimensional compliance control in construction, *Advanced Engineering Informatics* 24(1): 107–118. <http://dx.doi.org/10.1016/j.aei.2009.08.006>
- Cheng, M.-Y.; Tsai, H.-C.; Lien, L.-C.; Kuo, C.-H. 2008. GIS-based restoration system for historic timber buildings using RFID technology, *Journal of Civil Engineering and Management* 14(4): 227–234. <http://dx.doi.org/10.3846/1392-3730.2008.14.21>
- CSA. 2005. *Parametric modelling in AutoCAD® – almost* [online], The CSA Newsletter 17(3) [cited 12 September 2012]. Available from Internet: <http://csanet.org/newsletter/winter05/nlw0506.html>
- Donath, D.; Thurow, T. 2007. Integrated architectural surveying and planning: methods and tools for recording and adjusting building survey data, *Automation in Construction* 16(1): 19–27. <http://dx.doi.org/10.1016/j.autcon.2005.10.012>
- Eastman, T. S. L. 2008. *BIM handbook: a guide to building information modeling for owners, managers, architects, engineers, contractors and fabricators*. Hoboken, NJ: John Wiley and Sons, Ltd. 504 p.
- Graphisoft. 2012. *Graphisoft BIMx* [online], [cited 12 September 2012]. Available from Internet: <http://www.graphisoft.com/products/bim-explorer>
- Haala, N.; Kada, M. 2010. An update on automatic 3D building reconstruction, *ISPRS Journal of Photogrammetry and Remote Sensing* 65(6): 570–580. <http://dx.doi.org/10.1016/j.isprsjprs.2010.09.006>
- Jiang, R.; Jáuregui, D. V.; White, K. R. 2008. Close-range photogrammetry applications in bridge measurement: literature review, *Measurement* 41(8): 823–834. <http://dx.doi.org/10.1016/j.measurement.2007.12.005>
- Larsen, K. E.; Lattke, F.; Ott, S.; Winter, S. 2011. Surveying and digital workflow in energy performance retrofit projects using prefabricated elements, *Automation in Construction* 20(8): 999–1011. <http://dx.doi.org/10.1016/j.autcon.2011.04.001>
- Leica Geosystems AG. 2012a. Leica ScanStation C10 – datasheet [online], [cited 15 May 2012]. Available from Internet: http://hds.leica-geosystems.com/downloads123/hds/hds/ScanStation%20C10/brochures-datasheet/Leica_ScanStation_C10_DS_en.pdf
- Leica Geosystems AG. 2012b. Leica TDRA6000 produced inspection certificate M. Article no: 576373. Serial no: 362996.
- Jerma, J. L.; Navarro, S.; Cabrelles, M.; Villaverde, V. 2010. Terrestrial laser scanning and close range photogram-

- metry for 3D archaeological documentation: the Upper Palaeolithic cave of Parpalló as a case study, *Journal of Archaeological Science* 37(3): 499–507. <http://dx.doi.org/10.1016/j.jas.2009.10.011>
- Mechelke, K.; Kersten, T. P.; Lindstaedt, M. 2007. *Comparative investigations into the accuracy behaviour of the new generation of terrestrial laser scanning systems* [online], HafenCity University Hamburg, Hamburg [cited 14 September 2012]. Available from Internet: https://www.hcu-hamburg.de/fileadmin/documents/Geomatik/Labor_Photo/publik/o3d2007_mechelke_et_al.pdf
- Mensi. 2012. *Technical specifications* [online], [cited 24 August 2012]. Available from Internet: <http://mensi.free.fr/english/specsoi.htm>
- Mill, T.; Ellmann, A.; Uueküla, K.; Joala, V. 2011. Road surface surveying using terrestrial laser scanner and total station technologies, in *Proc. of the 8th International Conference Environmental Engineering*, 19–20 May, 2011, Vilnius, Lithuania, 1142–1147.
- Muskett, J. 1995. *Site surveying*. 2nd ed. Hoboken, NJ: Blackwell Science Publications. 432 p.
- Ordóñez, C.; Martínez, J.; Arias, P.; Armesto, J. 2010. Measuring building façades with a low-cost close-range photogrammetry system, *Automation in Construction* 19(6): 742–749. <http://dx.doi.org/10.1016/j.autcon.2010.03.002>
- Rajala, M.; Penttilä, H. 2006. *Testing 3D building modelling framework in building renovation* [online], Helsinki University of Technology, Helsinki [cited 1 October 2012]. Available from Internet: http://www.mittaviiva.fi/hannu/studies/2006_rajal_penttila.pdf
- Riegl Laser Measurement Systems GmbH. 2011. *Riegl VZ®-4000 – datasheet* [online], [cited 5 June 2012]. Available from Internet: http://www.riegl.com/uploads/tx_pxpriegldownloads/10_DataSheet_VZ-4000_27-10-2011_PRELIMINARY.pdf
- Schulz, T.; Ingesand, H. 2004. Terrestrial laser scanning – investigations and applications for high precision scanning, in *Proc. of the FIG Working Week*, 22–27 May, 2004, Athens, Greece. 15 p.
- Tang, P.; Akinci, B. 2012. Formalization of workflows for extracting bridge surveying goals from laser-scanned data, *Automation in Construction* 22: 306–319. <http://dx.doi.org/10.1016/j.autcon.2011.09.006>
- Tse, T. K.; Wong, K. A.; Wong, K. F. 2005. The utilisation of building information models in 3D modelling: a study of data interfacing and adoption barriers, *Journal of Information Technology in Construction, Special Issue From 3D to nD modelling* 10: 85–110.
- US Army Corps of Engineers. 2007. *Engineering and design – control and topographic surveying* [online], The Army Corps of Engineers [cited 15 October 2012]. Available from Internet: http://publications.usace.army.mil/publications/engineering-manuals/EM_1110-1-1005_sec/EM_1110-1-1005_Sections/c-8.pdf
- Weygant, R. S. 2011. *BIM content development: standards, strategies, and best practices*. Hoboken, NJ: John Wiley and Sons Ltd. 464 p.
- Zoller + Fröhlich GmbH. 2012. *Z + F IMAGER® 5010 – datasheet* [online], [cited 3 August 2012]. Available from Internet: http://www.zf-laser.com/Brochure_IMAGER_5010.pdf

Tarvo MILL. Lecturer, MSc, the Chair of Construction Geodesy, Faculty of Construction, Tallinna Tehnikakõrgkool/University of Applied Sciences. Currently pursuing postgraduate studies towards PhD degree in Civil Engineering (Geodesy) at the TUT. Research interests: terrestrial laser scanning, engineering geodesy, building information modelling, maintenance of buildings, management of construction and built environment.

Aivars ALT. Associate Professor of Construction Management, MSc, Department of Civil Engineering, Faculty of Construction, Tallinna Tehnikakõrgkool/University of Applied Sciences. Research interests: construction management and management of built environment, building information modelling, classification of data in construction.

Roode LIHAS. Professor of Facilities Management, PhD, Department of Building Production, Dean of the Faculty of Civil Engineering, Tallinn University of Technology. Research interests: maintenance of buildings, management of construction and built environment, incl. dwellings. He has published about 90 different research papers, 7 textbooks and hand-books, and has also been the author or co-author of several National Standards on maintenance and facilities management. He has been the project manager of several national and international projects.

Mill, T., Ellmann, A., Uekūla, K. and Joala, V. (2011). Road surface surveying using terrestrial laser scanner and total station technologies. *Proceedings of the 8th International Conference Environmental Engineering* (1142–1147). Vilnius, Lithuania: Vilnius Gediminas Technical University Press.

ROAD SURFACE SURVEYING USING TERRESTRIAL LASER SCANNER AND TOTAL STATION TECHNOLOGIES

Tarvo Mill¹, Artu Ellmann², Katrin Uueküla³, Vahur Joala⁴

^{1,2,3}Tallinn University of Technology, Ehitajate tee 5, 19086 Tallinn, Estonia.

E-mails: ¹tarvo@tkk.ee; ²Artu.Ellmann@ttu.ee; ³katrin@geograpp.ee

⁴Leica Geosystems Oy, PL 119, 02631 Espoo, Finland. E-mail: Vahur.Joala@leica-geosystems.com

Abstract. This study compares the applications of two novel surveying technologies for road surface mapping - Terrestrial Laser Scanners and robotic Total Stations. In particular, a Leica HDS3000 and a Leica TCRP 1203 instruments were used. The principles of both technologies are reviewed and their applicability is discussed. The study deals with issues of road surveying under non-stop traffic condition, the safety of surveyors, work methodology, optimization of surveying time. The aspects of data processing, assessment, analysis and achieved accuracy are also handled. Possible reasons for detected discrepancies between different approaches are discussed in detail. The two methods in question both allow the accurate determination of paving material volumes that should be milled off the upper layer of the road surface and the volume of the filling material required to achieve a smooth road surface. However, the study indicates that using conventional surveying methods such as total station surveying in road surface mapping is more time consuming and the results are more generalized than using laser scanning technology where capturing thousands of surface points (i.e. point cloud) takes just seconds.

Keywords: Terrestrial Laser Scanner, mapping of road surface.

1. Introduction

This study compares two different ground profile surveying technologies and corresponding survey results. In particular, an emerging technology of the terrestrial laser scanning is compared with the conventional total station surveying. Both surveying technologies are tested on a 37 meter long road section over a bridge, which is located some 25 km west of Tallinn, the capital of Estonia.

In case of both road ground profile surveying technologies which were used, overviews of surveying equipment and technologies are given. Surveying duration and post-processed survey data is also analyzed in the study.

The study is based on survey data from the Mill (2008) study.

A study focusing on testing a terrestrial laser scanner in high-speed road survey and analyzing the smoothness of the road using laser scanning data was done by Chow (2007).

This study is described in eleven sections. The introduction is followed by a section on surveying principles of terrestrial laser scanning. The third section tackles road ground profile surveying. The fourth and the fifth sections give an overview of the surveying equipment used.

The sixth and seventh sections describe the surveying of a road using laser scanning and total station technology. Post-processing of the data is discussed in the eighth section. The ninth section compares the two surveying methods. The results of the study are discussed in the tenth section. A brief summary concludes the paper.

2. Surveying principles of terrestrial laser scanning

Based on the scanning technologies terrestrial laser scanners can be divided into two basic groups according to scanning technologies: time of flight laser scanners and phase-shift laser scanners.

There are many differences between time of flight laser scanners and phase-shift lasers scanners. In distance determination a phase-shift laser scanner sends out light waves of varying lengths to the target object. Some of the photons fade and some reflect back from the object to the laser scanner. Due to the differences in the oscillation of the waves which were sent out and the waves the reflected back in the opposite phase, a phase-shift arises. A phase shift is any change that occurs in the phase of one quantity, or in the phase difference between two or more quantities (Glen 2005). The distance of a survey point is determined using the size of the phase of phase-shifts (figure 1).

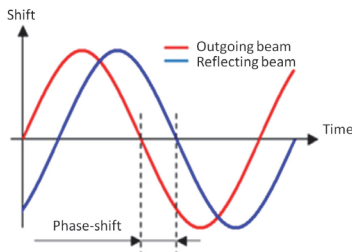


Fig 1. The difference in phase of two waves is known as the phase shift

In contrast, the time of flight laser scanners determine distances by measuring how long it takes for the pulse of light to reflect back from the object. Note that the distance is twice as long as the actual distance because the pulse of light moves forth and back. The distance is computed by $(c \cdot t)/2$, where t is the round-trip time, and c is the speed of light. Time of flight scanner distance measuring accuracy is dependent on how precisely time (t) is measured, let it be said that for a pulse of light to travel one millimeter takes 3,3 picoseconds ($3,3 \cdot 10^{-12}$).

A terrestrial laser scanner scans its entire field of view one point at a time by changing the laser rangefinder's direction of view to scan different points. The vertical direction of the laser rangefinder is changed by using a system of rotating mirrors; the horizontal direction of the laser rangefinder is changed by rotating the laser scanner itself around the vertical axis. While time of flight laser scanners can determine up to 50 000 points per second (Leica Geosystems 2010), then phase-shift laser scanners can determine up to 1 000 000 points per second (Zoller+Fröhlich 2010).

The duration of the scanning process is dependent on both the speed of determining distances and scanning resolution.

A major disadvantage with phase-shift scanners is their shorter measuring distances being typically less than 100 meters.

The main advantage of time of flight scanners is their long range, up to 1000 meters. The shortage of time of flight laser scanners is their relatively inaccurate time measurements. Distance measurement accuracy is in millimeters. For example, the Leica HDS 3000 scanner used in our study determines distances with an accuracy of ± 4 mm.

3. Road ground profile surveying

Using studded tires in wintertime in temperate zones where overall average yearly temperature $+5$ °C is quite common. Inevitably using studded tires is the main cause of wear of asphalt cover. Wear and sagging are in turn the main cause of ruts in the road surface. Considered the fact that in temperate zones the amount of rainfall exceeds evaporation and temperatures fluctuate substantially

around 0 °C. Consequently, the water in pavement cracks often freezes and melts, causing the formation of holes (water expands when frozen) (WSDT - State Materials Laboratory 2008).

Reconstruction of asphalt paving is usually accomplished by milling off the uneven top layer of the road cover and filling the holes and milled ruts with asphalt. For the reconstruction works, the existing road cover needs to be mapped beforehand. Usually the road surface model is created using total station survey data. To construct a surface model of a two lane road, cross profile points are measured from each side and from the centre of the road with a step of 10 meters in settlements and outside settlements where there are curbstones on road sides. In rural areas the cross profile points are measured with a step of 12, 5 meters. Requirements state that the longest sight distance on road profile mapping should not be greater than 150 meters. Errors in the surveying heights must not exceed ± 2 cm, with respect to the surveying network (Estonian Road Administration 2008).

As mentioned before, a total station is used for conventional road surveying. In this case a reflector prism is placed at each survey point. One of major disadvantages of this type of survey method is lack of detail in the surface model created. Let it also be mentioned that the shape of surface model produced depends much on where precisely the reflector prism pole had been placed, whether it had been placed on a level plane surface, or on a lower surface dent or on a higher hump. Therefore, the produced road surface model may not reflect in sufficient detail the depths of dents and the heights of humps. If such a micro-relief is needed by the conventional total station survey, then this may to greater overall resource costs.

A major problem in road surveying with a total station is the safety of surveyors, since it is very difficult to work on the road when it's not closed down to traffic. Commuters on the road might not notice the surveyor. The risks are even higher when working on highways where safety is not ensured by the wearing of just a reflector vest or placement of safety cones.

Using a terrestrial laser scanner for road surface mapping does not require the need of road closure.

In order to compare two different technologies for road surface mapping, in June 2007 a terrestrial laser scanning and total station surveying were carried out. The work was accomplished using a Leica Terrestrial laser scanner HDS 3000 and a Leica total station TSRP 1203. As a result, two road surface models of the 37 m long strip crossing the bridge were created, one based on the laser scanning data and the other one on the total station survey data.

4. Terrestrial laser scanner Leica HDS 3000

The terrestrial laser scanner Leica HDS 3000 kit consists of software and hardware. The hardware side consists of a laser scanner, batteries, a 220 V adapter and a laptop which is used for controlling the scanning process and saving scanned data. Targets and target mounts

(figure 2) are also included in the hardware kit. Targets are determined from different scanning stations which are afterwards used to join all point clouds measured from different stations together.



Fig 2. Leica target mount

The software side consists mainly of the program Leica Cyclone, which has a number of sub modules for scanning and for modeling. We can also include Bentley's MicroStation and Autodesk's AutoCad with the plug-in COE (Cyclone Object Exchange) and Cloudworx for Microstation/AutoCad into the software set. COE is a plug-in which is used to exchange data between Cyclone and MicroStation or AutoCad. Cloudworx for MicroStation/AutoCad is a plug-in which is used to produce topographic plans or profiles in MicroStation or AutoCad drafting environments .

5. Total station Leica TCRP 1203

The total station Leica TCRP 1203 kit contains the total station, a reflector prism pole, a 360° reflector prism and a remote control.

The Leica TCRP 1203 is an instrument with an automated reflector prism tracking system and a remote control system. The reflector prism tracking system leaves out the need of precise sighting onto the prism. The Power Search software helps finding the prism if the connection between the total station and the prism is lost.

The remote control screen shows the same picture which is on the total station screen in real time. In addition, the remote control has a touch-screen and a full QWERTY keyboard. Controlling the total station via the remote control device is analogous to controlling the total station using the keyboard on the total station. All functions on remote control are the same as on the total station.

6. Scanning the road surface

The scanning process begins with observing the scanning area, determining the potential locations for the scanner and placing targets. The used Leica HDS 3000 terrestrial laser scanner determines 1800 points per second.

Scanning of the road strip was done from two scanner positions located at opposite sides of the bridge. One station was located at the southwest end of the bridge and

the other at the northeast end of the bridge (figure 3). The entire scanning process took 2 hours and 40 minutes. Initially the survey data was collected in an arbitrary coordinate system. However, using control points which were coordinated with a total station, the point cloud was converted into the Estonian National 2D rectangular coordinate system L-EST 97, and the -heights into the Estonian National height system Baltic 1977. A total of 1 394 426 points were gathered in scanning, 256 722 of which were used to create road surface.



Fig 3. Laser scanning results from the southwest end of the bridge (left) and at the other at the end of northeast of the bridge (right). Scanner positions are marked with xyz coordinate axis

7. Total station surveying

Surveying speed with a total station depends largely on traffic frequency. Namely the connection between the total station and the reflector prism can be interrupted easily by passing by vehicles; – therefore, some of the points need to be remeasured. Surveying is complicated due to safety considerations because surveying points must also be determined on the centre of the road.

Road profile field works took 2 hours and 20 minute's altogether. To receive a detailed model of the surface of the road, the surface was measured with a step of approximately one meter in the longitudinal direction, while in the transverse direction five points were measured, two from both sides and one from the middle. Thus, the number of the points exceeds approximately 10 times the requirements of the Road Administration. From the 37 meter long road, a total of 244 points were gathered.

The entire measuring process was carried out without road closure (i.e. the same way as laser scanning).

Survey data is in the Estonian National planar coordinate system L-EST 97, while heights are in the Estonian National height system Baltic 1977 (i.e. in the same coordinate and height system as the laser scanning results).

8. Post processing of the survey data

All survey data processing was done using the Bentley MicroStation V8 drafting program.

Both the data gathered with the total station and with the laser scanner TIN (TIN - triangulated irregular network) triangulation models were produced. The TIN triangulation model is used because the surface of the road is uneven. The triangulation model is essentially a 3D representation of the roads' surface created using the heights of survey points. Where heights increase gradually or where heights are even the triangular facets of the

network is larger; where the surface is more rugged the triangular facets of the network is smaller (figure 4). The edges of the triangles coincide generally in higher points and in lower points.

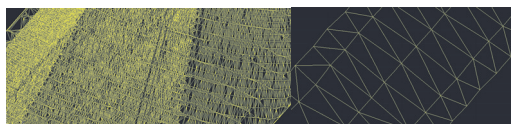


Fig 4. Fragment of TIN mesh model created using laser scanning data (Left-hand side), fragment of TIN mesh model created using total station survey data (right-hand side)

Contour lines intersecting after every 2 cm were added to both road surface models (figure 5).

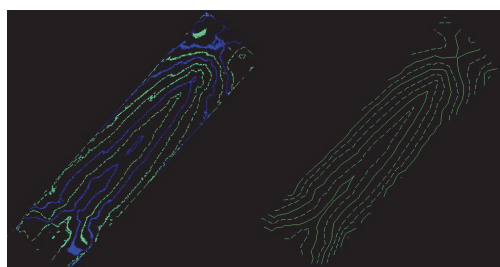


Fig 5. Surface models with contour lines. Model created using laser scanner data (left-hand side) and model created using total station survey data (right-hand side)

9. Indirect comparison of survey methods

The terrestrial laser scanner Leica HDS 3000 works within a range of up to 300 meters. The effective measurement range depends on the surface to be scanned. Road surface is a relatively horizontal surface and if we place the scanner onto a tripod two meters from the ground, then the scanning range in one direction could be 60 meters, the angle of the laser beam in the horizontal direction is then 3° (therefore, we can scan easily up to 100 meters of road in one position). In total, the distance would be 120 meters, 60 meters in each direction. If we look at a two lane road which is approximately 11 meters in width, then the entire survey area would be $120 \cdot 11 = 1320 \text{ m}^2$. Taking into account the fact that the scanning speed is up to 1800 points per second and the scanning resolution is 10 centimeters, then roughly scanning an area of 180 m^2 takes only a second and scanning a total area 1320 m^2 takes only 7,3 seconds. We must also consider that scanning area assignment is based on a dome shape photo image (full $360^\circ \cdot 270^\circ$ dome). The scanning area selection is accomplished by selecting segment areas of the dome using degrees. Because a road is a line object then selecting the area just once is usually not enough, therefore prolonging the scanning process. Difficulties with assigning the scanning area might arise if the scanner is placed on the side of the road. If the scanner is

placed in the middle of the road, for instance, on an overpass, then selecting the scanning area is easier.

Specifications for the total station Leica TCRP 1203 indicate that the maximum range is up to 1000 meters. Determining reflector prism point takes 0,3 seconds in tracking mode, while the normal walking speed is 5 kilometers per hour, i.e., 85 meters per minute. If we determine the side points and centre point (three points in total) on a two lane road with a step of 10 meters, then the walking distance of the survey area is $120/10 \cdot 11 = 132$ meters. To walk a distance of 132 meters takes 1,6 minutes. Therefore, the surveying time for the 1320 m^2 area would come to roughly $(12 \cdot 3 \cdot 0,3) + 1,6 = 12,4$ minutes. If we consider traffic density, surveyors' safety, the directing of the reflector prism, intermittent loss of the connection between the remote control and the total station, then the total survey time can increase significantly.

In conclusion surveying an area of 1320 m^2 with a laser scanner could be done in a matter of seconds, roughly calculated 7,3 seconds. Surveying the same area with a total station takes several minutes, roughly 12,4 minutes.

10. Comparing the results

To compare two different sets of survey data, the data was imported into the Bentley MicroStation V8 drafting program and two TIN surface models were created.

The model created using the total station survey data and the model created using laser scanning data were superimposed. The triangular meshes were activated and elevation difference command was executed. The program calculates within selected areas the differences in model heights and shows divergent areas using colors. We must keep in mind that when creating TIN meshes, the amount of survey points is crucial. Figure 6 illustrates the differences with contour lines between the two TIN meshes created. Blue contour lines illustrate the lower parts of the differences, white contour lines illustrate equal heights, and orange contour lines illustrate the higher parts. At the northeast and southwest ends the total station points are higher than the laser scanner points. Points with equal heights are scattered on the model. The biggest difference between heights is $-8,1$ centimeters at the southern corner of the model. The lowest difference between heights is $+0,8$ centimeters at the northern end of the model.

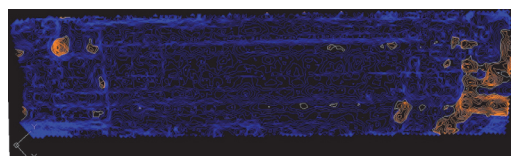


Fig 6. Comparison result of two TIN meshes. Northeast direction is right

From the comparison model we can conclude that total station survey points appear to be lower than the laser scanner points, and this is probably caused due the

fact that the cross profile transverse gradient values are not constant given the unevenness caused by the state of wear and sagging of the paving surface and of the road. The total station survey points could be located on sags or on higher humps; therefore the model created using total station survey data is more generalized. At the same time the distance between laser scanner survey points is occasionally less than a centimeter producing highly detailed surface information.

11. Comparison the two surface models with a project surface

Using total station survey data a project surface of the road was created. The project surface has given the nature of the road in question a suitable longitudinal gradient 0,47% and a transverse gradient on two sides of 2,5% (figure 7). Comparing the project surface with surfaces created using laser scanner and total station survey data gives the amount of material that needs to be milled off the top layer of the road surface or the amount of filling material needed to smoothen the road surface.

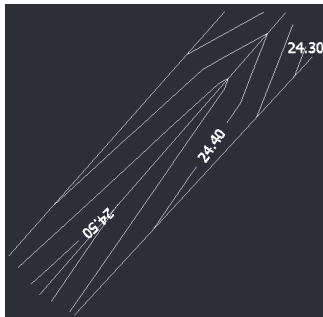


Fig 7. Project surface of the road

Comparing the project surface with the model created using laser scanning survey data show that on the 37 meter long road strip the amount of the material that should be milled off is 0,21 m³ and the amount of filling material to be used is 6,54 m³. Comparing the project surface with the model created using total station survey data shows that on the 37 meter long road strip the amount of the material that should be milled off is 0,24 m³ and the amount of filling material to be used is 4,85 m³.

The results show surprisingly little differences in material quantities that should be milled off the road surface and material quantities that should be used to fill the road surface, even though laser scanning technology has a great advantage due to a larger amount of points. The differences could be due the fact that the total station survey was carried out ten times more densely than required. The differences amount to only 0,03 m³ of material that should be milled of the road surface and 1,69 m³ that should be filled along the 37 meter long strip.

12. Conclusions

Terrestrial laser scanners collect a large number of points from the observed object within a short period of time. The collected points make up a point cloud. The point cloud includes information about the scanned object, each point holding xyz coordinates, the RGB code, and the reflection intensity value. Point clouds are easy to use in various applications, beginning with just simple research and ending with different data processing operations such as modeling and designing.

The application areas of terrestrial laser scanning technology are increasing all the time. Every year there are newer and more efficient models introduced on the market. The latest time of flight laser scanners like the Leica C10 and Trimble CX 3D are capable of collecting up to 50 000 points per second (Leica Geosystems 2010, Trimble 2010). In comparison, the laser scanner used in this study is able to collect only up to 1800 points per second. The difference is nearly thirty times, this has a great impact on the working pace. Producers placed great emphasis on user friendliness, so there are fewer or no cables at all, while data transferring is carried out using Bluetooth, Compact Flash Memory Card or other similar means; there are no external batteries; and there is no need for a control laptop because controlling can be done on the scanner.

In the course of the study, two road surface models were created, one using total station survey data and the other laser scanner survey data. The model created using laser scanning data is several times more detailed than the model created using total station survey data due to the number of survey points.

If the road surface model is more detailed, then we can determine the optimal material quantities that should be milled off the surface of the road and the optimal material quantities that should be used to fill the road surface.

In conclusion we can state that primary advantages of using terrestrial laser scanning technologies in such working areas lie in the surveying speed, the safety of a surveyor, and the absence of a disruption to traffic. Laser scanning certainly provides advantages over total station surveying when surveying objects such as bigger roads, highways and tunnels (subways), when the closure of the object for surveying is out of the question or very complicated. The disadvantage of using terrestrial laser scanner is its dependence on the weather. Scanning work is not possible when it's snowing and raining because the laser beams might reflect off from the snowflakes or rain drops.

References

- Chow, K. L. 2007. *Engineering Survey Applications of Terrestrial Laser Scanner in Highways Department of the Government of Hong Kong Special Administration Region (HKSAR)*. Hong Kong: FIG Working Week 2007

- Estonian Road Administration 2008. *Additional requirements for topo-geodetic research in road design*. Tallinn: Estonian Road Administration. 10 p.
- Glen, B. 2005. *Handbook for sound engineers*. [online], 5(3): 5–21 [viewed on October 15, 2010]. Available on the Internet: <<http://books.google.com/books?id=y0d9VA0lkogC&pg=PA1499#v=onepage&q&f=false>>. ISBN 0240807588.
- Leica Geosystems 2010. *Leica ScanStation C10 - Datasheet*. Heerbrugg: Leica Geosystems AG [viewed on August 23, 2010]. Available on the Internet: <http://hds.leica-geosystems.com/en/Leica-ScanStation-C10_79411.htm>
- Mill, T 2008. *Comparison of different geodetic bridge surveying methods*. Tallinn: Tallinn University of Technology 100 p.
- Trimble 2010. *Trimble CX 3D Laser Scanner* [viewed on October 14 2010]. Available on the Internet: <<http://www.trimble.com/construction/building-construction/cx-3d-laser-scanner.aspx>>
- Washington State Department of Transportation - State Materials Laboratory 2008. *Pavements and studded tire damage*. Washington: Washington State Department of Transportation - State Materials Laboratory. 21 p.
- Zoller+Fröhlich 2010. *Z+F IMAGER® 5010 - Datasheet*. Zoller+Fröhlich GmbH [viewed on August 23, 2010]. Available on the Internet: <http://www.zf-laser.com/e_z_f-laserscanner.html>

CURRICULUM VITAE

Personal data

Name: Tarvo Mill
Date and place of birth: 19.05.1983, Tallinn
Nationality: Estonian
E-mail: Tarvo.mill@tktk.ee

Education

Educational institution	Graduation year	Field of study, degree
Tallinn University of Technology	2008	Transport Engineering and Logistics, MSc
Tallinn College of Engineering	2006	Construction Geodesy, First stage of higher education

Language skills

Language	Level
Estonian	Native language
English	Average
Russian	Basic

Professional Employment

Period	Organisation	Position
2005 - ...	TTK University of Applied Sciences	Lecturer
08.01.2014 - 12.31.2014	Tallinn University of Technology	Junior Researcher
2003 - 2005	Geometria OÜ	Surveyor

Publications

- Mill, T. and Ellmann, A. (2017, online). Assessment of along-normal uncertainties for application to terrestrial laser scanning surveys of engineering structures. *Survey Review*. DOI: 10.1080/00396265.2017.1361565
- Mill, T. (2016). Simulation of terrestrial laser scanning errors occurring during deformation monitoring. *Proceedings of the 3rd Joint International Symposium on Deformation Monitoring (JISDM)* (pp 1–9). Vienna, Austria: Vienna University of Technology.
- Mill, T., Ellmann, A., Kiisa, M., Idnurm, J., Idnurm, S. Horemuz, M. and Aavik, A. (2015). Geodetic Monitoring of Bridge Deformations Occurring during Static Load Testing. *The Baltic Journal of Road and Bridge Engineering*, 10(1), 17–27.

- Sobak, M., Ellmann, A. and Mill, T. (2015). Terrestrial laser scanning assessment of generalization errors in conventional topographic surveys. *Geodesy and Cartography*, 41(1), 15–24.
- Mill, T., Ellmann, A., Aavik, A., Horemuz, M. and Sillamäe, S. (2014). Determining ranges and spatial distribution of road frost heave by terrestrial laser scanning. *The Baltic Journal of Road and Bridge Engineering*, 9(3), 227–236.
- Mill, T. and Ellmann, A. (2014). Terrestrial laser scanning technology for deformation monitoring of a large suspension roof structure. *Proceedings of the 6th International Conference on Engineering Surveying (INGEO)* (pp 179–186). Prague, Czech Republic: CTU Printhouse.
- Sobak, M., Ellmann, A. and Mill, T. (2014). Pinnavormide mõõdistuspunktide asukohavalikust tulenevate üldistusvigade kvanifitseerimine terrestrial laser skanneerimise lausandmestiku põhjal. *Geodeet*, 44, 84–91.
- Mill, T. and Ellmann, A. (2014). Rahvusvaheline ehitusgeodeesia konverents INGEO Prahast. *Geodeet*, 44, 47–48.
- Mill, T., Alt, A. and Liias, R. (2013). Combined 3D building surveying techniques – terrestrial laser scanning (TLS) and total station surveying for BIM data management purposes. *Journal of Civil Engineering and Management*, 19, S23–S32.
- Ustinova, N., Kala, V., Mill, T. and Ellmann, A. (2012). Geodetic Surveying Studies for Civil Engineering Students at Tallinn University of Technology. *Geodesy and Cartography*, 38(2), 86–91.
- Mill, T., Ellmann, A., Uueküla, K. and Joala, V. (2011). Road surface surveying using terrestrial laser scanner and total station technologies. *8th International Conference Environmental Engineering* (pp 1142–1147). Vilnius, Lithuania: Vilnius Gediminas Technical University Press.
- Mill, T., Ellmann, A., Uueküla, K. and Joala, V. (2011). Teetasapinna mõõdistamine terrestrial laser skanneerimise ja elektrontahhümeetrilise mõõdistamise tehnoloogiaga. *Geodeet*, 41, 81–85.

Presentations in international conferences:

- Mill, T. (2016). Simulation of terrestrial laser scanning errors occurring during deformation monitoring. *Proceedings of the 3rd Joint International Symposium on Deformation Monitoring (JISDM)* (pp 1–9). Vienna, Austria: Vienna University of Technology.
- Mill, T. and Ellmann, A. (2014). Terrestrial laser scanning technology for deformation monitoring of a large suspension roof structure. *Proceedings of the 6th International Conference on Engineering Surveying (INGEO)* (pp 179–186). Prague, Czech Republic: CTU Printhouse.

Mill, T., Ellmann, A., Uekūla, K. and Joala, V. (2011). Road surface surveying using terrestrial laser scanner and total station technologies. *8th International Conference Environmental Engineering* (pp 1142–1147). Vilnius, Lithuania: Vilnius Gediminas Technical University Press.

ELULOOKIRJELDUS

Isikuandmed

Nimi: Tarvo Mill
Sünni aeg ja koht: 19.05.1983, Tallinn
Kodakondsus: Eesti
E-post: Tarvo.mill@tktk.ee

Haridustee

Õppeasutus	Lõpetamise aeg	Haridus (eriala/kraad)
Tallinna Tehnikaülikool	2008	Transpordiehitus ja logistika, magister
Tallinna Tehnikakõrgkool	2006	Rakendusgeodeesia, rakendus kõrghariduse diplom

Keelteoskus

Keel	Tase
Eesti	Emakeel
Inglise	Kesktaase
Vene	Baastase

Teenistuskäik

Töötamise aeg	Tööandja	Ametikoht
2005 - ...	Tallinna Tehnikakõrgkool	Lektor
08.01.2014 - 12.31.2014	Tallinna Tehnikaülikool	Noorteadur
2003 - 2005	Geometria OÜ	Maamõõtja

Avaldatud teadusartiklite loetelu on toodud ingliskeelse CV juures.

**DISSERTATIONS DEFENDED AT
TALLINN UNIVERSITY OF TECHNOLOGY ON
CIVIL ENGINEERING**

1. **Heino Mölder**. Cycle of Investigations to Improve the Efficiency and Reliability of Activated Sludge Process in Sewage Treatment Plants. 1992.
2. **Stellian Grabko**. Structure and Properties of Oil-Shale Portland Cement Concrete. 1993.
3. **Kent Arvidsson**. Analysis of Interacting Systems of Shear Walls, Coupled Shear Walls and Frames in Multi-Storey Buildings. 1996.
4. **Andrus Aavik**. Methodical Basis for the Evaluation of Pavement Structural Strength in Estonian Pavement Management System (EPMS). 2003.
5. **Priit Vilba**. Unstiffened Welded Thin-Walled Metal Girder under Uniform Loading. 2003.
6. **Irene Lill**. Evaluation of Labour Management Strategies in Construction. 2004.
7. **Juhan Idnurm**. Discrete Analysis of Cable-Supported Bridges. 2004.
8. **Arvo Iital**. Monitoring of Surface Water Quality in Small Agricultural Watersheds. Methodology and Optimization of monitoring Network. 2005.
9. **Liis Sipilgas**. Application of Satellite Data for Monitoring the Marine Environment. 2006.
10. **Ott Koppel**. Infrastruktuuri arvestus vertikaalselt integreeritud raudtee-ettevõtja korral: hinnakujunduse aspekt (Eesti peamise raudtee-ettevõtja näitel). 2006.
11. **Targo Kalamees**. Hygrothermal Criteria for Design and Simulation of Buildings. 2006.
12. **Raido Puust**. Probabilistic Leak Detection in Pipe Networks Using the SCEN-UA Algorithm. 2007.
13. **Sergei Zub**. Combined Treatment of Sulfate-Rich Molasses Wastewater from Yeast Industry. Technology Optimization. 2007.
14. **Alvina Reihan**. Analysis of Long-Term River Runoff Trends and Climate Change Impact on Water Resources in Estonia. 2008.
15. **Ain Valdmann**. On the Coastal Zone Management of the City of Tallinn under Natural and Anthropogenic Pressure. 2008.
16. **Ira Didenkulova**. Long Wave Dynamics in the Coastal Zone. 2008.
17. **Alvar Toode**. DHW Consumption, Consumption Profiles and Their Influence on Dimensioning of a District Heating Network. 2008.

18. **Annely Kuu.** Biological Diversity of Agricultural Soils in Estonia. 2008.
19. **Andres Tolli.** Hiina konteinerveod läbi Eesti Venemaale ja Hiinasse tagasisaadetavate tühjade konteinerite arvu vähendamise võimalused. 2008.
20. **Heiki Onton.** Investigation of the Causes of Deterioration of Old Reinforced Concrete Constructions and Possibilities of Their Restoration. 2008.
21. **Harri Moora.** Life Cycle Assessment as a Decision Support Tool for System optimisation – the Case of Waste Management in Estonia. 2009.
22. **Andres Kask.** Lithohydrodynamic Processes in the Tallinn Bay Area. 2009.
23. **Loreta Kelpšaitė.** Changing Properties of Wind Waves and Vessel Wakes on the Eastern Coast of the Baltic Sea. 2009.
24. **Dmitry Kurennoy.** Analysis of the Properties of Fast Ferry Wakes in the Context of Coastal Management. 2009.
25. **Egon Kivi.** Structural Behavior of Cable-Stayed Suspension Bridge Structure. 2009.
26. **Madis Ratassepp.** Wave Scattering at Discontinuities in Plates and Pipes. 2010.
27. **Tiia Pedusaar.** Management of Lake Ülemiste, a Drinking Water Reservoir. 2010.
28. **Karin Pachel.** Water Resources, Sustainable Use and Integrated Management in Estonia. 2010.
29. **Andrus Räämet.** Spatio-Temporal Variability of the Baltic Sea Wave Fields. 2010.
30. **Alar Just.** Structural Fire Design of Timber Frame Assemblies Insulated by Glass Wool and Covered by Gypsum Plasterboards. 2010.
31. **Toomas Liiv.** Experimental Analysis of Boundary Layer Dynamics in Plunging Breaking Wave. 2011.
32. **Martti Kiisa.** Discrete Analysis of Single-Pylon Suspension Bridges. 2011.
33. **Ivar Annus.** Development of Accelerating Pipe Flow Starting from Rest. 2011.
34. **Emlyn D. Q. Witt.** Risk Transfer and Construction Project Delivery Efficiency – Implications for Public Private Partnerships. 2012.
35. **Oxana Kurkina.** Nonlinear Dynamics of Internal Gravity Waves in Shallow Seas. 2012.
36. **Allan Hani.** Investigation of Energy Efficiency in Buildings and HVAC Systems. 2012.

37. **Tiina Hain.** Characteristics of Portland Cements for Sulfate and Weather Resistant Concrete. 2012.
38. **Dmitri Loginov.** Autonomous Design Systems (ADS) in HVAC Field. Synergetics-Based Approach. 2012.
39. **Kati Kõrbe Kaare.** Performance Measurement for the Road Network: Conceptual Approach and Technologies for Estonia. 2013.
40. **Viktorja Voronova.** Assessment of Environmental Impacts of Landfilling and Alternatives for Management of Municipal Solid Waste. 2013.
41. **Joonas Vaabel.** Hydraulic Power Capacity of Water Supply Systems. 2013.
42. **Inga Zaitseva-Pärnaste.** Wave Climate and its Decadal Changes in the Baltic Sea Derived from Visual Observations. 2013.
43. **Bert Viikmäe.** Optimising Fairways in the Gulf of Finland Using Patterns of Surface Currents. 2014.
44. **Raili Niine.** Population Equivalence Based Discharge Criteria of Wastewater Treatment Plants in Estonia. 2014.
45. **Marika Eik.** Orientation of Short Steel Fibers in Concrete. Measuring and Modelling. 2014.
46. **Maija Viška.** Sediment Transport Patterns Along the Eastern Coasts of the Baltic Sea. 2014.
47. **Jana Pöldnurk.** Integrated Economic and Environmental Impact Assessment and Optimisation of the Municipal Waste Management Model in Rural Area by Case of Harju County Municipalities in Estonia. 2014.
48. **Nicole Delpeche-Ellmann.** Circulation Patterns in the Gulf of Finland Applied to Environmental Management of Marine Protected Areas. 2014.
49. **Andrea Giudici.** Quantification of Spontaneous Current-Induced Patch Formation in the Marine Surface Layer. 2015.
50. **Tiina Nuuter.** Comparison of Housing Market Sustainability in European Countries Based on Multiple Criteria Assessment. 2015.
51. **Erkki Seinre.** Quantification of Environmental and Economic Impacts in Building Sustainability Assessment. 2015.
52. **Artem Rodin.** Propagation and Run-up of Nonlinear Solitary Surface Waves in Shallow Seas and Coastal Areas. 2015.
53. **Kaspar Lasn.** Evaluation of Stiffness and Damage of Laminar Composites. 2015.
54. **Margus Koor.** Water Distribution System Modelling and Pumping Optimization Based on Real Network of Tallinn. 2015.

55. **Mikk Maivel.** Heating System Efficiency Aspects in Low-Energy Residential Buildings. 2015.
56. **Kalle Kuusk.** Integrated Cost-Optimal Renovation of Apartment Buildings toward Nearly Zero-Energy Buildings. 2015.
57. **Endrik Arumägi.** Renovation of Historic Wooden Apartment Buildings. 2015.
58. **Tarvo Niine.** New Approach to Logistics Education with Emphasis to Engineering Competences. 2015.
59. **Martin Thalfeldt.** Total Economy of Energy-Efficient Office Building Facades in a Cold Climate. 2016.
60. **Aare Kuusik.** Intensifying Landfill Wastewater and Biodegradable Waste Treatment in Estonia. 2016.
61. **Mart Hiob.** The Shifting Paradigm of Spatial Planning in Estonia: The Rise of Neighbourhood Participation and Conservation of Built-up Areas through the Detailed Case Study of Supilinn, a Historic Suburb of Tartu City, Estonia. 2016.
62. **Martin Heinvee.** The Rapid Prediction of Grounding Behavior of Double Bottom Tankers. 2016.
63. **Bharat Maharjan.** Stormwater Quantity and Quality of Large Urban Catchment in Tallinn. 2016.
64. **Nele Nutt.** The Restoration of Nationally Protected Estonian Manor Parks in the Light of the Florence Charter. 2017.
65. **Üllar Alev.** Renovation and Energy Performance Improvement of Estonian Wooden Rural Houses. 2017.
66. **Simo Ilomets.** Renovation Need and Performance of Envelopes of Concrete Apartment Buildings in Estonia. 2017.
67. **Argo Kuusik.** Determining Biogas Yield from Industrial Biodegradable Waste. 2017.
68. **Katri Pindsoo.** Spatio-Temporal Changes in the Components of Extreme Water Levels on Estonian Coasts. 2017.